

博士論文 (要約)

Liquid-Crystal-Enhanced Electret
Vibration Energy Harvester

(液晶により強化されたエレクトレット
環境振動発電器)

KASIDIS KITTIP AISALSILPA
キッティパイサルシルパ カシディス

Table of Contents

Table of Contents.....	i
List of Figures.....	iii
List of Tables.....	vii
Acknowledgement.....	viii
ABSTRACT.....	ix
 CHAPTER 1 INTRODUCTION.....	 1
1.1 ENERGY DEMAND IN IoT AND WSN	2
1.2 ENERGY HARVESTING	3
1.1.1 <i>Vibration-based Energy Harvesting.....</i>	4
1.2 ELECTRET MATERIALS	7
1.3 ELECTROSTATIC/ELECTRET ENERGY HARVESTER	7
1.3.1 <i>Working Principle.....</i>	10
1.3.2 <i>Electrode Configuration.....</i>	11
1.3.3 <i>Output Power Modelling for Electret Vibration Generator</i>	14
1.4 PARASITIC CAPACITANCE AND ITS EFFECT.....	15
1.4.1 <i>Modelling of C_p.....</i>	17
1.4.2 <i>Reduction of C_p.....</i>	18
1.5 STRATEGY FOR ENHANCING OUTPUT POWER	19
1.6 OBJECTIVES AND THESIS ORGANIZATION	21
 CHAPTER 2 LIQUID-CRYSTAL-ENHANCED ELECTRET VIBRATION ENERGY HARVESTER	 23
2.1 CHAPTER INTRODUCTION	24
2.2 ANISOTROPIC PERMITTIVITY MATERIALS.....	24
2.3 LIQUID CRYSTAL AS ANISOTROPIC PERMITTIVITY FLUID	24
2.4 BASIC NEMATIC LIQUID CRYSTALS	26
2.5 ELECTRICAL CHARACTERIZATION OF LIQUID CRYSTAL	27
2.5.1 <i>Impedance Analyzing.....</i>	27
2.6 CHARACTERIZATION RESULTS	30
2.6.1 <i>Relative Permittivity and Threshold voltage.....</i>	30
2.6.2 <i>Resistivity of 5CB and BCH-5F.F.F.....</i>	32
2.7 OUTPUT POWER GENERATION EXPERIMENTS WITH ELECTROSTATIC VIBRATION ENERGY HARVESTER	33
2.7.1 <i>1-D Electrostatic Model of Electrostatic Vibration Energy Harvester</i>	33
2.7.2 <i>Fabrication of Electrostatic Vibration Energy Harvester.....</i>	35
2.7.3 <i>Experimental Setup.....</i>	36
2.7.4 <i>Output Power Generation Results</i>	38
2.8 SURFACE CHARGE DECAY OF ELECTRET AND TRADE-OFF FROM LIQUID CRYSTAL	40
2.9 HIGH-RESISTIVITY NEMATIC LIQUID CRYSTAL	41
2.10 EFFECTS OF IMPURITY AND HUMIDITY ON LIQUID CRYSTAL	43
2.10.1 <i>Effect of Impurity and Humidity on Resistivity of LC.....</i>	43
2.10.2 <i>Effect of Impurity/Humidity Control on Surface Charge Decay of Electret with LC</i>	44
2.10.3 <i>Output Power Generation Experiment of Electret Vibration Energy Harvester with Impurity/Humidity Control.....</i>	45
2.11 CHAPTER SUMMARY	48

CHAPTER 3 LIQUID CRYSTAL ALIGNMENT MEASUREMENT AND DEVELOPMENT OF GENERATOR MODEL	49
3.1 CHAPTER INTRODUCTION	50
3.2 OUTPUT POWER MODELLING WITH FIELD-DEPENDENT PERMITTIVITY	50
3.3 RELATIONSHIP BETWEEN RELATIVE PERMITTIVITY AND ALIGNMENT ANGLE OF LC	51
3.4 LIQUID CRYSTAL ALIGNMENT MEASUREMENT	52
3.4.1 <i>Fourier Transform Infrared Spectroscopy</i>	52
3.4.2 <i>Polarized Optical Microscopy</i>	58
3.5 OUTPUT POWER MODELING WITH DYNAMIC PERMITTIVITY AND C_p	69
3.6 PERFORMANCE PREDICTION FOR LC-ENHANCED ELECTRET VIBRATION ENERGY HARVESTER	69
3.6.1 <i>Output Power Enhancement</i>	69
3.6.2 <i>Viscous Energy Loss</i>	70
3.6.3 <i>Figure of Merit for Permittivity Fluids</i>	74
3.7 CHAPTER SUMMARY	75
CHAPTER 4 ABSORBANCE OF ION IMPURITY WITH FERROELECTRIC MATERIALS FOR LIQUID-CRYSTAL-ENHANCED ELECTRET VIBRATION ENERGY HARVESTER.....	76
4.1 CHAPTER INTRODUCTION	77
4.2 IMPURITY CONTROL FOR RESISTIVITY RETENTIONS IN LIQUID CRYSTAL	77
CHAPTER 5 CONCLUSIONS	79
CHAPTER 6 REFERENCES.....	82
LIST OF PUBLICATIONS/CONFERENCES.....	90
APPENDIX.....	110

LIST OF FIGURES

FIGURE 1.1 VARIOUS FIELDS THAT COULD BE BENEFITTED FROM INTERNET OF THINGS (IoT). [4]	2
FIGURE 1.2 DIFFERENT KIND OF AMBIENT ENERGY SOURCES FOR ENERGY HARVESTING [7]	3
FIGURE 1.3 TYPICAL CONVERSION MECHANISMS IN VIBRATION-BASED ENERGY HARVESTER.	5
FIGURE 1.4 SCHEMATIC OF ELECTROMAGNETIC CONVERSION MECHANISM.	5
FIGURE 1.5 SCHEMATIC OF PIEZOELECTRIC CONVERSION MECHANISM: A) AT APPLIED COMPRESSIVE STRESS AND B) AT APPLIED TENSION. [19]	6
FIGURE 1.6 SCHEMATIC OF ELECTROSTATIC CONVERSION MECHANISM USING PARALLEL PLATE CAPACITOR.	6
FIGURE 1.7 MOLECULAR STRUCTURE OF CYTOP WITH END GROUP 'X'. [32]	8
FIGURE 1.8 FIRST ELECTRET VIBRATION ENERGY HARVESTER BY JEFIMENKO AND WALKER. [46]	8
FIGURE 1.9 OVERVIEW OF THE PROTOTYPED ELECTRET VIBRATION GENERATOR: A) PACKAGED PROTOTYPE IN CERAMIC CASE, B) TOP SI SUBSTRATE AND, C) BOTTOM GLASS SUBSTRATE. [48]	9
FIGURE 1.10 ROTATIONAL ELECTRET ENERGY HARVESTER: A) ELECTRODE DESIGN, B) PACKAGED PROTOTYPE AND, C) OUTPUT POWER FROM ARM SWING EXPERIMENT	9
FIGURE 1.11 ELECTROSTATIC CONVERSION CYCLE WITH EXTERNAL VOLTAGE SOURCE.	10
FIGURE 1.12 WORKING PRINCIPLE OF ELECTRET VIBRATION GENERATOR.	11
FIGURE 1.13 BASIC CONFIGURATION OF PARALLEL PLATE CAPACITOR.	11
FIGURE 1.14 SCHEMATIC OF DIFFERENT TYPES OF ELECTROSTATIC/ELECTRET GENERATORS: (A) GAP-CLOSING, (B) OVERLAPPING-AREA-CHANGE AND, (C) PERMITTIVITY CHANGE.	12
FIGURE 1.15 DIFFERENT ELECTRODE CONFIGURATIONS FOR ELECTROSTATIC/ELECTRET ENERGY HARVESTERS: A) INTERDIGITAL ELECTRODE FOR OVERLAPPING-AREA-CHANGE [50], B-C) PARALLEL PLATE ELECTRODE FOR GAP-CLOSING TYPE [51, 52], D) COMB-DRIVE ELECTRODE FOR GAP-CLOSING/OVERLAPPING-AREA-CHANGE [53], E) PARALLEL PLATE ELECTRODE WITH ENCAPSULATED HIGH PERMITTIVITY LIQUID FOR PERMITTIVITY CHANGE TYPE [54, 55] AND, F) INTERDIGITAL ELECTRODE FOR PERMITTIVITY CHANGE TYPE [56].	14
FIGURE 1.16 SCHEMATIC OF INTERDIGITAL ELECTRODES FOR ELECTROSTATIC/ELECTRET ENERGY HARVESTER, WHERE THE CAPACITANCE BETWEEN ELECTRODE FINGERS DOMINATES IN TOTAL PARASITIC CAPACITANCE (C_p).	15
FIGURE 1.17 EFFECT OF PARASITIC CAPACITANCE ON THE OUTPUT POWER OF ELECTRET/ELECTROSTATIC ENERGY HARVESTER [58].	16
FIGURE 1.18 A) ILLUSTRATION OF TWO LONG CONDUCTIVE WIRES WITH RADIUS R , SEPARATED BY THE DISTANCE D [59] AND B) THE SCHEMATIC OF CAPACITANCE BETWEEN FLAT ELECTRODES [60].	16
FIGURE 1.19 COMPARISON OF C_p CALCULATION RESULTS USING DIFFERENT MODELS AND EXPERIMENTAL DATA [64].	18
FIGURE 1.20 MODIFICATION FOR C_p REDUCTION; A) CONCAVITIES AT INTERDIGITAL GAP [63] AND B) SUSPENDED ELECTRODE ON PARYLENE-C STRUCTURE [64].	19
FIGURE 1.21 ELECTRET GENERATOR WITH HIGH ISOTROPIC PERMITTIVITY FLUIDS; (A) MERCURY-IN-THE-GAP [65], (B) GLYCERIN-IN-THE-GAP [64], (C) DI-WATER-IN-THE-GAP (INOUE ET AL.) [66] AND, (D) DI-WATER-IN-THE-GAP (CHEN ET AL.) [67]	19
FIGURE 1.22 ILLUSTRATION OF PARASITIC CAPACITANCE C_{p2} IN DIELECTRIC GAP, PROPORTIONAL TO THE TRANSVERSE PERMITTIVITY ϵ_{1x} OF DIELECTRIC GAP.	20

FIGURE 1.23 SIMULATION OF ROTATIONAL ELECTRET GENERATOR USING ISOTROPIC AND ANISOTROPIC PERMITTIVITY FLUID WITH FIXED TRANSVERSE PERMITTIVITY.	21
FIGURE 2.1 ILLUSTRATION OF LIQUID CRYSTAL PHASES [71].	25
FIGURE 2.2 SCHEMATIC OF LIQUID CRYSTALS THAT HAVE A) POSITIVE ANISOTROPIC PERMITTIVITY WHICH HAS DIPOLE ALONG LONGITUDINAL AXIS AND B) NEGATIVE ANISOTROPIC PERMITTIVITY WHICH HAS DIPOLE ALONG TRANSVERSE AXIS [72] AND, C) THE EXAMPLE OF THE POSITIVE ANISOTROPIC PERMITTIVITY LIQUID CRYSTAL WHICH HAS PHASE TRANSITION TEMPERATURE T_c [73].	26
FIGURE 2.3 MOLECULAR STRUCTURES OF COMMON NEMATIC LIQUID CRYSTALS: A) 5CB AND B) BCH-5F.F.F. THE DIPOLE MOMENTS ARE AT THE SHORT END OF AROMATIC RINGS.	27
FIGURE 2.4 SETUP OF IMPEDANCE ANALYZING: A) SCHEMATIC DIAGRAM AND B) THE PHOTO OF THE SETUP.	28
FIGURE 2.5 LIQUID CRYSTAL CELL FROM INSTEC; A) ITS PHOTO, B) ITS SCHEMATIC DIAGRAM AND, C) ITS EQUIVALENT ELECTRICAL CIRCUIT MODEL. THE TOTAL ELECTRODE AREA IS 5MM X 5MM. THE GAP IS 5 μ M.	28
FIGURE 2.6 MEASURED RESISTIVITY AND PERMITTIVITY OF POLYIMIDE AS A FUNCTION OF FREQUENCY [78].	29
FIGURE 2.7 CHANGE IN RELATIVE PERMITTIVITY AS A FUNCTION OF ELECTRIC FIELD STRENGTH.	30
FIGURE 2.8 MEASURED ANISOTROPIC PERMITTIVITY OF BASIC NEMATIC LIQUID CRYSTALS.	31
FIGURE 2.9 FREQUENCY DEPENDENCY OF LCs' RELATIVE PERMITTIVITIES. BLACK DOT LINES INDICATE 1000 AND 10 Hz FREQUENCY.	31
FIGURE 2.10 REAL PART OF THE MEASURED TOTAL IMPEDANCE OF LIQUID CRYSTAL CELL WITH THE CURVE FITTING FROM EQ. (2.5).	32
FIGURE 2.11 1-D ELECTROSTATIC MODEL OF ELECTROSTATIC VIBRATION ENERGY HARVESTER.	33
FIGURE 2.12 SCHEMATIC OF FABRICATION FLOW FOR THE ELECTROSTATIC VIBRATION ENERGY HARVESTER.	36
FIGURE 2.13 PHOTO OF FABRICATED ELECTRODE FOR ELECTROSTATIC VIBRATION ENERGY HARVESTER	36
FIGURE 2.14 SCHEMATIC OF POWER GENERATION EXPERIMENTAL SETUP.	37
FIGURE 2.15 PHOTO OF EXPERIMENTAL SETUP.	38
FIGURE 2.16 OUTPUT VOLTAGE WAVEFORM OF DIFFERENT PERMITTIVITY FLUIDS AT ITS CORRESPONDING OPTIMAL LOAD RESISTANCE..	39
FIGURE 2.17 OUTPUT POWER VERSUS EXTERNAL LOAD RESISTANCE OF ELECTROSTATIC VIBRATION ENERGY HARVESTER WITH AIR, FC-3283, 5CB AND, BCH-5F.F.F AS DIELECTRIC MEDIUM.	39
FIGURE 2.18 SURFACE POTENTIAL DECAY UNDER THE CONTACT OF LOW RESISTIVITY FLUIDS.	41
FIGURE 2.19 INVERSE PROPORTIONAL RELATION BETWEEN RESISTIVITY AND ANISOTROPIC PERMITTIVITY CHARACTERISTICS OF LC. [85]	41
FIGURE 2.20 (A) RELATIVE PERMITTIVITY OF MLC-7030 COMPARED TO BCH-5F.F.F. AND (B) FREQUENCY DEPENDENCY OF MLC-7030'S RELATIVE PERMITTIVITIES.	42
FIGURE 2.21 RESISTIVITY OVER ELAPSED TIME OF MLC-7030 WITH DIFFERENT CONDITIONS OF IMPURITY/HUMIDITY CONTROL.	43
FIGURE 2.22 SCHEMATIC OF SOFT-X-RAY CHARGING TECHNIQUE.	43
FIGURE 2.23 (A) SCHEMATIC OF SURFACE CHARGE DECAY EXPERIMENT AND (B) PHOTO OF ELECTRODE FOR THE EXPERIMENT WITH 15 μ M-THICK ELECTRET. GREEN ELLIPSOID REPRESENTS LC IN THE GAP.	44

FIGURE 2.24 NORMALIZED SURFACE POTENTIAL OVERTIME OF CHARGED ELECTRET UNDER DIRECT CONTACT WITH MLC-7030 IN UNCLEANED AND CLEANED STATES. INITIAL SURFACE POTENTIAL IS ABOUT -1kV.	44
FIGURE 2.25 EXPERIMENTAL SETUP WITH IMPURITY/HUMIDITY CONTROL FOR LC-ENHANCED ELECTRET VIBRATION ENERGY HARVESTER	45
FIGURE 2.26 RELATIVE HUMIDITY INSIDE SEALED EXPERIMENTAL SETUP OVERTIME AFTER INTRODUCING N ₂ GAS.	45
FIGURE 2.27 OUTPUT VOLTAGE WAVEFORM OF CONVENTIONAL AIR GAP ELECTRET GENERATOR AND MLC-7030-FILLED-GAP ELECTRET GENERATOR.	46
FIGURE 2.28 OUTPUT POWER VERSUS LOAD RESISTANCE AT 0 TH HOUR WITH CONVENTIONAL AIR GAP AND LC-FILLED GAP.	47
FIGURE 2.29 DECAYED OF NORMALIZED OUTPUT POWER OVERTIME BETWEEN UNCLEANED, CLEANED BUT NOT SEALED AND, CLEANED AND SEALED LC-ENHANCED ELECTRET VIBRATION ENERGY HARVESTER.	47
FIGURE 3.1 SCHEMATIC OF 1-D ELECTROSTATIC MODEL WITH FIELD-DEPENDENT PERMITTIVITY.	50
FIGURE 3.2 (A) SCHEMATIC OF LC MOLECULE ALIGNMENT INSIDE THE PARALLEL PLATE CAPACITOR WITH DIELECTRIC GAP G AND (B) RELATION OF LC PERMITTIVITY INSIDE THE GAP AND ITS ALIGNMENT ANGLE θ ACCORDING TO EQ. (3.4) AND (3.5).	52
FIGURE 3.3 SCHEMATIC OF FTIR SPECTROSCOPY WITH POSITIVE ANISOTROPIC LIQUID CRYSTAL SHOWN AS BLUE ELLIPSOID. WHEN THE ELECTROMAGNETIC AXIS OF IR BEAM PARALLEL TO THE LIQUID CRYSTAL MOLECULE, THE ABSORBANCE WILL BE HIGH, VICE VERSA.	53
FIGURE 3.4 SCHEMATIC OF FABRICATION PROCESS FLOW FOR FT-IR TEST CELL.	53
FIGURE 3.5 PHOTO OF FINISHED FT-IR TEST CELL AND THE SCHEMATIC OF ITS CROSS-SECTION	53
FIGURE 3.6 SCHEMATIC OF THE SETUP FOR MICROSCOPIC FTIR SPECTROSCOPY, PHOTO OF MICROSCOPIC FT-IR SPECTROMETER AND, ITS ZOOM-IN PHOTO OF THE SETUP.	55
FIGURE 3.7 RELATIONSHIP BETWEEN IR ABSORBANCE, RELATIVE PERMITTIVITY AND, ELECTRIC FIELD STRENGTH.	55
FIGURE 3.8 (A) IR ABSORBANCE OF BCH-5F.F.F IN FT-IR TEST CELL WITH AND WITHOUT ELECTRIC FIELD AND ITS CORRESPONDING (B) AXIAL PERMITTIVITY AND (C) ALIGNMENT ANGLE. GREEN ELLIPSOIDS REPRESENT THE INTERPRETED ALIGNMENT OF LC AT EACH REGION.	57
FIGURE 3.9 LIGHT BENDING PRINCIPLE OF LC UNDER POM. WHEN LC'S PLANAR ALIGNMENT IS IN-BETWEEN CROSS-POLARIZER, THE LIGHT IS BEND. VERTICAL ALIGNMENT POSES NO LIGHT BENDING CAPABILITY	59
FIGURE 3.10 PHOTOS OF A) FINISHED ELECTRODES FOR POM EXPERIMENT AND ZOOM-IN IMAGE.	59
FIGURE 3.11 SCHEMATIC OF POM EXPERIMENTAL SETUP.	60
FIGURE 3.12 PHOTOS OF THE INSIDE OF ENVIRONMENTAL CHAMBER.	60
FIGURE 3.13 PHOTO OF THE ENVIRONMENTAL CHAMBER AND THE ZOOM-IN PHOTO OF CRANK MECHANISM.	61
FIGURE 3.14 RELATIONSHIP BETWEEN PERMITTIVITY, LUMINESCENCE AND, ELECTRIC FIELD STRENGTH.	61
FIGURE 3.15 RELATIVE PERMITTIVITY AS A FUNCTION OF LUMINESCENCE.	62
FIGURE 3.16 OUTPUT POWER VERSUS LOAD RESISTANCE OF GENERATOR WITH POM SETUP..	63
FIGURE 3.17 POM IMAGES OF LC-ENHANCED ELECTRET VIBRATION ENERGY HARVESTER DURING OPERATION AT OPTIMAL RESISTANCE AND ITS INTERPRETATION OF RELATIVE PERMITTIVITY IN 1 PERIOD.	64

FIGURE 3.18 POM IMAGES OF LC-ENHANCED ELECTRET VIBRATION ENERGY HARVESTER DURING OPERATION AT OPTIMAL RESISTANCE AND ITS INTERPRETATION OF RELATIVE PERMITTIVITY AND ALIGNMENT ANGLE INSIDE THE GENERATOR WITHIN 1/2 PERIOD.	65
FIGURE 3.19 POM IMAGES OF LC-ENHANCED ELECTRET VIBRATION ENERGY HARVESTER DURING OPERATION IN OPEN CIRCUIT CONDITION AND ITS INTERPRETATION OF RELATIVE PERMITTIVITY AND ALIGNMENT ANGLE INSIDE THE GENERATOR WITHIN 1/2 PERIOD.	66
FIGURE 3.20 HORIZONTAL PERMITTIVITY AT INTERDIGITAL GAP OF CHARGE-COLLECTOR ELECTRODE OVERTIME IN DIFFERENT CONDITIONS; AT OPTIMAL RESISTANCE, SHORT CIRCUIT TO GROUND AND, OPEN CIRCUIT CONDITION. EACH PLOT IS THE AVERAGE OF N=20 DATA SET. BLACK LINE IS THE FIT LINE FROM EQ. (3.10).	67
FIGURE 3.21 ESTIMATION OF LC MOLECULE ALIGNMENT AT INTERDIGITAL GAP UNDER CHARGED AND GROUNDED ELECTRET WHEN ASSUMING NO INTERMEDIATE ALIGNMENT.	67
FIGURE 3.22 SCHEMATIC OF LC MOLECULE ALIGNMENT IN PRESENT AND IDEAL ALIGNMENT .	67
FIGURE 3.23 SIMULATED PARASITIC CAPACITANCE BETWEEN A) PRESENT ALIGNMENT AND B) IDEAL ALIGNMENT.	68
FIGURE 3.24 COMPARISON BETWEEN EXPERIMENTAL DATA, 1-D ELECTROSTATIC MODEL FROM EQ.(3.1), CONSTANT C_p , AND (3.11), DYNAMIC C_p .	69
FIGURE 3.25 SIMULATED OUTPUT POWER ENHANCEMENT OF LC-ENHANCED ELECTRET VIBRATION ENERGY HARVESTER COMPARED TO CONVENTIONAL AIR GAP AS A FUNCTION OF ANISOTROPIC PERMITTIVITY IN A) PRESENT ALIGNMENT AND B) IDEAL ALIGNMENT. BLACK SOLID LINE INDICATES FLUID WITH $\Delta\epsilon=5$.	70
FIGURE 3.26 MEASURED VISCOSITY OF NEMATIC LIQUID CRYSTALS AS A FUNCTION OF ANISOTROPIC PERMITTIVITY. [90] BLACK SOLID LINE IS THE FIT OF AVERAGE VISCOSITY TO ANISOTROPIC PERMITTIVITY. BLACK DASH LINE PROJECTED THE VISCOSITY OF MLC-7030 TO THE EQUIVALENT ANISOTROPIC PERMITTIVITY ACCORDING TO FIT LINE.	71
FIGURE 3.27 RATIO BETWEEN ELECTROSTATIC DAMPING FORCE AND VISCOUS DAMPING FORCE FROM DIFFERENT ANISOTROPIC PERMITTIVITY FLUIDS AS A FUNCTION OF ROTATIONAL VELOCITY AT VARIED SURFACE POTENTIAL.	73
FIGURE 3.28 COMPARISON OF FOM AND POWER ENHANCEMENT BETWEEN DIFFERENT FLUIDS.	74
FIGURE 4.1 SCHEMATIC AND EXAMPLES OF ION TRAPPING MECHANISMS; (A) CHEMISORPTION AND (B) FERROELECTRICITY.	78

LIST OF TABLES

TABLE 1.1 POTENTIAL AMBIENT ENERGY SOURCES AND ITS DEMONSTRATED CAPABILITIES. [8]	3
TABLE 1.2 ACCELERATION AND FREQUENCY OF FUNDAMENTAL VIBRATION MODES FOR VARIOUS SOURCES. [11]	4
TABLE 2.1 PHYSICAL PARAMETERS OF INSTEC'S LIQUID CRYSTAL CELL.....	30
TABLE 2.2 PHYSICAL PARAMETERS OF FABRICATED ELECTROSTATIC VIBRATION ENERGY HARVESTER.	35
TABLE 2.3 EXPERIMENTAL CONDITIONS FOR OUTPUT POWER GENERATION EXPERIMENT.....	37
TABLE 2.4 ENHANCEMENT AND ANISOTROPIC PERMITTIVITY.	39
TABLE 2.5 COMPARISON BETWEEN MEASURED AND SIMULATED C_p OF DIFFERENT PERMITTIVITY FLUIDS.....	40
TABLE 3.1 SIMULATION PARAMETERS FOR OUTPUT POWER OF LC-ENHANCED ELECTRET VIBRATION HARVESTER.	70
TABLE 3.2 SIMULATION PARAMETERS FOR ESTIMATION OF VISCOUS LOSS COMPARED TO OUTPUT POWER.....	72

Acknowledgements

First and foremost, I would like to express my sincere gratitude to my supervisor, Prof. Yuji Suzuki, for his full supports, valuable advices and kind guidance. From the time when he kindly accepted me as his research/visiting student in the summer of 2013, to the continuation of my master degree since spring of 2015, until my decision to pursue doctoral degree from 2018, I have been under his cares and guidance for almost 7 years. He is always professional and on point during discussion but, he also has patience to explain I misunderstood/confused. I am very grateful for his teaching to forge me into independent and active researcher.

The second person I would like to express my appreciation to is our laboratory's secretary, Mrs. Goda. She has helped me regarding many of my documents; whether it is school-related document, government-related document and many more. Without her help, I might get deport due to errors in documentation. On the road of my study here, I would also like to extend my honest gratitude to our faculty members; Morimoto-sensei for his advices in simulation methods, Lee-san for his support and guidance on ALD+MEMS-related process and life, Miyoshi-san for his service in design and build the experimental setup and knowledge in liquid crystal, Suzuki-san for her aid in electret and MEMS process, and Hamana-san for his support on technical problems, whether it is computer-related or machinery. I would also like to express my thankfulness to my professor in Thailand, Prof. Pimpin, who had taught me the basic of MEMS technology and introduced me to energy harvesting papers/works before joining this lab.

I would also like to express my thankfulness to my PhD defense's committee members, Prof.Kato, Prof.Delauney, Prof.Shiomi and, Prof.Kumada, for their comments and suggestions regarding my works; it gives me a lot to think and consider about how to improve my thesis.

Next, I would like to thanks my friends in Suzuki-Morimoto lab from 2015-2022 for their discussions, comments and, topics; both research and life. For my longtime colleagues, Oh-san, Xie-san, Lu-san and, Jin-san. For the one who already graduated and pursuing their life, R. Chen-san, Liang-san, Fu-san, Wan-san, Y.C. Chen-san, Kim-san, Yeh-san, Zhao-san and, Liu-san; they are ones of the inspirations for my pursuit of doctoral degree. Also, H. Wang-san for her discussion about liquid crystal; both experimental and simulation knowledge.

To my family, I would like to sincerely express my appreciation to my sister, Dr. Preechaya Kittipaisalsilpa (as of July 2021), and my father, Mr. Tasapol Kittipaisalsilpa, for their continued and caring support, in both my physical and mental health. Starting with the time I have to prepare myself after heartrending event to the time with my persisting health issues after living here. I hope that with the completion of my study, it would make their sacrifice meaningful.

Last but not least, I would like to express my utmost gratitude to my mother, Mrs. Sirilak Chareonchaisit, who raised me with all the best she could. Thank you for your love and care. I wish that she could be with me at this moment. I am still thinking of her often and it gives me the push to continue with my work when I am down.

Sincerely,
Kasidis Kittipaisalsilpa
(Namo)

Abstract

Low-frequency vibration-based electrostatic/electret energy harvester is an attractive candidate for powering low-power electronics in Internet-of-Things due to many reasons; such as, abundant energy source, compatibility with MEMS technology, and high output power at small volume compared to other energy harvesting methods. On the other hand, the current performance of such generator still cannot consistently meet the energy demand of wireless sensor nodes. Thus, it is called for further development to obtain higher output power at given conditions.

One way to enhance its output power is to introduce high permittivity fluid into its dielectric gap. However, parasitic capacitance (C_p) existing between 2 sets of electrode fingers has negative effect on its output power. Correlation model for C_p has illuminated the dependency of horizontal permittivity in dielectric gap (ϵ_x) and substrate permittivity (ϵ_s) while capacitance change ΔC is proportional to vertical permittivity in the gap (ϵ_y). In other word, if high isotropic permittivity ($\epsilon_x = \epsilon_y$) fluid is used, the increase of ϵ_x , i.e. C_p , will limit the potential enhancement of the generator.

This thesis aims to overcome this challenge by enhancing the output power through the increase ΔC while limiting the increase of C_p through the use of high anisotropic permittivity ($\epsilon_x \neq \epsilon_y$) fluid; especially the ones with $\epsilon_y > \epsilon_x$, which should greatly boost ΔC with its large ϵ_y while limit the increase of C_p with its smaller ϵ_x . Nematic liquid crystal (LC) is chosen as anisotropic permittivity fluid.

Nematic LC is an interesting material which retain both crystalline order, like solid, and fluid properties. It exhibits anisotropic permittivity and can align its molecular axis with electric field. The electrical characterization for LC is conducted using impedance analyzing technique. Impedance analyzer not only measures its axial ϵ_{\parallel} and transverse ϵ_{\perp} permittivities but, also its resistivity and threshold voltage can be observed. Common nematic LCs, 5CB ($\epsilon_{\parallel}=18$ and $\epsilon_{\perp}=6$) and BCH-5F.F.F ($\epsilon_{\parallel}=13$ and $\epsilon_{\perp}=4$), are chosen for introductory testing. Preliminary output power generation experiment with electrostatic vibration energy harvester has been conducted. With 5CB and BCH-5F.F.F, the enhancements of output power are respectively 87 and 67 times higher compared to that conventional air-in-the-gap. C_p is measured and its ϵ_x is founded to be similar to isotropic permittivity of LC ($\epsilon_{iso}=(\epsilon_{\parallel}+2\epsilon_{\perp})/3$).

On the other hand, it is widely known that the electret has poor surface charge stability with low resistivity fluid. With the characteristics of LC that resistivity is the inversely proportional to anisotropic permittivity ($\Delta\epsilon=(\epsilon_{\parallel}-\epsilon_{\perp})$), it leads to the trade-off between generator's life time and its output power. To verify this, we choose the high resistivity LC, MLC-7030 ($\epsilon_{\parallel}=6$ and $\epsilon_{\perp}=2.8$), which has bulk resistivity of $10^{16} \Omega\cdot\text{cm}$. With MLC-7030, the maximum output power is $139 \mu\text{W}$ at $68 \text{ M}\Omega$ which is 7-times higher compared to that of air gap ($19.8 \mu\text{W}$). On the other hand, LC is known to be easily contaminated by ionic impurity and absorption of water vapor. The implement of impurity/humidity control can lead to the realization of high resistivity. Cleaning and isolation methods have been implemented. Preliminary experiment is performed with LC cells in 3 conditions; (1) uncleaned, (2) cleaned with IPA in ultrasonic bath and, (3) sealed after cleaning with low-impurity epoxy. With adequate impurity/humidity control of (3), high resistivity of LC can be realized for a long time while (2) cannot retain high resistivity overtime and (1) results in very low resistivity. By mimicking condition (3) with cleaned generator and keeping low humidity with the introduction of N_2 gas, LC-enhanced electret vibration energy harvester is realized for the first time. High output power could be kept for over 40 hours. This also suggests that further

impurity/humidity suppression is necessary for long-term performance of such generator which will be discussed in later part.

For further development of LC-enhanced electret vibration generator, accurate output power model is needed. This calls for the detailed investigation of molecule alignment inside LC-enhanced electret generator. 2 measurements are performed; static molecule alignment and dynamic molecule alignment. For static molecule alignment, Fourier-transform infrared spectrometer (FT-IR) with narrow-band detector and spatial resolution of $9 \times 9 \mu\text{m}^2$ is used. The molecule alignment can be captured by sensing the characteristic absorption of axial bonds. Test cell is fabricated from CaF_2 substrate with patterned ITO electrode and coated with rubbed polyimide alignment layer for initial planar alignment. BCH-5F.F.F is chosen due to its easily noticeable characteristic bonds. From the preliminary test, relation between IR absorbance and permittivity is established. It is founded that the LC molecules gradually change their alignment over the interdigital gap from horizontal alignment (i.e., ε_{\perp}) at grounded electrode to vertical alignment (i.e., ε_{\parallel}) at electrode with strong electric field from applied voltage. The misalignment at interdigital gap is caused by the fringe electric field between high-voltage electrode and other grounded electrodes. Estimation of about $100 \mu\text{m}$ from electrode edge in actual generator has been affected from the misalignment during idle state. The effect is progressively lessened until no change in alignment is observed under both grounded and charged electrodes. Hence, the overall alignment, i.e. average ε_y , under each region does not significantly affected by the misalignment.

Dynamic molecule alignment data is captured using polarized optical microscopy (POM) equipped with high-speed camera. By utilizing the cross-polarizer, alignment of LC can be determined. Electret vibration generator with ITO electrodes is fabricated with Al_2O_3 insulation layer and CYTOP-EGG as electret. It is charged to -1kV with soft x-ray charging technique. An environmental chamber equipped with high-speed camera is employed to isolate generator from outside humidity and observe the alignment. MLC-7030 is chosen for this measurement due to its high resistivity. From preliminary test, POM images can be interpreted into ε_x , ε_y and, alignment angle θ . Output power generation experiment is performed and POM images is captured at optimal resistance. Real-time in-situ alignment change of LC has been observed for the first time. It reveals that the alignment at interdigital gap is periodically changing and mostly affected by high electric field from charged electret. Consequently, time-averaged C_p is slightly larger compared to the correlation model. At low $\Delta\varepsilon$ but large ε_s , the effect of dynamic alignment at interdigital gap may be small. But, with large $\Delta\varepsilon$ and ε_s , the effect could be more noticeable. Similar to results from FT-IR, the alignment at charged electret region maintains constant vertical alignment due to high electric field strength of electret. On the other hand, LC molecules align quite horizontally in grounded area. Furthermore, it should also be noted that effects of oscillating flow and unsteady electric field are negligible due to high electric field strength of electret.

Based on LC characteristics and information on molecule alignment, this study develops 1-D electrostatic model with field-dependent permittivity and dynamic C_p . The present model agrees well with the experimental results. The performance of LC-enhanced electret vibration energy harvester is predicted using the proposed 1-D model by comparing its electrostatic damping force and viscous damping force, which represents output power and viscous loss, respectively. Due to the limit of $\Delta\varepsilon$ for high resistivity is 5, the upper limit of output power enhancement is 12. Viscous loss by LC is approximated using rotational electret energy harvester model. It is found to be dependent on rotational speed rather than $\Delta\varepsilon$, i.e. viscosity, of LC. With MLC-7030, viscous loss is estimated to be about 1/9 of electrical output power. Figure of Merit (FoM) for comparing the output power enhancement effects of different fluids is defined. Comparing to isotropic liquids,

both power enhancement and FoM of MLC-7030 with $\Delta\epsilon=3.2$ are much higher at about 17 and 14.4, respectively.

In regards to impurity/humidity control for LC, this thesis proposes the use of ferroelectric material for impurity/humidity control in LC-enhanced electret generator. (Withheld)

In summary, the present thesis aims to enhance the output power through the boost of ΔC while limit the increase of C_p using nematic LC. Output power enhancement of up to 90 times has been achieved with electrostatic vibration energy harvester and common LCs. To prevent the discharge, high-resistivity nematic LC, MLC-7030, with anisotropic permittivity is employed. With adequate impurity and humidity control, LC-enhanced electret vibration generator has been realized for the first time with 7-times higher output power compared to conventional air gap. High output power is kept for over 40 hours. Static and dynamic LC molecule alignment inside generator has been illuminated with FT-IR and POM for the first time. C_p is founded to be periodically alternated and affected by strong electric field from charged electret. Based on FT-IR and POM experimental data, 1-D electrostatic output power model with field-dependent permittivity and dynamic C_p has been developed. The model agrees well with experimental data. Performance prediction of LC-enhanced electret vibration energy harvester is made. Its viscous loss is estimated by ratio of electrostatic damping force and viscous damping force. Figure of merit is also defined for comparing power enhancement of different fluids. Impurity control with the use of ferroelectric material has been employed to further suppress the discharge. (Withheld)

Chapter 1

Introduction

1.1 Energy Demand in IoT and WSN

In the recent years, the advancement of fabrication and manufacturing technology like MEMS (Micro Electro Mechanical Systems) technology leads us to smaller, cheaper and, less power-consuming electronics [1]. Not just mobile phone or television, but it also includes microsensors and wearable devices. Those small electronics like sensors play an important role toward the realization of Internet of Things (IoT). Concept of IoT has given birth to many beneficial applications; such as, healthcare monitoring, smart home, autonomous vehicles and, smart security (Figure 1.1). For many IoT applications, wireless sensor networks (WSN), consisting of millions of sensors, are very essential cog wheels which enable the interactions between users and the surrounding environment [2]. It has been predicted that the global market value of WSN will be over 80 billion dollars within 2022 [3]. Such that, many research and development has been focusing on the field of WSN.

Like any other electronics devices, sensors in WSN also require the power source to operate, even as low-power consumption as it can be. The current energy source, i.e. coin battery, may be sufficient to operate the sensor node; but, the issue arises when billions of sensor nodes is operated on batteries alone. The use of batteries become less attractive due to their short lifetime and resultant toxic wastes which cause the heavy burden to the environment. Energy harvesting has been considered a promising alternative power source for the WSN. Due to its principle of generating power, rather than storing-and-releasing like battery, energy harvesters could last longer than any battery and need less care after being deployed. This could relieve the troubles and costs of replacing batteries for sensor nodes and wastes generated from used battery. Moreover, this could enable us to employed them in the hard-to-access or hazardous environments.

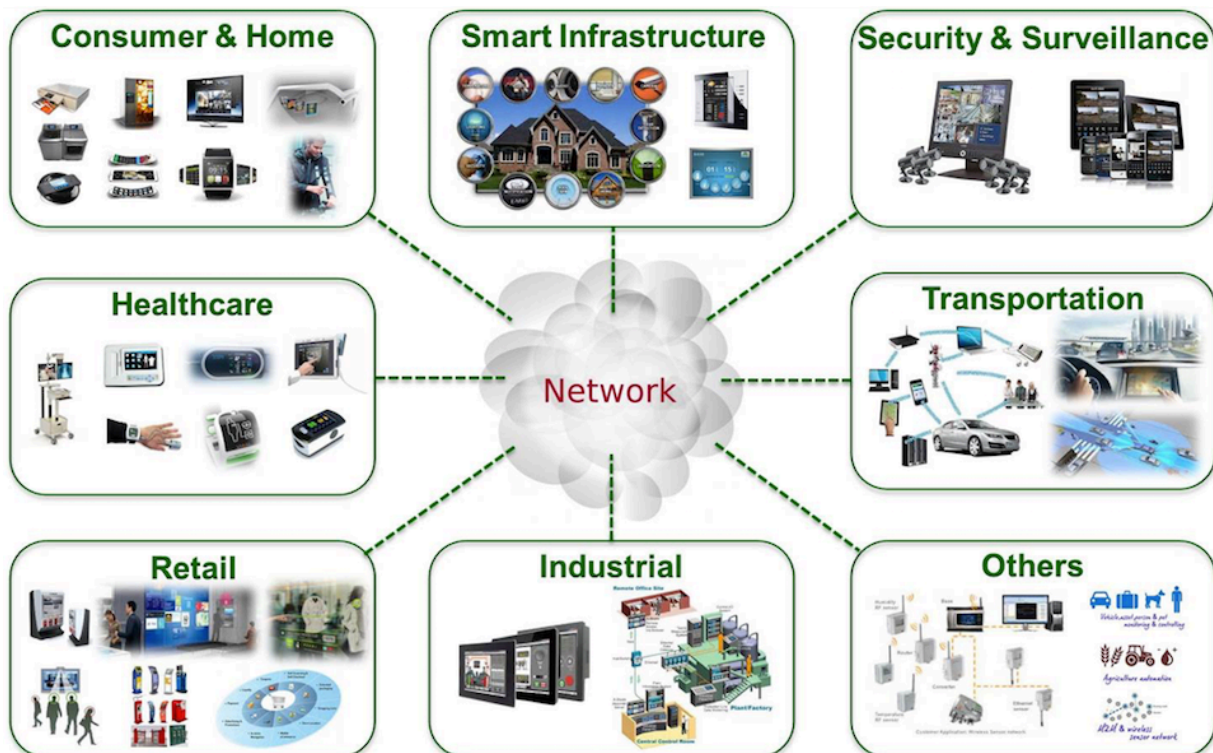


Figure 1.1 Various fields that could be benefitted from Internet of Things (IoT). [4]

1.2 Energy Harvesting

Energy Harvesting is a concept of collecting and making use of natural energy, such as, kinetic energy in the wind/water current or geothermal energy from underground; mostly turning them into electricity. In the present days, it is possible to scavenge and utilize the ambient energy in the environment due to the development of MEMS technology. The trivial but ubiquitous energy, such as ambient light, radio frequency, body heat, small vibration and, human movement can be collected and converted into electricity as shown in Figure 1.2.

Table 1.1 lists the power density of each ambient energy source. As shown, the scavenged energy can be range from less than $1 \mu\text{W}$ to 1 mW in the scale of cm^2 or cm^3 . Though the harvested energy may seem small compared to Li-ion battery [5, 6], it is already possible to power the low-power consumption electronics. For instance, a wireless sensor node which has data transmission rate of hundreds of kbits/s over a several tens of meter distance with 1% radio duty cycle, its power

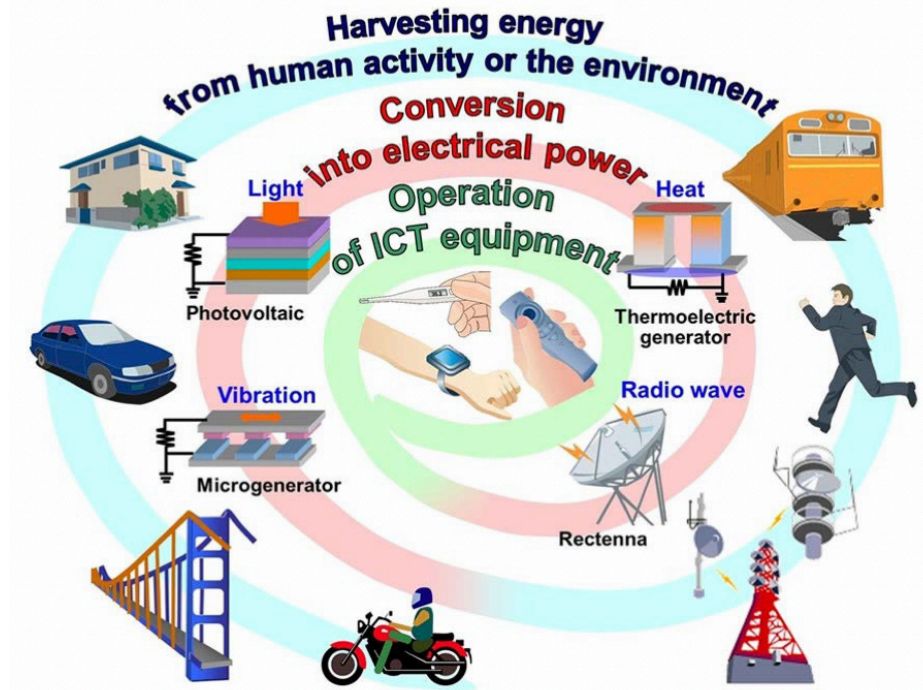


Figure 1.2 Different kind of ambient energy sources for energy harvesting [7]

Table 1.1 Potential ambient energy sources and its demonstrated capabilities. [8]

Energy Source	Performance
Ambient radio frequency	$< 1 \mu\text{W}/\text{cm}^2$
Ambient light	$100 \mu\text{W}/\text{cm}^2$ (illuminated office) $100 \text{ mW}/\text{cm}^2$ (directly toward bright sun)
Thermoelectric	$60 \mu\text{W}/\text{cm}^2$
Vibrational microgenerators	$4 \mu\text{W}/\text{cm}^3$ (human motion, Hz level) $800 \mu\text{W}/\text{cm}^3$ (machine, kHz level)
Ambient airflow	$1 \text{ mW}/\text{cm}^2$

consumption is 1-10 μW [9]. Another exceptional example is the Seiko's Thermic Watch which can run continuously on body heat generated 1 μW [10].

1.1.1 Vibration-based Energy Harvesting

Obviously, there is no best ambient energy source or harvesting method but, it undeniably strongly depends on which application or the surrounding environment being used with/for. If looking from the viewpoint of energy source's availability, it is unquestionable that the ambient vibration source is the most omnipresent. It can be founded in numerous scenarios; such as, human motion, piping vibration, structural vibration, etc. Roundy et al. [11] listed some of common vibration sources in daily life and measured their acceleration magnitude and frequency data for fundamental vibration mode in Table 1.2. It is founded that the potential ambient vibration sources mainly exist at low frequency fundamental mode around 100 Hz or less. This is a crucial information for designing vibration-based energy harvesters.

Most of the vibration-based energy harvesters has the same basic concept which follows 2-step conversion: i) mechanical-to-mechanical and ii) mechanical-to-electricity conversion, as shown in Figure 1.3. For the first one, it consists of the mass-spring system which converts surrounding ambient vibration into the relative motion/vibration for the system. The mass-spring system is designed to amplifies the relative motion for generating output power in the later conversion.

For the vibration-based energy harvester, the main mechanical-to-electrical conversion mechanisms can be separated into 3 methods; electromagnetic, piezoelectric and, electrostatic [11] [12] [13] [14].

Electromagnetic mechanism is based on the electromagnetic induction principle in Faraday's law. As shown in Figure 1.4, the relative motion of the conductive coils and magnetic field induced the electron's movement; resulting in current generation. This is the widely used basic principle in macro-scale power plant. This method is very self-sufficient and only relies on the external excitation force for moving the inductive coils. On the other hand, the performance of the micro-scale electromagnetic vibration generator is usually limited by its size, though the high output current can be achieved. This is due to the difficulty to integrate the magnetic material into micro-scale device. So, for such generators, macro-scale coils and bulk magnets is usually

Table 1.2 Acceleration and frequency of fundamental vibration modes for various sources. [11]

Vibration source	a (m/s ²)	f_{peak} (Hz)
Car engine compartment	12	200
Door frame just after door closes	3	125
Blender casing	6.4	121
Secondary story floor of busy office	0.2	100
CD on notebook computer	0.6	75
Car instrument panel	3	13
HVAC vents in office building	0.2-1.5	60
Base of 3-axis machine tool	10	70
Person nervously tapping the heel	3	1

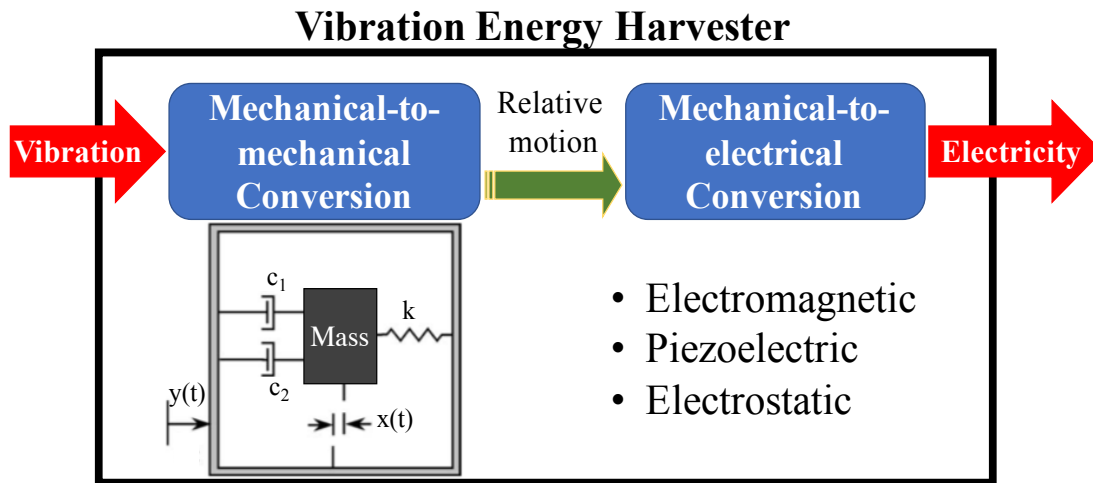


Figure 1.3 Typical conversion mechanisms in vibration-based energy harvester.

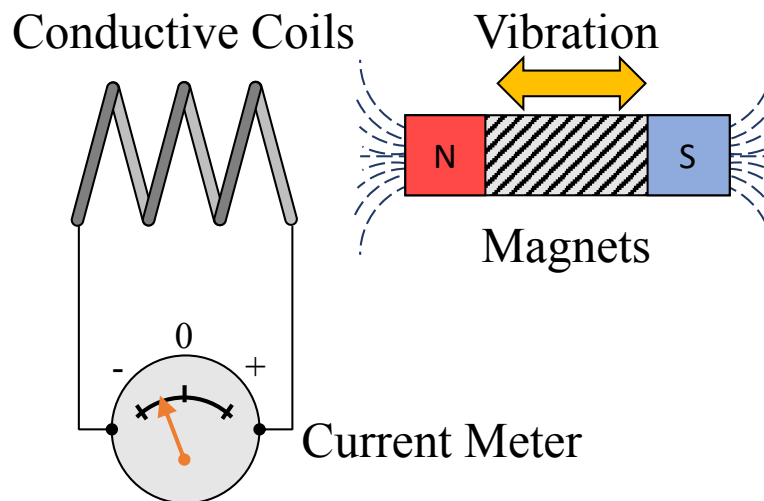


Figure 1.4 Schematic of electromagnetic conversion mechanism.

employed [14] [15] [16] [17] [18] which limits the possibility for the size reduction

For the piezoelectric mechanism, as its name implied, it is based on the piezoelectric effect, usually, from piezoelectric materials; such as, piezoceramic (e.g. lead zirconate titanate: PZT), polyvinylidene fluoride (PVDF), aluminum nitride (AlN) and, single crystal (e.g. quartz and lead titanate: PbTiO_3) [19]. Piezoelectric effect occurs when a certain crystal is under mechanical strain leading to electric polarization; resulted in the voltage difference across the material as shown in Figure 1.5. Many groups had been proposed the piezoelectric generator with high output power applicable with human motion and environmental vibration [20] [21] [22]. This method is quite attractive since it only relies on the material property to generate the output power. It is only limited by the integration of piezoelectric material onto micro-scale device.

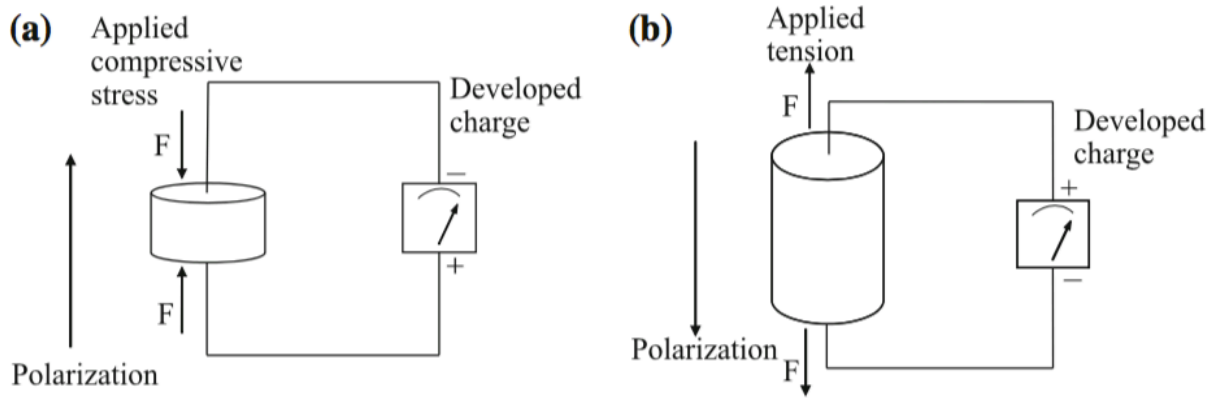


Figure 1.5 Schematic of piezoelectric conversion mechanism: a) at applied compressive stress and b) at applied tension. [19]

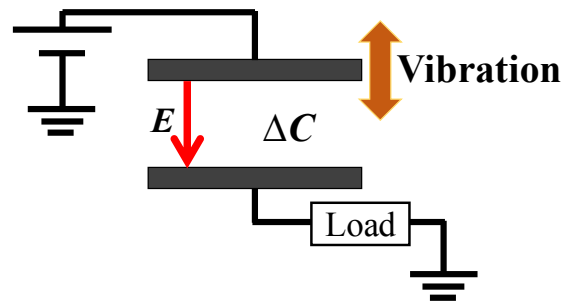


Figure 1.6 Schematic of electrostatic conversion mechanism using parallel plate capacitor.

Last but not least, electrostatic generator utilizes the variation of capacitance under the constant bias charge/voltage to convert mechanical energy into electricity as illustrated as Figure 1.6.

Compared to other 2 mentioned mechanisms, electrostatic type is easier to be implemented with micro-scale device since the capacitor structure (e.g. interdigital electrodes) are widely used in many fields [23] [24] [25] [26]. In addition, it has the advantage of high output power at low frequency compared to electromagnetic and piezoelectric type in the same micro-scale [27] [28] [29] [30] [31] [32]. On the other hand, this type of generator requires constant bias voltage/charge to operate; in other word, the external source is needed. The requirement of external voltage/charge source is solved by the development of ‘electret’ material [33] [34] [35] which can retain charges with high stability. It can be called ‘electrostatic/electret energy harvester’. In this study, we will focus on the energy harvesting using electrostatic mechanism or electrostatic/electret energy harvester.

1.2 Electret Materials

The secret to realization of electrostatic/electret energy harvester without external voltage/charge source. First described in 1732 by Gray about the long-term electrification of dielectric materials [33]. The term “Electret” later coined by Heaviside [36] is used to call for a class of dielectric material that possesses quasi-permanent electric polarization state or charges [34]. It is equivalent to electrostatic version of magnets. Afterwards, Eguchi [37] conducted systematic research about electret materials and its properties.

Electret materials can be grouped into 2 categories; inorganic ceramic-based electret and polymer-based electret. The examples for ceramic based-electrets are quartz (SiO_2) and hydroxyapatite (HA)/oxy-hydroxyapatite (OHA) [38] [39]. Sprenkels et al. [38] reported long-term charge stability of SiO_2 electret; although predicted to last for hundreds of years, it showed low value of surface potential (about -150 V). In 1996, Yamashita et al. [39] had demonstrated HA as electret with high surface potential but, at the cost of much thicker electret layer in millimeter (mm) scale. On the other hand, polymer electrets with fluoro-substituents, such as PVDF and CYTOP, shows promising capabilities for high surface potential with thin samples in micrometer scale [40] [41].

Among the polymer-based electrets, CYTOP shows the best performance in both long-term charge stability and high surface potential capability with μm -scale thickness. Figure 1.7 shows the molecular structure of CYTOP. It has been widely known that the end group of the CYTOP polymer chain has significant effect on electret performance [40]. Recently, computer simulation for electret development [42] [43] [44] [45] has been proposed which has very good agreement with experimental electron affinity value of electret. This could lead to the easier and less labor cost for future development of better electret materials. Kim et al. [43] employed quantum chemical analysis to investigate CYTOP electrets and proposed the new end group of Tris(2-aminoethyl)amine (TAEA) which achieved great improvement in term of charge stability at lower thermal cost. In 2021, Zhang et al. [45] proposed the high-performance polymer electret material based on CYTOP using deep-learning algorithm with another end group similar to TAEA; achieving almost -3000V surface potential for over 800 hours with $15\mu\text{m}$ -thick electret film.

1.3 Electrostatic/Electret Energy Harvester

The first demonstration of electret energy harvester was in 1970s by Jefimenko and Walker [46] (Figure 1.8). Later investigated and improved by Tada [47]. In 2003, Boland [27] proposed the integration of MEMS-based technology, the first micro electret energy harvester had been realized.

As mentioned before, electrostatic/electret energy harvester is attractive due to its high output power at low frequency and small volume. Furthermore, it is compatible with MEMS-based fabrication technology which enable it to be scaled down. In our group, many researches has been done in energy harvesting field, especially for electrostatic/electret energy harvester. For the example, Matsumoto et al. [48] has successfully prototyped MEMS electret-based energy harvester with output power of $6\mu\text{W}$ at 40 Hz vibration frequency as shown in Figure 1.9. Miyoshi et al. [49] has successfully obtained $80\mu\text{W}$ from an armswing using rotational electret energy harvester as shown in Figure 1.10.

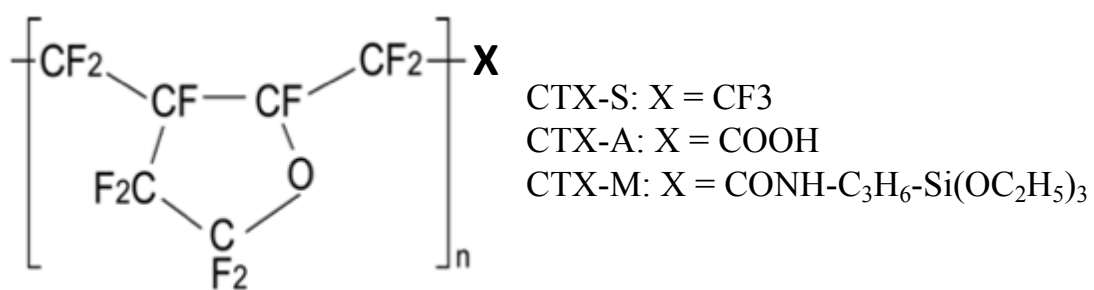


Figure 1.7 Molecular structure of CYTOP with end group 'X'. [32]

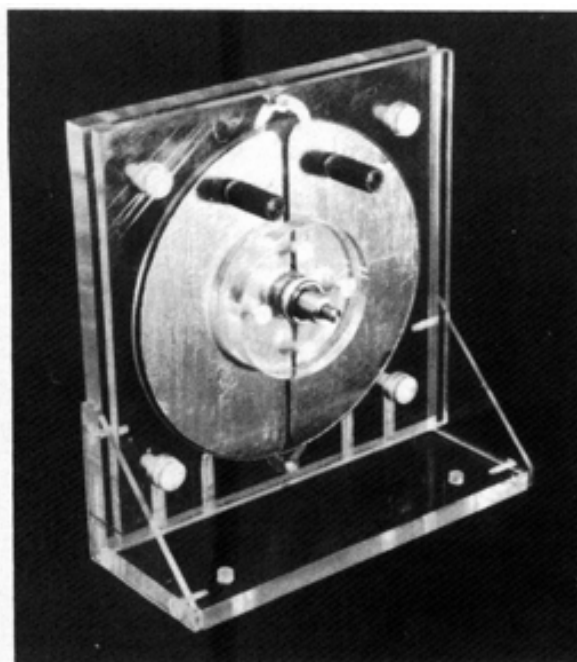


Figure 1.8 First electret vibration energy harvester by Jefimenko and Walker. [46]

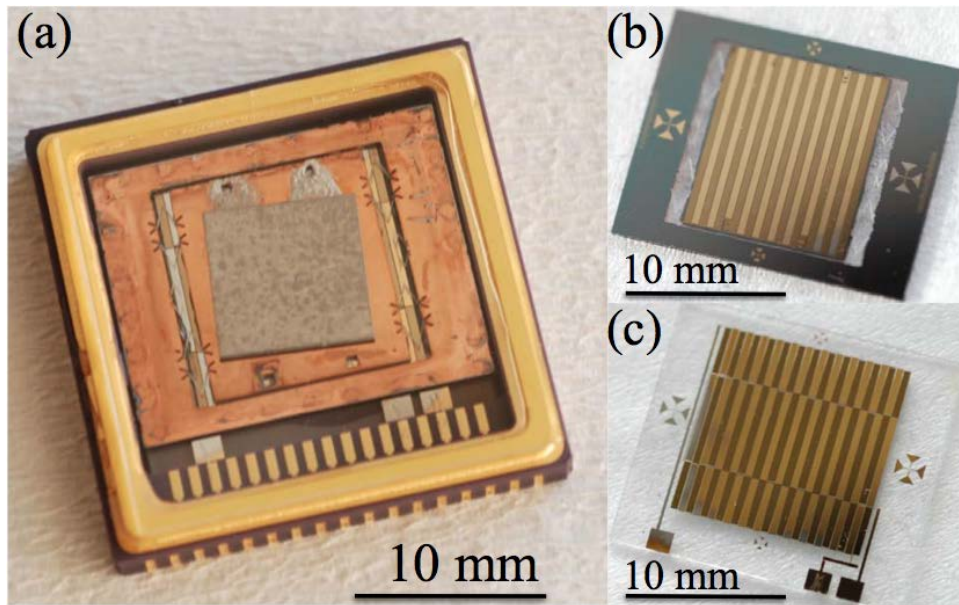


Figure 1.9 Overview of the prototyped electret vibration generator: a) packaged prototype in ceramic case, b) top Si substrate and, c) bottom glass substrate. [48]

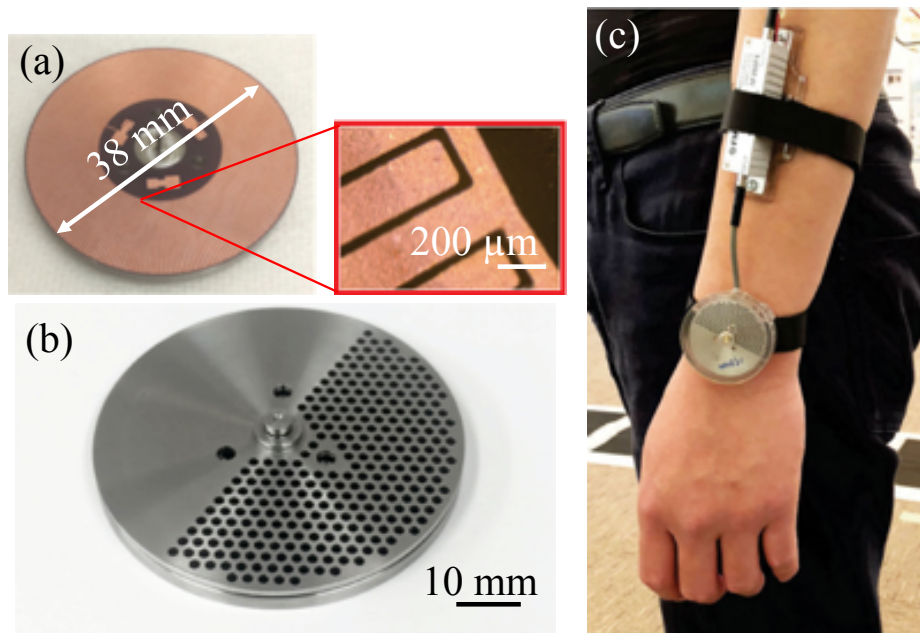


Figure 1.10 Rotational electret energy harvester: a) electrode design, b) packaged prototype and, c) output power from arm swing experiment

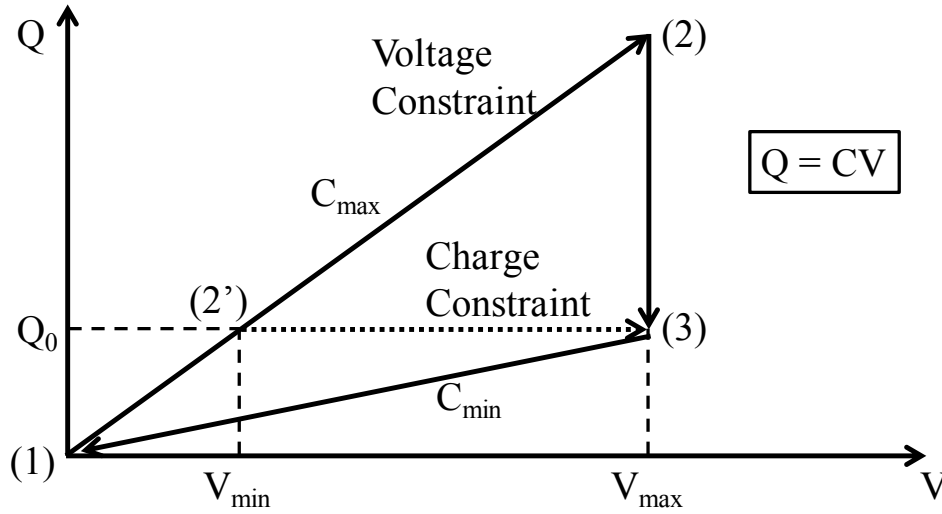


Figure 1.11 Electrostatic conversion cycle with external voltage source.

1.3.1 Working Principle

The basic principle electrostatic/electret energy harvester is relied on the change of the capacitance with charged surface(s). Figure 1.11 shows the Q-V diagram for electrostatic conversion cycle with external voltage source. It can be classified into 2 modes: charge-constrained and voltage constrained cycle.

In the charge-constrained cycle (Cycle 1-2'-3-1), the cycle starts when the capacitance reaches its maximum C_{max} . The device is then charged with electric charge Q_0 with voltage V_{min} . Next, the device configuration is mechanically move to find minimum capacitance C_{min} . As the charge is kept constant at C_{min} , the voltage reaches its maximum V_{max} . Then, the device is connected to external load. The net energy per cycle is given by

$$E_{12'31} = \frac{1}{2}(C_{max} - C_{min})V_{max}V_{min} = \frac{1}{2}(C_{max} - C_{min})Q_0^2 \quad (1.1)$$

In the same manner but slightly different, the voltage-constrained cycle (Cycle 1-2-3-1) starts with C_{max} while connected to voltage source. Then, the capacitance is decreased to C_{min} while voltage V_{max} is maintained. In this case, the net energy per cycle is

$$E_{1231} = \frac{1}{2}(C_{max} - C_{min})V_{max}^2 \quad (1.2)$$

On the other hand, when the electret material with embedded charge is employed as shown in Figure 1.12, assuming the in-plane overlapping area change scheme. The induced charge is generated on both electrode A and B which are in opposite side of electret plate. The movement of electret plate due to external vibration will cause the shift in induced charge between two electrode plates; resulting in electricity generation. Boland et al. [27] approximated the output power of electret-based energy harvester as the following relation

$$P \propto \Delta C \sigma^2 \quad (1.3)$$

where ΔC is the change in capacitance ($C_{max} - C_{min}$) and σ is the surface charge potential on electret.

From all equation (1.1), (1.2) and, (1.3), we could clearly see that the change of the capacitance between C_{max} and C_{min} or ΔC is an important key for the net energy gained and output power for electrostatic/electret energy harvester. To maximize this, we should look into the configuration of electrode.

1.3.2 Electrode Configuration

In electrostatic/electret energy harvester, the base configuration is that of capacitor. The basic capacitance equation of parallel plate capacitor is given as; $C = \epsilon_0 \epsilon_r A / g$, where C is a capacitance, ϵ_0 is permittivity of free space, ϵ_r is relative permittivity of the gap, A is the overlapping area and, g is the thickness of the gap as shown in Figure 1.13. From the equation, it can be seen that there are 3 possible types for variation; gap-closing, overlapping-area-change and, permittivity change. Figure 1.14 shows the different configuration of variable capacitor.

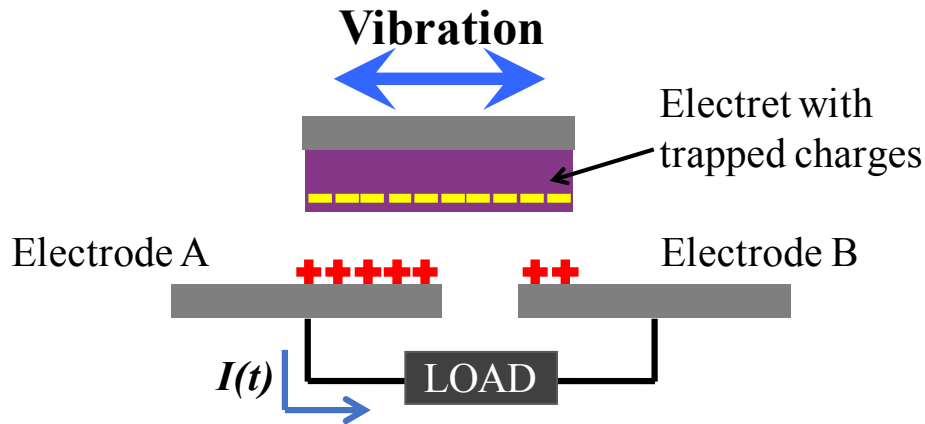


Figure 1.12 Working principle of electret vibration generator.

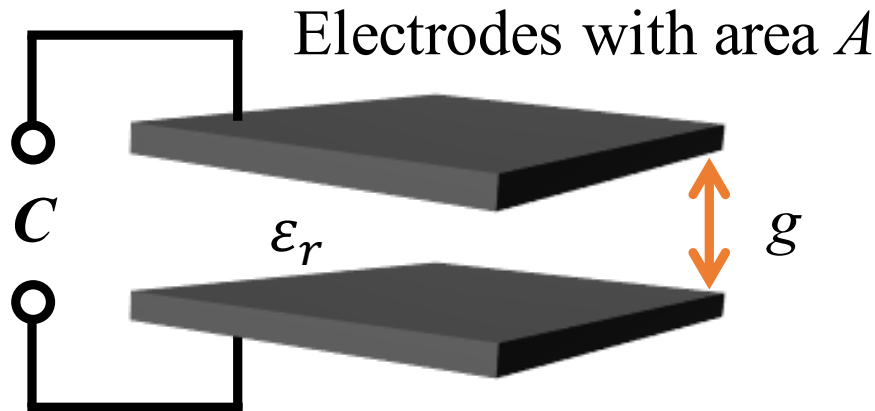


Figure 1.13 Basic configuration of parallel plate capacitor.

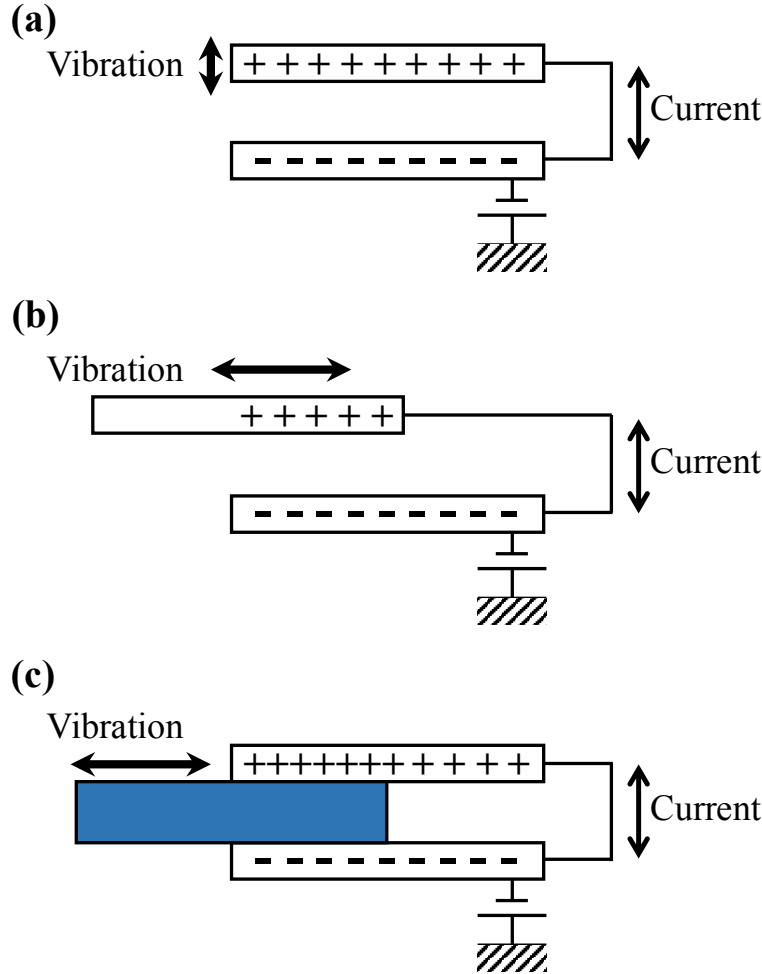


Figure 1.14 Schematic of different types of electrostatic/electret generators: (a) gap-closing, (b) overlapping-area-change and, (c) permittivity change.

In the gap-closing type, one of the electrodes is vibrating causing the gap to be larger and smaller periodically. From this, we can derive the rate of change of the capacitance as equation (1.4);

$$\frac{dC}{dt} = -\epsilon_0 \epsilon_r \frac{A}{g(t)^2} \frac{dg}{dt} \quad (1.4)$$

In the overlapping-area-change type, one of electrode is sliding while maintain the constant gap causing the change in overlapping area. So, the rate of change of capacitance is

$$\frac{dC}{dt} = \frac{\epsilon_0 \epsilon_r}{g} \frac{dA}{dt} \quad (1.5)$$

For the permittivity change type, the dielectric layer with high relative permittivity is sliding between a pair of parallel electrodes. This can be seen as the change of the area with relative permittivity ϵ_r . Thus, the rate of change of capacitance can be written as

$$\frac{dC}{dt} = \frac{\epsilon_0(\epsilon_{r'} - \epsilon_r)}{g} \frac{dA}{dt} \quad (1.6)$$

where $\epsilon_{r'}$ is the permittivity of high dielectric material.

Based on above mentioned types, many has proposed electrostatic/electret energy harvester with different electrode configuration to utilize different types of capacitance variation as shown in Figure 1.15. For instance, Paracha et al. [50] and Matsumoto et al. [48] use the two interdigital electrodes to form an in-plane overlapping-area-change energy harvester. Wang and Hansen [51] only use one parallel plate capacitor scheme to create out-of-plane gap-closing electret energy harvester. While Feng et al. [52] utilize two parallel plate capacitors connected in series to realize out-of-plane gap-closing electret energy harvester. On the other hand, Fu et al. [53] uses comb-drive electrode configuration to achieve gap-closing and overlapping-area-change in one generator. Bu et al. [54] use high relative permittivity liquid encapsulated in between fixed parallel plate capacitor to create permittivity-change electrostatic energy harvester. While Huynh et al. [55] and Takahashi et al. [56] utilize interdigital electrode to harvest the vibration energy through relative permittivity change using moving high relative permittivity liquid and solid, respectively. Recently, Adachi et al. [57] has successfully prototyped overlapping-area-change rotational electret energy harvester using closed loop interdigital electrode.

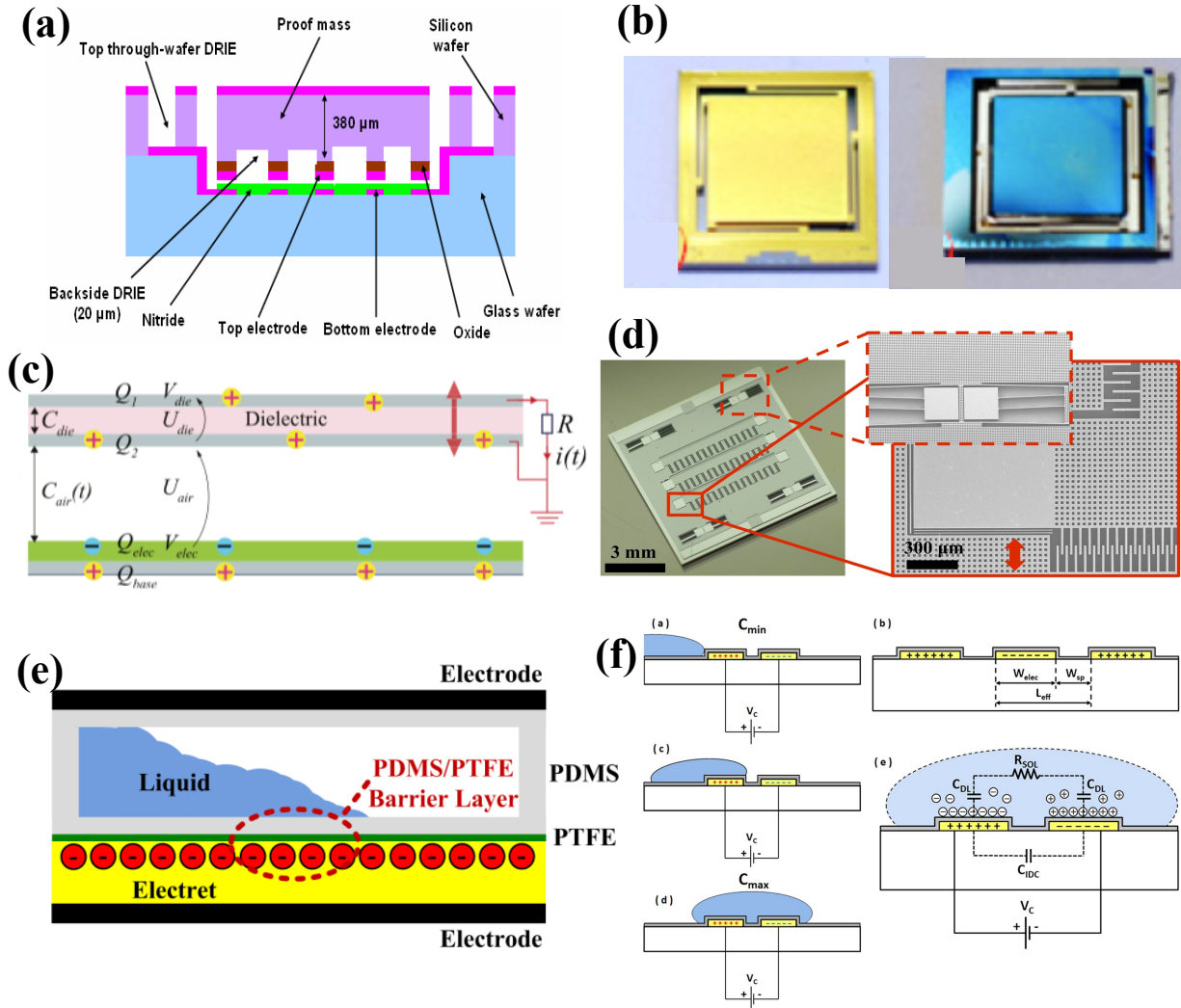


Figure 1.15 Different electrode configurations for electrostatic/electret energy harvesters: a) interdigital electrode for overlapping-area-change [50], b-c) parallel plate electrode for gap-closing type [51, 52], d) comb-drive electrode for gap-closing/overlapping-area-change [53], e) parallel plate electrode with encapsulated high permittivity liquid for permittivity change type [54, 55] and, f) interdigital electrode for permittivity change type [56].

1.3.3 Output Power Modelling for Electret Vibration Generator

To understand the output power of electrostatic/electret energy harvester, we should first understand its principle model. For electret energy harvesters, there is a commonly used formula derived by Boland et al. [27] for estimating the maximum output power as the following.

$$P_{max} = \frac{\sigma^2 \cdot n A_0 f}{4 \frac{\epsilon_2 \epsilon_0}{d} \left(\frac{\epsilon_2 g}{\epsilon_1 d} + 1 \right)} \quad (1.7)$$

where σ is the electret surface charge density, ϵ_0 is the permittivity of free space, ϵ_1 is the relative permittivity of air (or gap-filled dielectric) and, ϵ_2 is the dielectric of the electret material. g and d are thickness of the air gap (or dielectric material) and electret, respectively. A_0 , n and, f are respectively defined as the maximum overlapping area, the number of the poles and, the rotational frequency. In spite of the fact that equation (1.7) is derived for rotational overlapping-area change electret energy harvester, it is still useful for investigation of the factors related to the output power of other electret vibration generators. This will be used to discuss in the later part in this chapter.

1.4 Parasitic Capacitance and its effect

Parasitic capacitance (Here after C_p) is one of the constrain in electrostatic/electret energy harvester; especially, in-plane overlapping-area-change using interdigital electrodes. It is originated in both external circuit and generator itself; usually the C_p of generator is dominant over that of external circuit. For in-plane overlapping vibrational energy harvester, C_p mainly exists between finger of interdigitated electrode as shown in Figure 1.16. It can be separated into 2 parts; C_p that originated from substrate and dielectric gap, C_{p1} and C_{p2} respectively.

In 2009, Bartsch et al. [58] had incorporated the effect of parasitic capacitance to the output power for rotational electret generator (1.5). The derived analytical expression is as following

$$P = \frac{d^2 \sigma^2 R}{\epsilon_0^2 \epsilon_2^2 (R + R_i)^3} \{R + R_i - 4C_p n f R R_i \tanh(M)\} \quad (1.8)$$

where $M = (R + R_i)/4C_p n f R R_i$. R and R_i is the external and optimal load resistance, respectively.

As seen in equation (1.8), the existence of C_p causes the output power to be lower than its ideal case. The effect of parasitic capacitance on the output power using rotational energy harvester is demonstrated using external capacitor connected parallel to the generator as shown in Figure 1.17. As predicted from the model, the large parasitic capacitance results in lower output power compared to the small one; by slightly increase C_p from 15 to 37 pF, output power has decreased by half. Further increase of C_p could result in change of the output power by the order-of-magnitude.

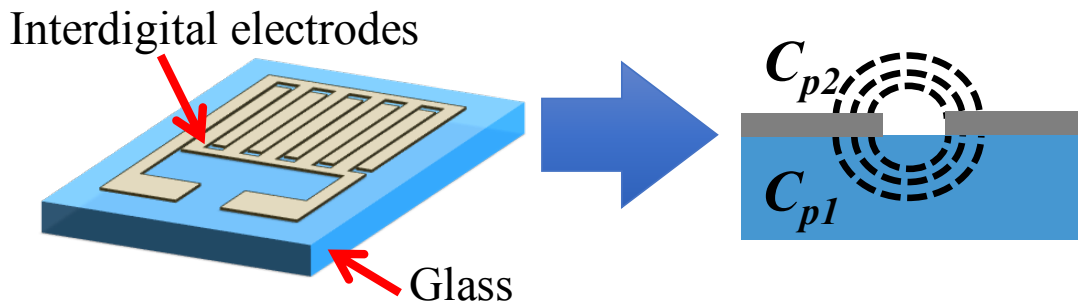


Figure 1.16 Schematic of interdigital electrodes for electrostatic/electret energy harvester, where the capacitance between electrode fingers dominates in total parasitic capacitance (C_p).

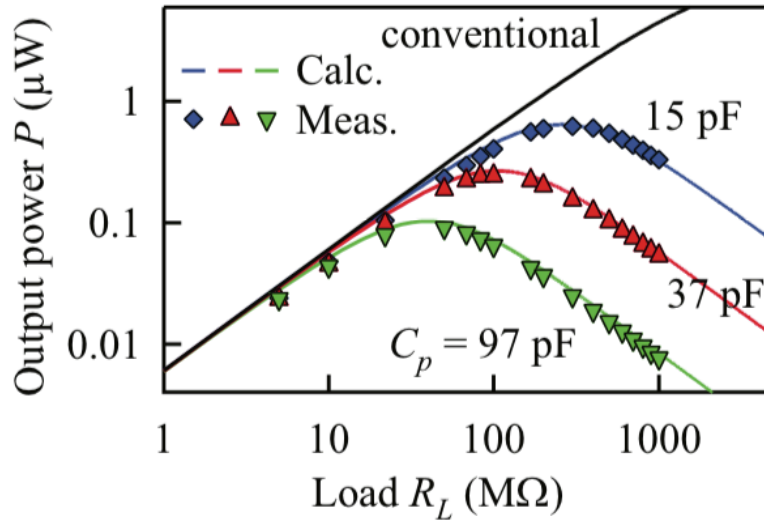


Figure 1.17 Effect of parasitic capacitance on the output power of electret/electrostatic energy harvester [58].

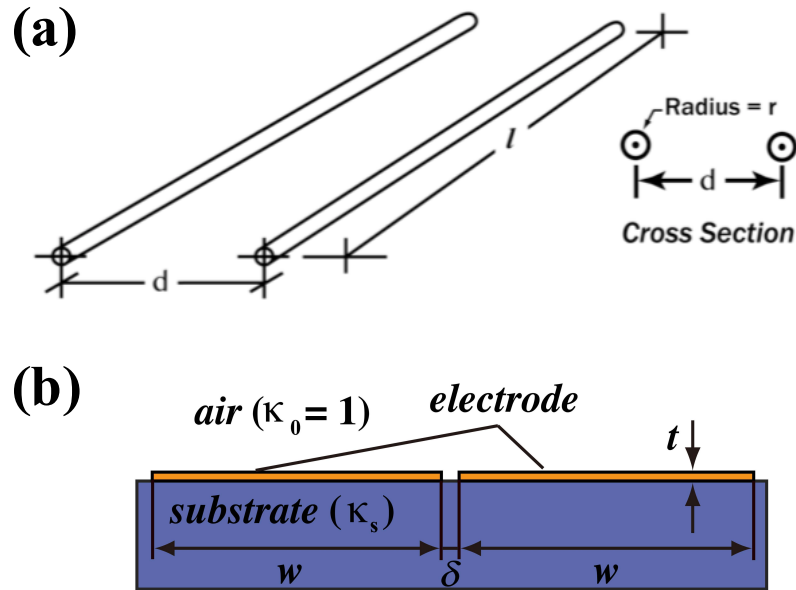


Figure 1.18 a) Illustration of two long conductive wires with radius r , separated by the distance d [59] and b) the schematic of capacitance between flat electrodes [60].

1.4.1 Modelling of C_p

Many researches have been proposed about the model for C_p in electrostatic energy harvester. Method such as finite element method (FEM) [58] has been used but, the calculation is not so straightforward. Looking back to the general design of the in-plane overlapping electrostatic generator, interdigitated electrodes are used. This type of electrode can be seen widely used in other fields such as gas sensor and actuator. Conformal mapping technique [61] [62] has been used to calculate the interdigital capacitance with the high accuracy. The principle of this technique is to solve the complex problem by projecting the element into other domain while preserving local information; making the problem becomes less complex. Although the technique is less effort-consuming unlike FEM, it is still complicated.

On the other hand, C_p of interdigitated electrode can also be viewed as capacitance of parallel conductive wires as shown in Figure 1.18a and its equation is shown as eq. (1.9). The detailed derivation can be found in [59]. Charles S. Walker [60] explained the capacitance between horizontal flat electrodes as shown in Figure 1.18b; the equation is given as (1.10).

In the work of Masaki et al. [63], the model of C_p is proposed with the creepage distance between electrodes instead of the displacement between it for the interdigitated electrode with concavities at interdigitated gap; the equation is shown as eq. (1.11). In the previous study in our group, Chen and Suzuki [64] proposed the analytical expression based on the parallel conductive wires as shown in eq. (1.12).

Parallel conductive wires [59]

$$C = \frac{\pi \epsilon_0 \epsilon_r l}{\ln \left[\frac{d}{2r} + \sqrt{\left(\frac{d}{2r} \right)^2 - 1} \right]} \text{ or } C \approx \frac{\pi \epsilon_0 \epsilon_r l}{\ln(d/r)} \text{ (when } \frac{2r}{d} \ll 1) \quad (1.9)$$

Charles S. Walker [60]

$$C = \frac{\pi \epsilon_0 k_{eff} l}{\ln \left(\frac{\pi \delta}{w + t} + 1 \right)} \quad (1.10)$$

Masaki et al. [63]

$$C = \frac{\pi \epsilon_0 k_s l}{\ln \left(\frac{\delta - t}{0.5t} \right)} \quad (1.11)$$

Chen and Suzuki, correlation model [64]

$$C = \frac{\pi \epsilon_0 k_{eff} l}{\ln[\alpha + \sqrt{\alpha^2 - 1}]} \quad (1.12)$$

where $\alpha = \frac{\pi}{2} \cdot \frac{1 + \delta/w}{1 + t/w}$ and $k_{eff} = \frac{\epsilon_1 + \epsilon_s}{2}$

In the eq. (1.9), when the distance between two conductive wires is very small compared to wire's diameter, the capacitance formula can be reduced to the right-most equation. As for eq. (1.10), k_{eff} representing the effective permittivity is used instead of ϵ_r because of the effect of substrate's permittivity. ϵ_1 is the relative permittivity in dielectric gap. w and t is defined as width and thickness of electrode. In the case of Masaki et al. (eq. (1.11)), the model is in the assumption

of very small distance between electrode plates resulted in elimination of square root term. k_s is the substrate permittivity. As for Chen-Suzuki correlation model, it shows the close expression to the parallel conductive wires without the small distance assumption like eq. (1.11). α is equivalent to $d/2r$ in eq. (1.9).

In [64], the comparison between the theoretical result from different method and experiment is shown in Figure 1.19. It could be clearly understood that Charles' model of C_p is closer to the experimental results when the interdigitated gap is large due to the use of simplified parallel conductive wires' expression ($d \gg r$). Model from Masaki et al. shows the underestimation of the C_p which may be caused by the absence of electrode width in their model. Meanwhile correlation model from Chen and Suzuki shows the good agreement with the FEM and experimental results. So, we will use Chen-Suzuki model as the main method for calculation C_p in the study.

1.4.2 Reduction of C_p

Based on the understanding of C_p , it can be reduced by the modification of electrode design and materials (substrate and dielectric). Masaki et al. [63] create the concavities at interdigital gap and get 3-times higher output power compared to typical interdigital gap design as shown in Figure 1.22a. Chen and Suzuki [64] suspend interdigital electrodes on parylene-C structure; resulting in smaller k_{eff} and achieving 35% more output power compared to the conventional electrode design as shown in Figure 1.22b.

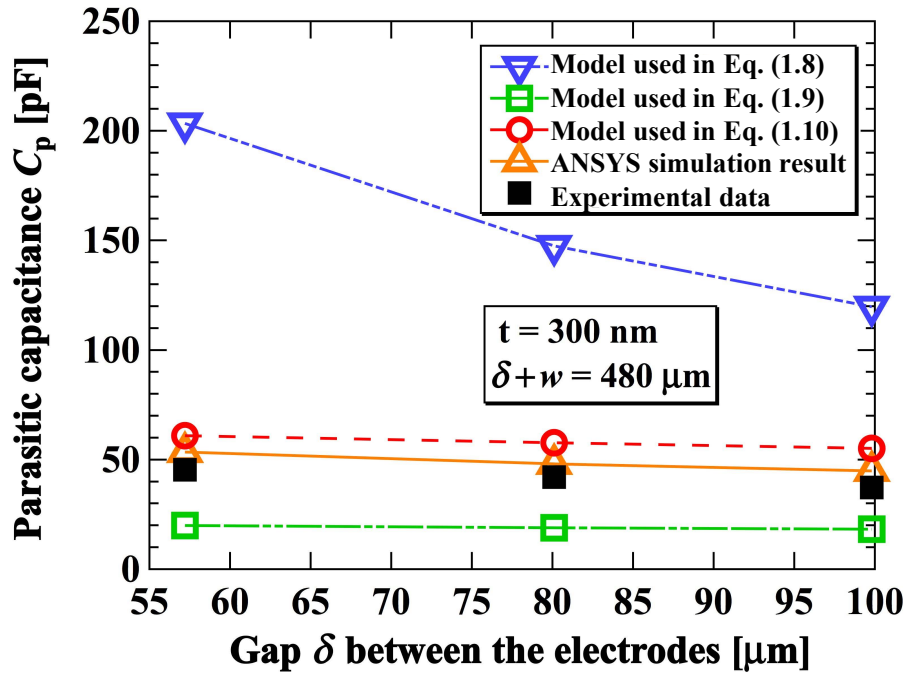


Figure 1.19 Comparison of C_p calculation results using different models and experimental data [64].

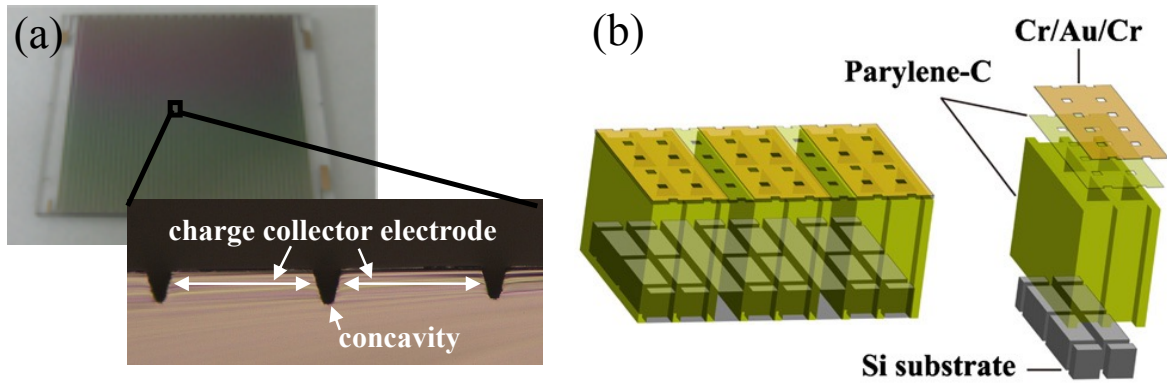


Figure 1.20 Modification for C_p reduction; a) concavities at interdigital gap [63] and b) suspended electrode on parylene-C structure [64].

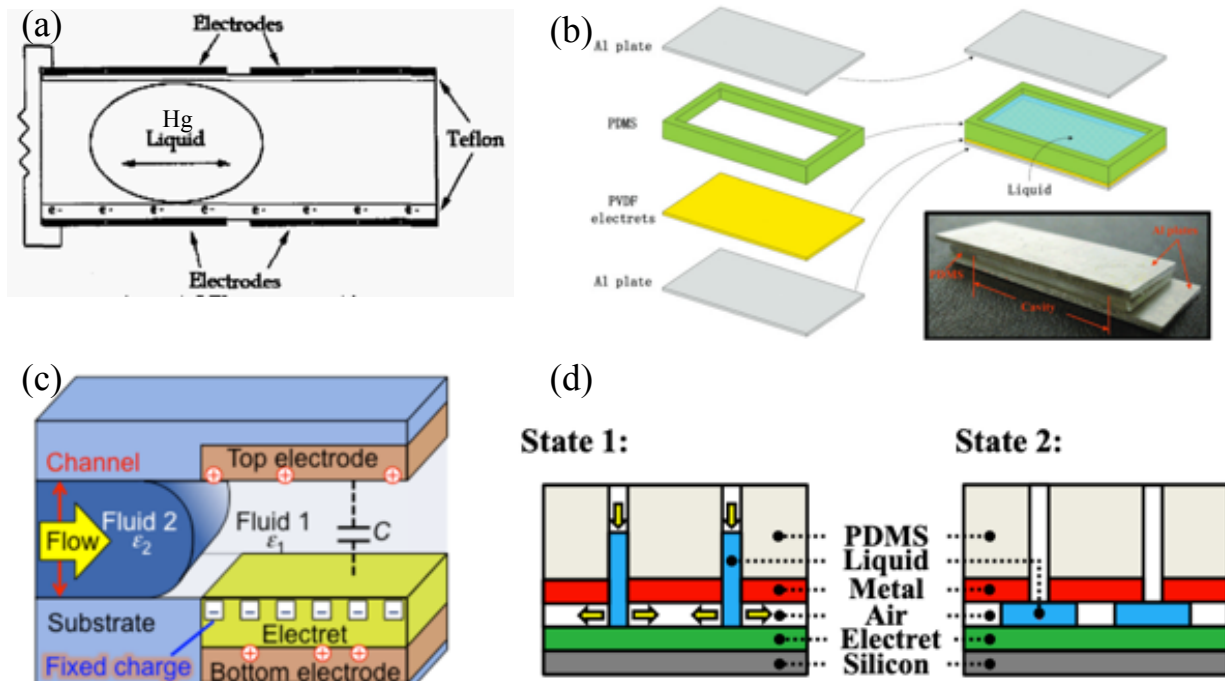


Figure 1.21 Electret generator with high isotropic permittivity fluids; (a)mercury-in-the-gap [65], (b)glycerin-in-the-gap [64], (c)DI-water-in-the-gap (Inoue et al.) [66] and, (d)DI-water-in-the-gap (Chen et al.) [67]

1.5 Strategy for Enhancing Output Power

Based on concept of capacitor, the easiest way to enhance the output power of electrostatic/electret vibration energy harvester is to enlarge its capacitance change ΔC by introducing high permittivity medium, such as fluid, into its dielectric gap. Though the concept of enhancing ΔC is simple, many attempted researches showed lower-than-expected output power even with high permittivity fluids. In 2005, Boland et al. [65] proposed the use of liquid mercury, which is conductive and has infinite permittivity, with corona-charged Teflon as electret material and achieved output power density of $0.31 \mu\text{W}/\text{cm}^2$. Bu et al. [68] utilized glycerin ($\epsilon_r=45.8$) with PVDF electret and generated

$0.36\mu\text{W}/\text{cm}^2$. These low output powers could be attributed to small amount of used fluid; resulting in less enhanced ΔC . Recently, Inoue et al. [66] and Chen et al. [67] reported the use of DI water in SiO_2 -electret vibration energy harvester and resulted in output power of $0.44\mu\text{W}/\text{cm}^2$ and $0.64\mu\text{W}/\text{cm}^2$, respectively. Figure 1.21 shows the schematics of mentioned examples.

Looking back to the output power modelling equation (1.8), we understand the relationship between output power and parasitic capacitance. Based on electret vibration generator model and Chen-Suzuki correlation model of parasitic capacitance, we can clearly see that the permittivity of dielectric gap plays an important role in the increasing the output power ($P \propto \epsilon_1$) while it also influences C_p through $k_{eff} (= (\epsilon_1 + \epsilon_s)/2$, where ϵ_s is a substrate permittivity). In other word, the increase of permittivity of dielectric gap will not improve the output power of the generator as much as expected due to the increase of C_p . That is one of the reasons of low power density in [65] [68] [66] [67] even though the very high permittivity fluids are used.

On the other hand, if we could use the material that has anisotropic permittivity (axial permittivity \neq transverse permittivity or $\epsilon_{\parallel} \neq \epsilon_{\perp}$), since C_p is proportional to ϵ_{\perp} as shown in Figure 1.22, we could increase the capacitance change while limit the increase of C_p . This may lead to the enhancement of output power without much power-reduction effect from C_p .

For demonstration, by using the output power analytical expression for rotational electret energy harvester [58] with the dielectric gap of $100\text{ }\mu\text{m}$ and estimated parasitic capacitance by conformal mapping, we could estimate the increase of output power when using isotropic and anisotropic permittivity material as shown in Figure 1.23. It clearly shows that, with the anisotropic permittivity, the output power could be increase by 100 times compared to that of the conventional one when the axial permittivity becomes close to 50. While the conventional generator with high isotropic permittivity seems to reaches the output power enhancement limit at the same permittivity of 50 with the enhancement of 10 times compared to that of air gap. Thus, the anisotropic permittivity is necessary to further improve the output power of such generator.

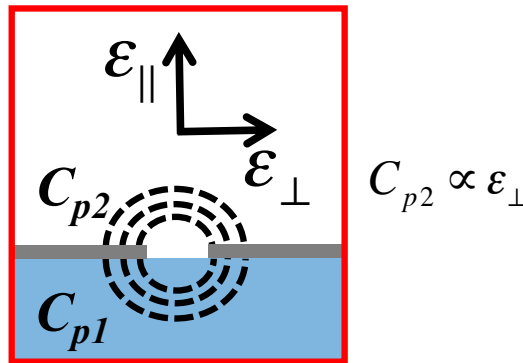


Figure 1.22 Illustration of parasitic capacitance C_{p2} in dielectric gap, proportional to the transverse permittivity ϵ_{1x} of dielectric gap.

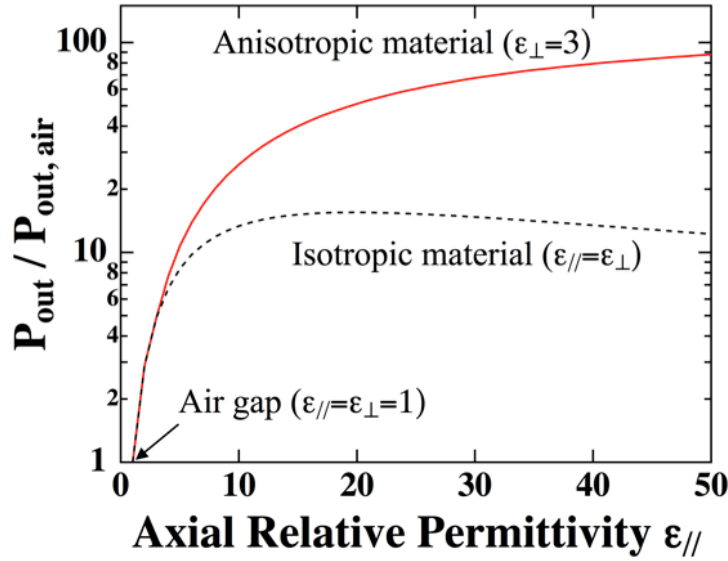


Figure 1.23 Simulation of rotational electret generator using isotropic and anisotropic permittivity fluid with fixed transverse permittivity.

1.6 Objectives and Thesis Organization

The main objective of the present study is to achieve the output power enhancement of electrostatic/electret vibrational energy harvester by boosting the capacitance change (ΔC) while limiting the increase of parasitic capacitance (C_p).

This thesis is organized as the following;

The first chapter introduces the concept of energy harvesting, especially, electrostatic/electret vibration energy harvesting. Its working principle and examples are shown. Detrimental effect of C_p on its performance is discussed while the strategies to enhance its output power is reviewed. The objective of this research is stated here.

In the second chapter, nematic liquid crystal is presented as promising anisotropic permittivity fluid for output power enhancement of electret vibration energy harvester. Material characterization method is introduced and its properties are discussed. While the trade-off between enhancement and long-term stability of such generator is considered, the effect of impurity/humidity on LC's resistivity has been examined. Output power generation experiments are conducted to verified the concept of LC-enhanced electrostatic/electret vibration energy harvester.

The third chapter discusses the development of generator model for accurate prediction of LC-enhanced electret vibration generator. The study of molecular alignment of LC molecules inside the generator through the use of Fourier-Transform Infrared spectroscopy and Polarized Optical Microscopy techniques is conducted. The effect of charged and non-charged electret on molecular alignment of LC is examined; especially, LC alignment at interdigital gap. Based on experimental results, a 1-D electrostatic model for output power of LC-enhanced electret vibration

energy harvester is proposed and validated with experiment. Then, performance prediction is made.

The forth chapter presents the impurity control means for LC-enhanced electret vibration energy harvester using ferroelectric materials. The effectiveness of ferroelectricity as impurity control is clarified by comparing with chemisorption effect. Long-term resistivity tests have been performed for metal oxide particles, ferroelectric particles and, ferroelectric thin film. The results are compared and discussed.

The fifth chapter summarizes the results and achievements of this thesis.

Chapter 2

Liquid-Crystal-Enhanced Electret Vibration Energy Harvester

2.1 Chapter Introduction

In this chapter, anisotropic permittivity fluid and its basic characteristics are introduced. To confirm its characteristics, its electrical properties are characterized. The effect of such anisotropic permittivity fluids on electrostatic/electret vibrational energy harvester is examined and discussed; namely, output power enhancement, parasitic capacitance and, surface charge decay of electret.

2.2 Anisotropic Permittivity Materials

Materials with anisotropic properties usually refers to solids with non-cubic crystal structure in single domain, such as tetragonal barium titanate [69]; in a-axis, its permittivity could reaches several thousand while, in c-axis, its permittivity is only a few of hundreds. Apart from single crystals, composite materials also exhibit anisotropic properties. However, solid materials cannot be used as the medium in the dielectric gap of energy harvester due to several reasons; mainly, the possible damages from collision and friction.

Fluids with anisotropic permittivity do not causes the physical damages to the energy harvester. Looking closely, we can categorized them into 2 types; heterogenous mixture and pure anisotropic fluids. Firstly, heterogeneous mixture, as the name implies, is made by mixing anisotropic-shaped particles with isotropic medium. The common examples is ferrofluid [70], which is the mixture of ferrite particles and isotropic medium. Despite its anisotropic properties, it is not commonly available while its resistivity is low (10^8 - $10^{11} \Omega \cdot \text{cm}$); making it unsuitable for the electrostatic/electret energy harvester. On the other hand, pure anisotropic fluids such as liquid crystals exhibits anisotropic properties without the need of additional materials. It also has relatively high resistivity ($>10^{11} \Omega \cdot \text{cm}$). Furthermore, it is commonly available due to display industries. Hence, in the present study, liquid crystals will be used as anisotropic permittivity fluid for electret vibration energy harvester.

2.3 Liquid Crystal as Anisotropic Permittivity Fluid

Discovered in late 19th century, liquid crystal is a state of material that has the physical properties similar to liquid while having a certain degree of molecular order like crystalline solid. It can be said that liquid crystal is an intermediate phase existed between crystalline solid and isotropic liquid as shown in Figure 2.1. Generally, its molecules tend to align to the same direction in this state; that direction is called director. It could be categorized into 4 types depending on the molecular ordering;

- Nematic: its molecules are represented by rod-shaped or ellipsoid. It has the least order among other types of liquid crystal, only the short-range order between the molecules. Due to that, it could move freely and has smaller viscosity compared to other types or phases.
- Smectic: similar to nematic phase plus transitional order, smectic phase maintains short-range order of nematic phase. But, its molecules tend to align themselves in layer or plane. This causes it to have higher viscosity than nematic phase.
- Cholesteric: looking in one layer, cholesteric phase is just like the nematic phase. However, it shows the twisted orientation of director between each layer. This phase can also be called chiral nematic phase.
- Discotic: unlike other phases, its molecules are represented as discs. It aligns themselves by stacking on top of other molecules.

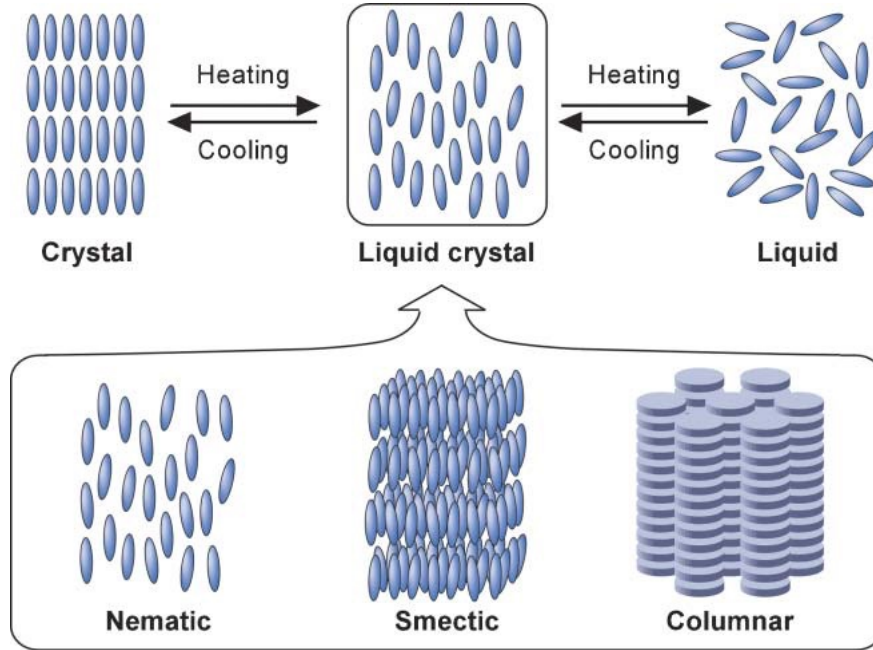


Figure 2.1 Illustration of liquid crystal phases [71].

Liquid crystal exhibits anisotropic properties due to above-mentioned ordering. Depending on which direction is observed, it shows different value of relative permittivity. Generally, it has 2 relative permittivity; axial permittivity, ε_{\parallel} , and transverse permittivity, ε_{\perp} . Axial permittivity represents the permittivity observed along liquid crystal molecule's longitudinal axis. On the other hand, transverse permittivity represents permittivity observed from axis perpendicular to its longitudinal axis. The anisotropic permittivity, $\Delta\varepsilon$, of the liquid crystal can be determined by the following equation:

$$\Delta\varepsilon = \varepsilon_{\parallel} - \varepsilon_{\perp} \quad (2.1)$$

When $\Delta\varepsilon > 0$, the liquid crystal is called positive anisotropic permittivity liquid crystal/fluid. Accordingly, liquid crystal that has $\Delta\varepsilon < 0$ is called negative anisotropic permittivity liquid crystal. Figure 2.2 shows the example of positive and negative anisotropic permittivity liquid crystal.

Furthermore, it should be noted that liquid crystal can align itself according to external influences, such as, magnetic and electrostatic field, due to its internal dipole. It is important to know that positive anisotropic permittivity liquid crystal aligns its longitudinal axis parallel to the direction of external influences. On the other hand, negative anisotropic permittivity liquid crystal aligns its longitudinal axis perpendicular to the direction of the external influences as shown in Figure 2.2a-b. This can be easily explained by the different position and direction of dipole in the molecule. For liquid crystal with $\Delta\varepsilon > 0$, the direction of the dipole usually parallel to its longitudinal axis and vice versa for liquid crystal with $\Delta\varepsilon < 0$. From the discussion about in-plane overlapping area change electrostatic vibrational energy harvester in chapter 1, high anisotropic permittivity liquid crystal is needed as anisotropic permittivity fluid for enhancing its output power by increasing ΔC and without much increase in C_p .

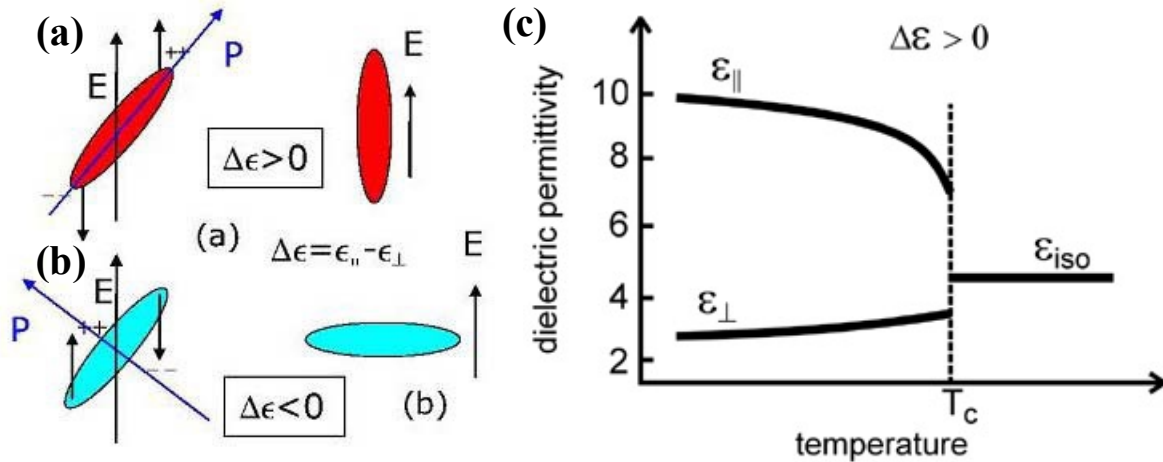


Figure 2.2 Schematic of liquid crystals that have a) positive anisotropic permittivity which has dipole along longitudinal axis and b) negative anisotropic permittivity which has dipole along transverse axis [72] and, c) the example of the positive anisotropic permittivity liquid crystal which has phase transition temperature T_c [73].

Lastly, liquid crystal state is temperature dependent for thermotropic liquid crystal. As shown in Figure 2.2c, the liquid crystal will lose its anisotropic permittivity and becomes isotropic permittivity fluid when the temperature is risen higher than a certain temperature point called phase transition temperature or clearing temperature (T_c or T_{NI}). After all, liquid crystal is a state existed between crystalline solid and isotropic liquid; so, the increase of temperature beyond its phase transition temperature will make it becomes isotropic liquid. In other words, T_{NI} defines the operation range of LC for electret vibration energy harvester.

2.4 Basic Nematic Liquid Crystals

For initial comparison, the commonly known basic nematic liquid crystals with positive anisotropic permittivity are used; 4-cyano-4'-pentylbiphenyl, 5CB, and 3,4,5-Trifluoro-4'-(trans-4-pentylcyclohexyl)-biphenyl, BCH-5F.F.F. Developed by Gray et al. [74], 5CB is a commonly known nematic liquid crystal and widely used for study. 5CB has a dipole located at cyano substituent ($C\equiv N$). Due to the strong dipole from cyano substituent, 5CB exhibits large anisotropic permittivity as shown in Figure 2.3a [75]. In addition, it has nematic phase around room temperature (25°C).

On the other hand, BCH-5F.F.F contains fluoro substituents ($C-F$) as shown in Figure 2.3b. Because of that, it is categorized as fluorinated liquid crystal. Fluorinated liquid crystal is more developed liquid crystal that has decent anisotropic permittivity and resistivity. From the literature review [76, 77], BCH-5F.F.F has nematic range close to room temperature than other fluorinated liquid crystals which is favorable in experimental test.

Last but not least, the overall direction of dipole in 5CB and BCH-5F.F.F is parallel to their molecule's longitudinal axis making them positive anisotropic permittivity nematic liquid crystal and susceptible to aligning themselves parallel with direction of electric field.

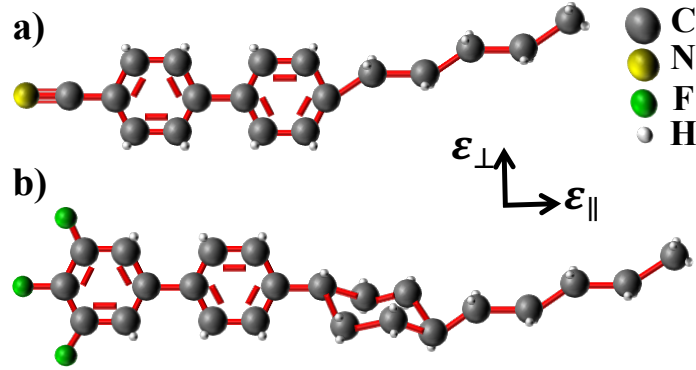


Figure 2.3 Molecular structures of common nematic liquid crystals:
a) 5CB and b) BCH-5F.F.F. The dipole moments are at the short end of aromatic rings.

2.5 Electrical Characterization of Liquid Crystal

This part will present a method used for characterizing electrical properties of liquid crystal. This will include the procedure and modelling. The chosen characterization method is an impedance analyzing. Impedance analyzing is capable of measuring relative permittivity of the material and its resistivity at the same time.

2.5.1 Impedance Analyzing

For impedance analyzing, we use an impedance analyzer system (1260 Impedance/Gain-Phase Analyzer, Solartron Analytical) with the capability of measuring at low frequency range (<1000 Hz) and high accuracy. The schematic of characterization set up is shown as Figure 2.4. The procedure for impedance analyzing is as the following. Liquid crystal is filled into the cell at the isotropic liquid phase. Then, the liquid crystal cell is put into the oven for temperature regulation. The thermocouples attached to the liquid crystal cell are used for monitoring the temperature. Lastly, the liquid crystal cell is connected to the impedance analyzer. The commercial liquid crystal cell with antiparallel alignment (polyimide layer) for positive anisotropic liquid crystal from INSTEC is used as a liquid crystal container for impedance analyzing. Its photo and schematic are shown as Figure 2.5a-b.

From the schematic of liquid crystal cell, it is clearly showing that it is a parallel plate capacitor. This makes the measurement for relative permittivity easy. On the other hand, the resistivity measurement is not as straightforward since the liquid crystal cell can be viewed as multiple capacitor connecting in series. The equivalent electrical circuit model of liquid crystal cell is created using non-ideal capacitor model as a based and is shown as Figure 2.5c.

From Figure 2.5c, R and C represent resistance and capacitance, respectively. The subscript PI represents for polyimide part. while C and R_p indicate capacitance for LC and its internal resistance. R_s represents the series resistance caused by the electrode and wiring which can be in the order of hundreds of ohms. The equation of total impedance Z is as the following:

$$Z = \left[R_s + \frac{2R_{PI}}{1 + (\omega C_{PI} R_{PI})^2} + \frac{R_p}{1 + (\omega C_R R_p)^2} \right] - j \left[\frac{2\omega C_{PI} R_{PI}^2}{1 + (\omega C_{PI} R_{PI})^2} + \frac{\omega C_p R_p^2}{1 + (\omega C_R R_p)^2} \right] \quad (2.2)$$

where ω is the angular frequency from the equation: $\omega = 2\pi f$.

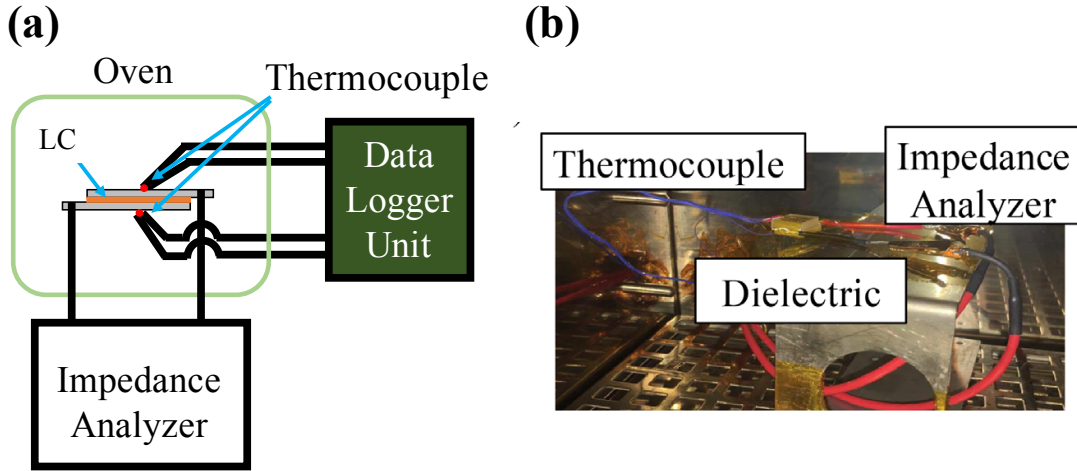


Figure 2.4 Setup of impedance analyzing: a) schematic diagram and b) the photo of the setup.

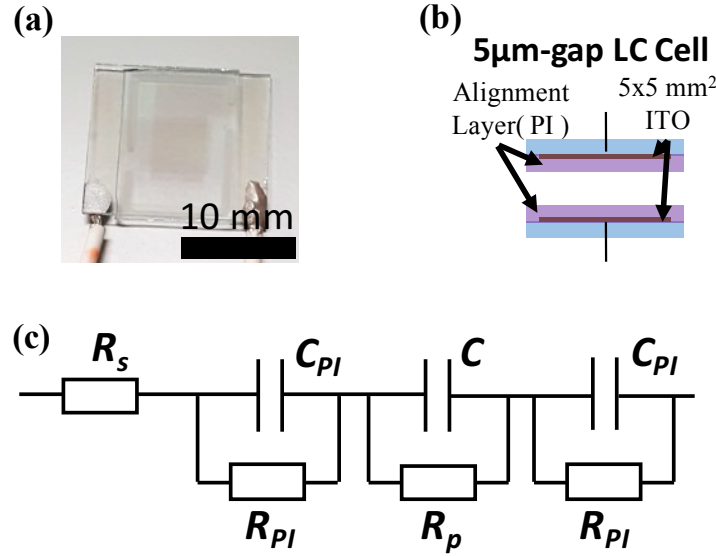


Figure 2.5 Liquid crystal cell from INSTEC; a) its photo, b) its schematic diagram and, c) its equivalent electrical circuit model. The total electrode area is 5mm x 5mm. The gap is 5 μm.

The equation (2.2) can be further explained using a function of physical parameter of the liquid crystal cell and materials by using fundamental equation of resistance and parallel plate capacitance; $R_i = \rho_i \times t_i / A_i$ and $C_i = \epsilon_0 \epsilon_{r,i} \times A_i / t_i$. ρ is the resistivity of material, ϵ_r is the relative permittivity, t is the thickness of material and, A is the liquid-crystal-covered area on the electrode. So, the equation (2.2) becomes the following with the assumption that every parameter except frequency is frequency independent:

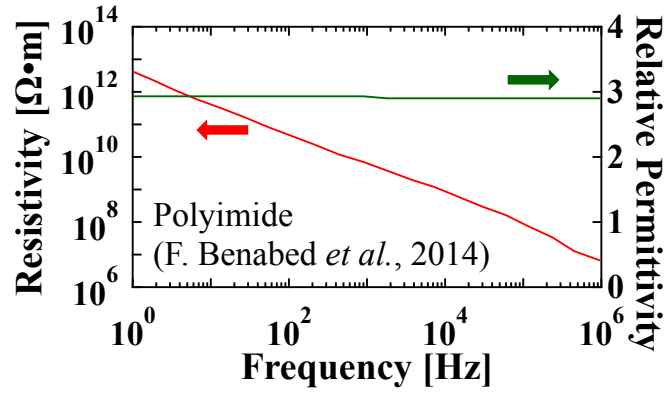


Figure 2.6 Measured resistivity and permittivity of polyimide as a function of frequency [78].

$$Z = \left[R_s + \frac{2(\rho \times t/A)_{PI}}{1 + (\omega \epsilon_0 \epsilon_{PI} \rho_{PI})^2} + \frac{(\rho \times t/A)_{LC}}{1 + (\omega \epsilon_0 \epsilon_{LC} \rho_{LC})^2} \right] - j \left[\frac{2\omega \epsilon_0 \epsilon_{PI} \rho_{PI} (\rho \times t/A)_{PI}}{1 + (\omega \epsilon_0 \epsilon_{PI} \rho_{PI})^2} + \frac{\omega \epsilon_0 \epsilon_{LC} \rho_{LC} (\rho \times t/A)_{LC}}{1 + (\omega \epsilon_0 \epsilon_{LC} \rho_{LC})^2} \right] \quad (2.3)$$

From literature review [78], we had found that resistivity of polyimide is frequency dependent as shown in Figure 2.6. The curve fitting shows the general equation of polyimide's resistivity as a function of frequency to be;

$$\rho_{PI}(f) = a10^{b \log(f)} \quad (2.4)$$

with a and b as arbitrary coefficient and constant. Thus, the total impedance equation will become:

$$Z = \left[R_s + \frac{2(a10^{b \log(f)} \times t/A)_{PI}}{1 + (\omega \epsilon_0 \epsilon_{PI} a10^{b \log(f)})^2} + \frac{(\rho \times t/A)_{LC}}{1 + (\omega \epsilon_0 \epsilon_{LC} \rho_{LC})^2} \right] - j \left[\frac{2\omega \epsilon_0 \epsilon_{PI} a10^{b \log(f)} (a10^{b \log(f)} \times t/A)_{PI}}{1 + (\omega \epsilon_0 \epsilon_{PI} a10^{b \log(f)})^2} + \frac{\omega \epsilon_0 \epsilon_{LC} \rho_{LC} (\rho \times t/A)_{LC}}{1 + (\omega \epsilon_0 \epsilon_{LC} \rho_{LC})^2} \right] \quad (2.5)$$

From the equation (2.5), it shows that the resistance or resistivity of liquid crystal layer is significant only in real part of the total impedance equation. In other word, we can extract said information from the experiment using curve fitting method; on the assumption that the resistivity of liquid crystal is frequency independent. The physical parameters of the liquid crystal cell are shown in Table 2.1.

Table 2.1 Physical parameters of INSTEC's liquid crystal cell.

Parameters		
Electrode area	25	mm ²
Gap	5	μm
Thickness of polyimide	60	nm

2.6 Characterization results

2.6.1 Relative Permittivity and Threshold voltage

Firstly, 5CB is tested with impedance analyzer using liquid crystal cell with parallel horizontal alignment layer. Figure 2.7 shows the permittivity change of 5CB as a function of electric field strength. With the change of permittivity from 6 to 18 as the electric field increases, it represents the change of transverse to axial permittivity in the sensing direction (the direction of liquid crystal thickness). By using 95% of the total permittivity change, we conclude the threshold electric field strength for 5CB to be $1 \text{ V}/\mu\text{m}$ and its anisotropic permittivity to be 12.

In the same manner, the BCH-5F.F.F is tested. With the observed change of permittivity from 4 to 12 as a function of electric field strength, we conclude its threshold electric field strength to be $1.5 \text{ V}/\mu\text{m}$ and its anisotropic permittivity to be 9 as shown. It should be noted that all the measurement is performed at 1000-Hz frequency of applied electric field.

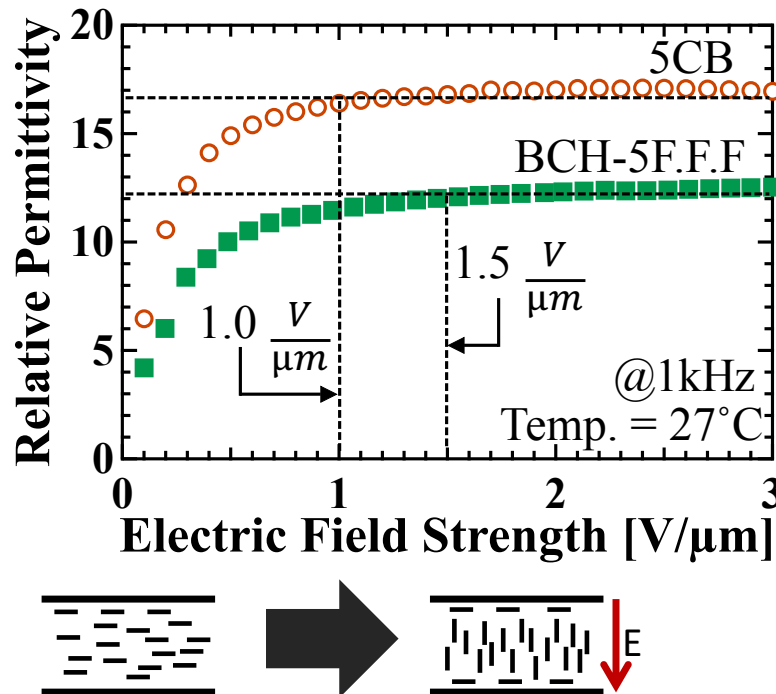


Figure 2.7 Change in relative permittivity as a function of electric field strength.

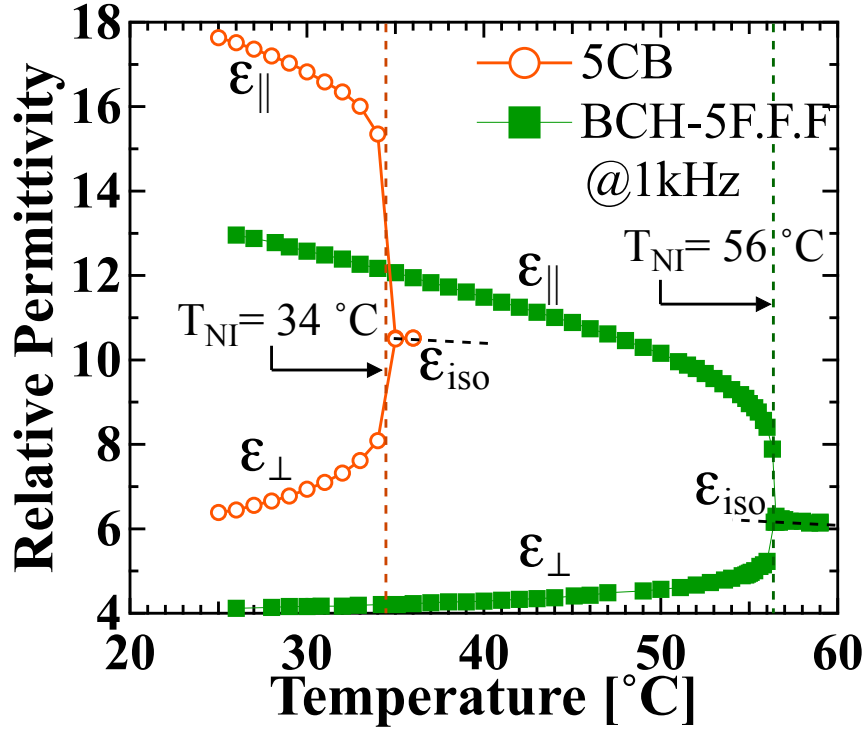


Figure 2.8 Measured anisotropic permittivity of basic nematic liquid crystals.

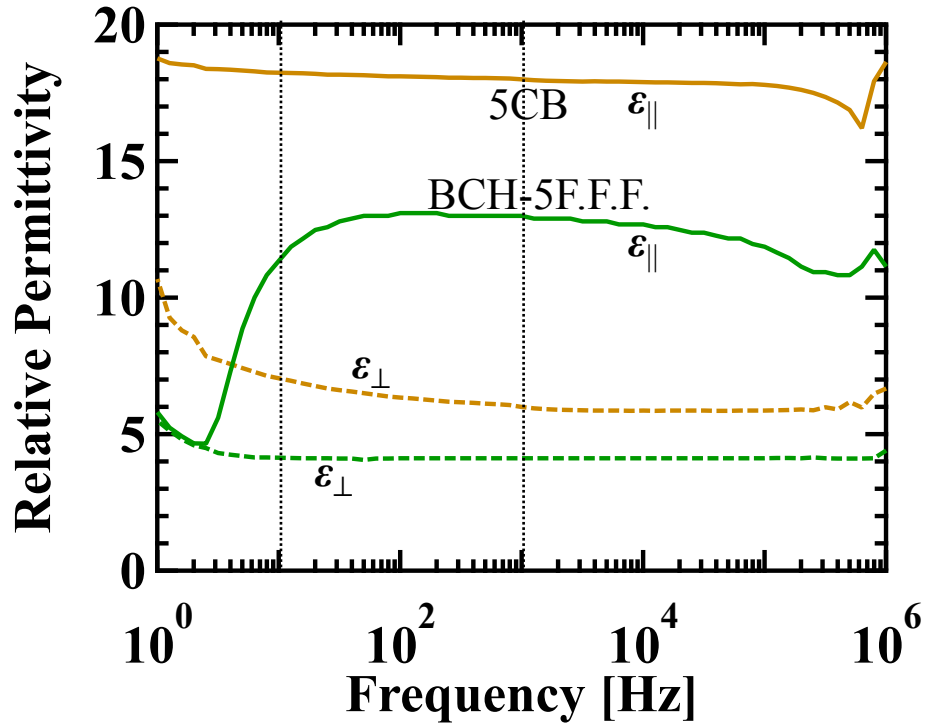


Figure 2.9 Frequency dependency of LCs' relative permittivities. Black dot lines indicate 1000 and 10 Hz frequency.

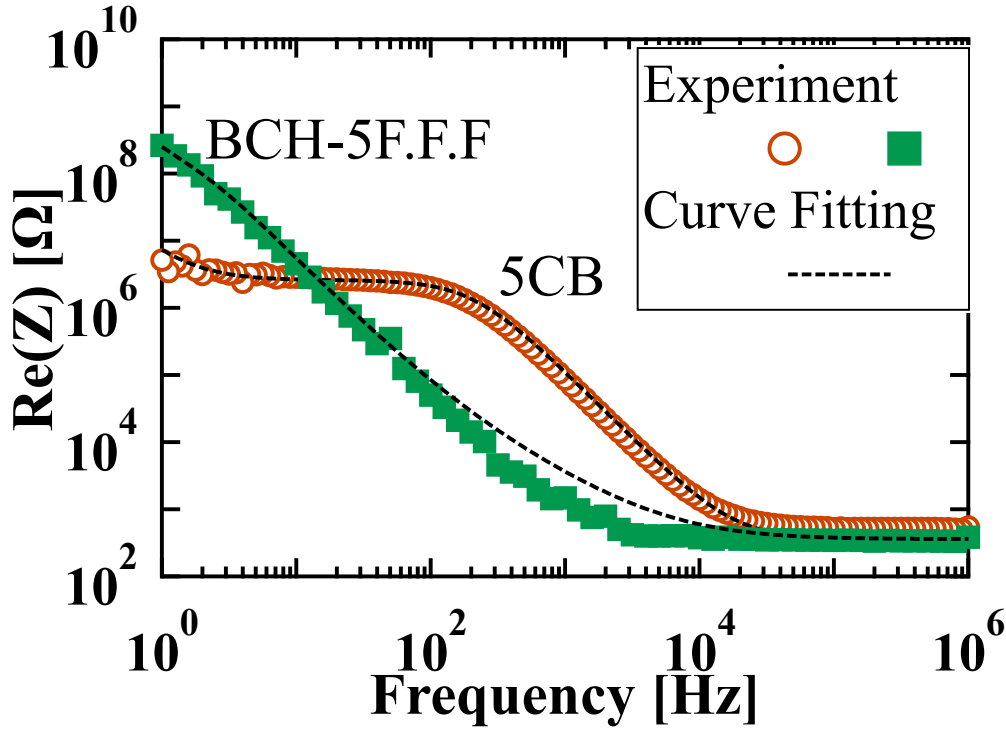


Figure 2.10 Real part of the measured total impedance of liquid crystal cell with the curve fitting from eq. (2.5).

Figure 2.8 shows the comparison between relative permittivity of 5CB and BCH-5F.F.F as a function of temperature. The transverse permittivity is measured with 0.5 V_{AC} while the axial permittivity is measured with 10 V_{AC} (2 V/μm) to ensure the thorough change of the LC molecule alignment. It shows that 5CB has both axial and transverse permittivity larger than that of BCH-5F.F.F. The transition temperature is shown as the permittivity becomes isotropic at about 34°C. For BCH-5F.F.F, its transition temperature is about 56 °C; indicating 3-times wider operation range for BCH-5F.F.F.

Since the usual operating frequency of our electret vibration energy harvester is much below 1000 Hz, frequency dependency of relative permittivity of LC is measured as shown in Figure 2.9. It is found that relative permittivities of LCs are quite constant at the frequency above 10 Hz while relative permittivities at frequency below 10 Hz may depend on each LC molecules/species as shown in the large increase and decrease in transverse permittivity of 5CB and axial permittivity of BCH-5F.F.F, respectively. Hence, the subsequent output power generation experiments will be performed at 10-Hz vibration frequency.

2.6.2 Resistivity of 5CB and BCH-5F.F.F

The total impedance of each liquid crystal as a function of frequency and its phase degree are shown is measured. Then, the real part of total impedance is shown in Figure 2.10. The curve fitting (dash line) from the real part of the equation (2.5) shows the agreement with measured values of impedance for both 5CB and BCH-5F.F.F. From curve fitting, the resistivity of 5CB and BCH-5F.F.F are 1.3×10^9 and $7.4 \times 10^{11} \Omega \cdot \text{cm}$, respectively.

This could be explained by the difference of cyano and fluoro substituents [76] [77] [79] [80]. From literature reviews [79] [80], 5CB is commonly known about its high polarizability and ionic impurities; in other word, low resistivity. Compared to $C\equiv N$, $C-F$ shows low polarizability which means smaller amount of impurities and higher resistivity [76] [77].

Hence, this shows that 5CB may not be a good candidate for enhancement of electrostatic vibrational energy harvester because of its low resistivity. Large leakage current may occur which could negate/discharge the high surface potential at charged electret. On the other hand, BCH-5F.F.F shows more than 240 times of resistivity higher than 5CB which is a promising candidate for using in direct-contact with high bias voltage or charged electret.

2.7 Output Power Generation Experiments with Electrostatic Vibration Energy Harvester

2.7.1 1-D Electrostatic Model of Electrostatic Vibration Energy Harvester

As stated before, this thesis focuses on in-plane overlapping area change electrostatic vibration generator. Similar to Tada [81] and Tsutsumino et al. [82], we can create 1-dimension (1-D) electrostatic model of the output voltage by looking at the generator in electrical point of view. Its schematic is shown as Figure 2.11. One of top electrode is connected to voltage source, imitating high surface potential V_{surf} of charged electret, while the another one is connected to ground. The bottom electrode is connected to external load resistance R , while also, in parallel with parasitic capacitance C_p . Top and bottom electrodes is separated by dielectric material with dielectric constant of ϵ_1 and thickness g . There is electric field E_1 from source-connected top electrode to bottom electrode; similarly, there is also electric field E_2 from ground-connected top electrode to bottom electrode. It should be noted that we can neglect guard electrode on bottom side since its potential is always be zero.

Firstly, we could get the governing equations by applying Kirchhoff's voltage law. From each top electrode to same bottom electrode. They will be as the following:

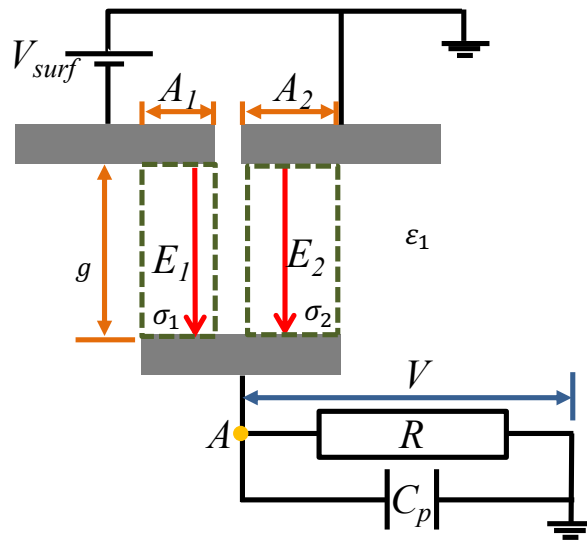


Figure 2.11 1-D electrostatic model of electrostatic vibration energy harvester.

$$V_{surf} + gE_1 + V = 0 \quad (2.6)$$

$$gE_2 + V = 0 \quad (2.7)$$

From the above equations, we can derive the electric field E_1 and E_2 like this;

$$E_1 = -\frac{V_{surf} + V}{g} \quad (2.8)$$

$$E_2 = -\frac{V}{g} \quad (2.9)$$

Next, we apply the Gaussian's surface theory onto the bottom electrode as shown in eq. (2.10). It shows the relationship between induced charge and electric field. In other word, this could tell us the information about the induced charge Q caused by top electrodes. By substitute eq. (2.8) and (2.9) into (2.10), we could get eq. (2.11).

$$\sigma_i = -\epsilon_0 \epsilon_i E_i \quad (2.10)$$

$$\sigma_1 = \epsilon_0 \epsilon_1 \frac{V_{surface} + V}{g} \text{ and } \sigma_2 = \epsilon_0 \epsilon_2 \frac{V}{g} \quad (2.11)$$

Then, we use Kirchhoff's current law at node A to get eq. (2.12). This is the important equation since it includes all the terms concerned for output voltage. A_1 is the overlapping area under electric field E_1 while A_2 is the overlapping area under electric field E_2 . The same for induced charges σ_i .

$$\frac{d}{dt}(\sigma_1 A_1 + \sigma_2 A_2) + \frac{V}{R} + C_p \frac{dV}{dt} = 0 \quad (2.12)$$

Next, we substitute eq. (2.11) into eq. (2.12) to get:

$$\frac{dV}{dt} = -\frac{\frac{V}{R} + BV_{surface} \frac{dA_1}{dt}}{BA_{max} + C_p} \quad (2.13)$$

where $B = \epsilon_0 \epsilon_1 / g$.

Lastly, we get the equation (2.14) represented the change of output voltage over time. And by solving this equation numerically, we could get the output voltage of the generator. The method Range-Kutta of the 4th-order is employed to solve this differential equation. The average output power could be known from the following the equation;

$$P = \frac{V^2}{R} \text{ or } P_{avg} = \frac{1}{T} \int_0^T \frac{V^2}{R} dt \quad (2.14)$$

While V is a function of time.

From equation 2.14, we can see that the rate of change of output voltage, excluding the external load resistance, depends on the bias voltage and rate of change in overlapping area. In addition, similar to the output power model of rotational electret energy harvester discussed in chapter 1.4, output voltage of in-plane electrostatic vibration generator, also affects by the influence of parasitic capacitance; which in turn, undesirably affects the output power.

2.7.2 Fabrication of Electrostatic Vibration Energy Harvester

The test devices are fabricated using standard MEMS fabrication technologies. The brief fabrication process is as the following. Firstly, the TEMPAX glass substrate is cleaned to remove organic waste and dust. Secondly, Cr/Au/Cr electrode is sputtered onto the substrate. The chromium is sputtered onto the substrate first to be an adhesion promoting layer for gold. The total thickness of metal electrode is 300 nm. Thirdly, it is coated with positive photoresist (PR) and photolithography techniques are performed on PR-coated metal-sputtered TEMPAX substrate. Next, the metal electrode is etched using corresponding metal etchants; creating the patterned of interdigitated electrode on substrate. Then, the photoresist is removed with its remover solution. Next, samples are separated by dicing saw. The electrodes are then coated with 100nm-thick Al_2O_3 insulation layer.

The schematic of fabrication process is shown as Figure 2.12. The detailed procedure and its condition are shown in appendix A. Figure 2.13 shows the fabricated interdigital electrode plate. The physical parameter of interdigital electrode or substrate with interdigital electrode is shown as Table 2.2. The pair of fabricated electrodes is used in power generation experiment as top and bottom electrodes.

Table 2.2 Physical parameters of fabricated electrostatic vibration energy harvester.

Parameters		
Electrode area	20×20	mm ²
Pitch	1.0	mm
Electrode width	0.45	mm
Interdigital gap	0.05	mm

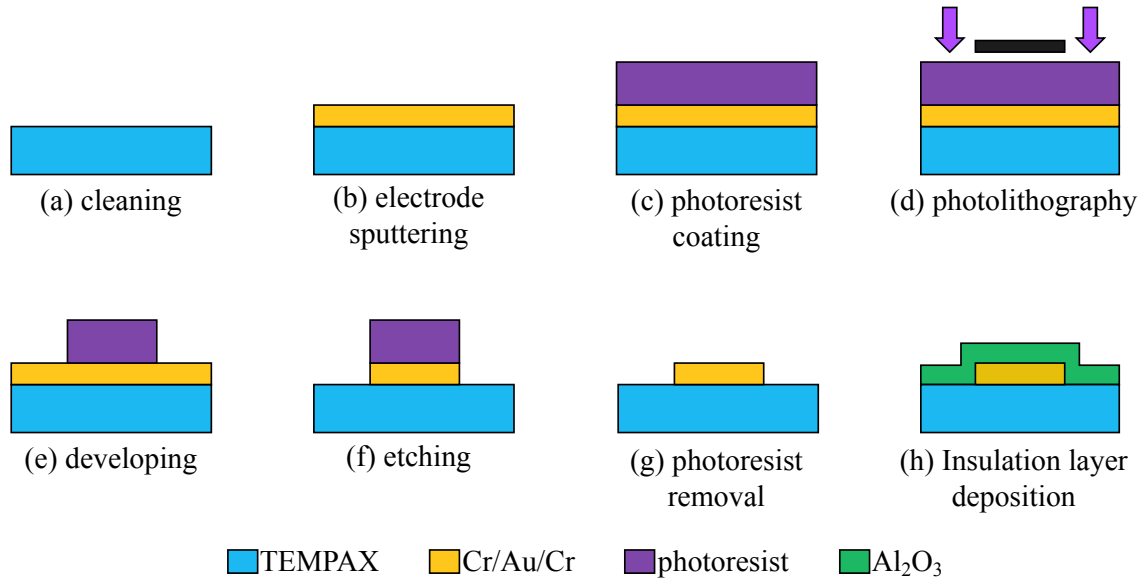


Figure 2.12 Schematic of fabrication flow for the electrostatic vibration energy harvester.

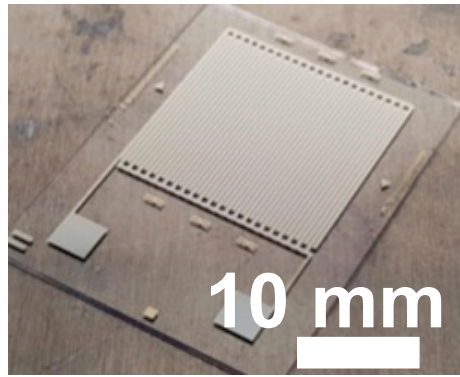


Figure 2.13 Photo of fabricated electrode for electrostatic vibration energy harvester

2.7.3 Experimental Setup

The schematic of our experimental set up for power generation experiment is shown as Figure 2.14. The substrate with interdigitated electrode is mounted onto the bottom stage which attached to the precision guide rail. The precision guide rail (VRU1085, THK, 3- μ m tolerance) is connected to the electromagnetic shaker (APS-113, APS Dynamics, Inc.) through the hinge connection; this ensures the movement generated by electromagnetic shaker will be in 1-dimension. The electromagnetic shaker is powered by function generator (AFG 3022, Tektronix Inc.) to provide 1-dimension harmonic vibration to the bottom substrate. The vibration amplitude is adjustable by changing the voltage output at function generator and gain at voltage amplifier. The vibration amplitude is monitored by gap measuring laser meter (LC-2440, KEYENCE™). The top substrate is mounted onto 5-axis stage. The top and bottom substrates are set in parallel with the aid gap measuring laser meter and digital camera (LT-9500, KEYENCE™) with high precision of 0.01 μ m. Source Measure Unit (2410 SourceMeter® SMU, Keithley™) is used to act as the external voltage source, imitating charged electret. It is connected to the top substrate. The bottom substrate is connected to the external circuit. It is consisting of external load R and programmable I/V converter-amplifier (CA 5350, NF).

The data logger unit (NR-600, Keyence) is connected in series with I/V converter-amplifier. The use of I/V converter-amplifier is very helpful since the large output voltage from electrostatic energy harvester is commonly known to be difficult to capture directly without the use of voltage divider scheme. It should be noted that the information capture through data logger unit is the output current I , not output voltage V , though it is correlated ($V = IR$). Figure 2.15 shows the photo of experimental setup and the zoom-up photo of top stage with mounted substrate. The experimental condition is as shown in Table 2.3.

Table 2.3 Experimental conditions for output power generation experiment.

Parameters	
Dielectric gap	100 μm
Vibration amplitude	1.0 $\text{mm}_{\text{peak-leak}}$
Vibration frequency	10 Hz
Applied bias voltage	-500 V
I/V gain	10^6 V/A

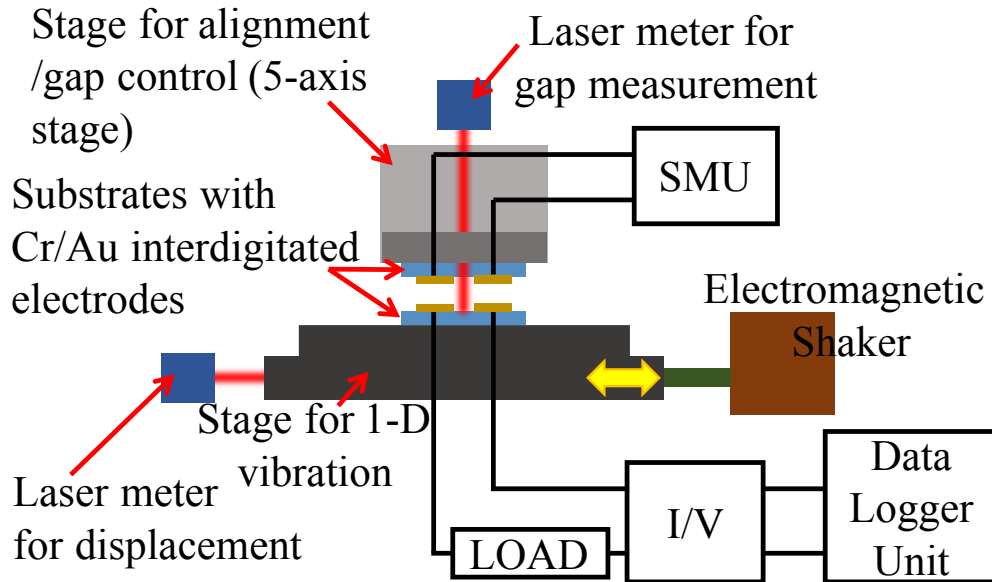


Figure 2.14 Schematic of power generation experimental setup.

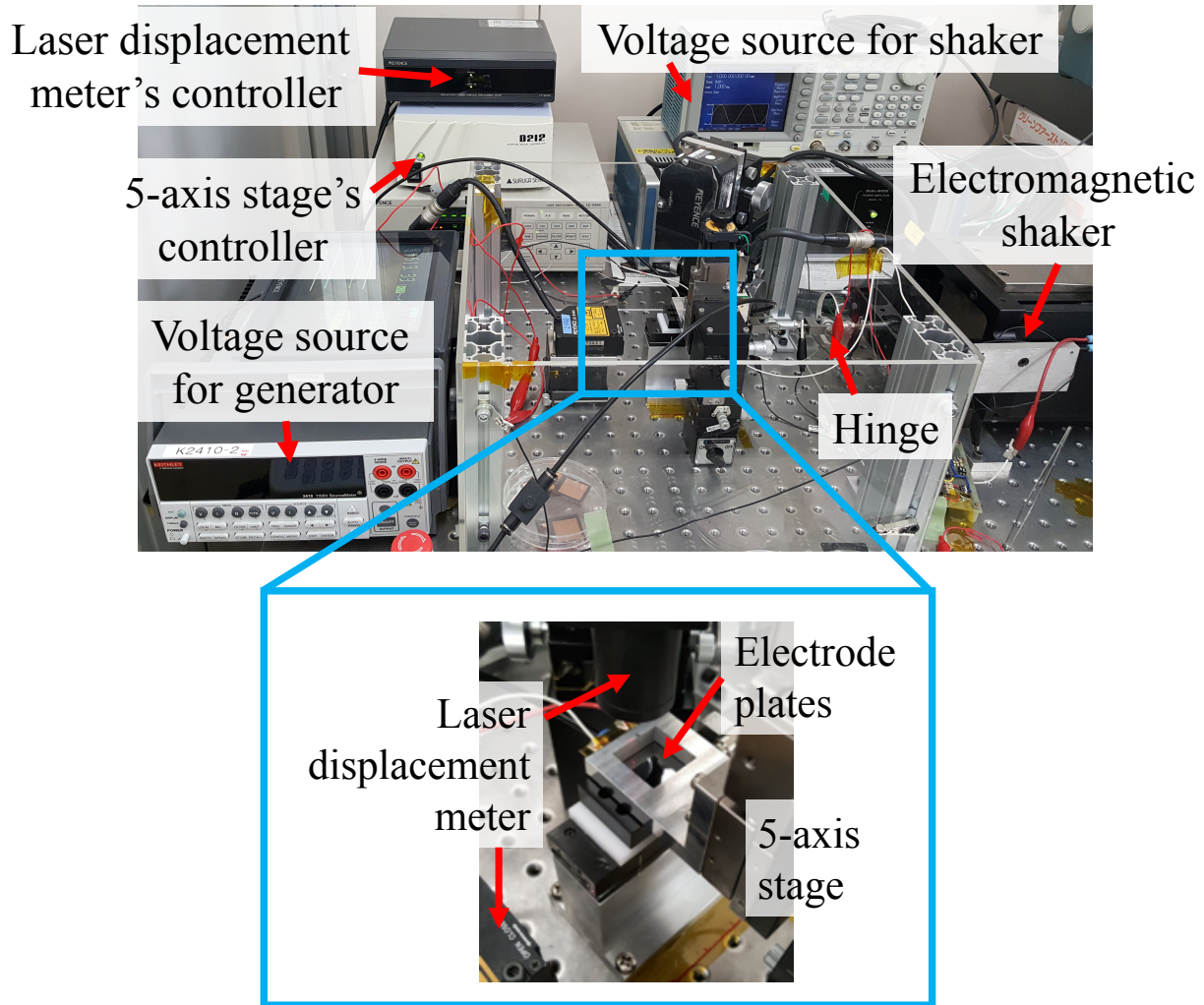


Figure 2.15 Photo of experimental setup.

2.7.4 Output Power Generation Results

Basic nematic LCs, 5CB and BCH-F.F.F, has been tested for output power generation with electrostatic vibration energy harvester. For the comparison, FC-3283 (3M™) has been used as isotropic permittivity fluid with relative permittivity of 1.91 and bulk resistivity of $10^{15} \Omega \cdot \text{cm}$. Figure 2.16 shows the output voltage waveform of different permittivity fluids at their corresponding optimal resistance. For isotropic permittivity fluids, peak-to-peak voltages of air and FC-3283 are 70 and 88 V, respectively. On the other hand, 5CB ($\Delta\epsilon=12$) and BCH-5F.F.F ($\Delta\epsilon=9$) has respective peak-to-peak voltage of 250 and 260 V. Figure 2.17 shows the output power versus external load resistance. With isotropic fluid such as FC-3283, the maximum output power is $13.3 \mu\text{W}$. On the hand, with nematic liquid crystals 5CB and BCH-5F.F.F, the maximum output power is as high as $443 \mu\text{W}$ and $336 \mu\text{W}$, respectively. Compared to conventional air gap, LC-in-the-gap can obtain the output power enhancement of two-order-of-magnitude while isotropic-permittivity-in-the-gap could only improve the output power by 2.6 times. Based on the results, the output power can be enhanced larger with higher anisotropic permittivity as shown in Table 2.4.

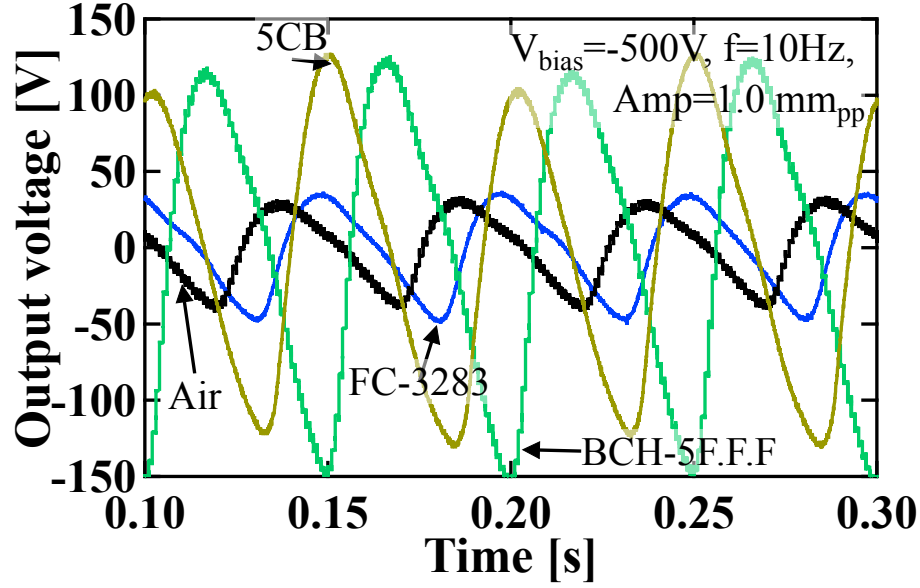


Figure 2.16 Output voltage waveform of different permittivity fluids at its corresponding optimal load resistance..

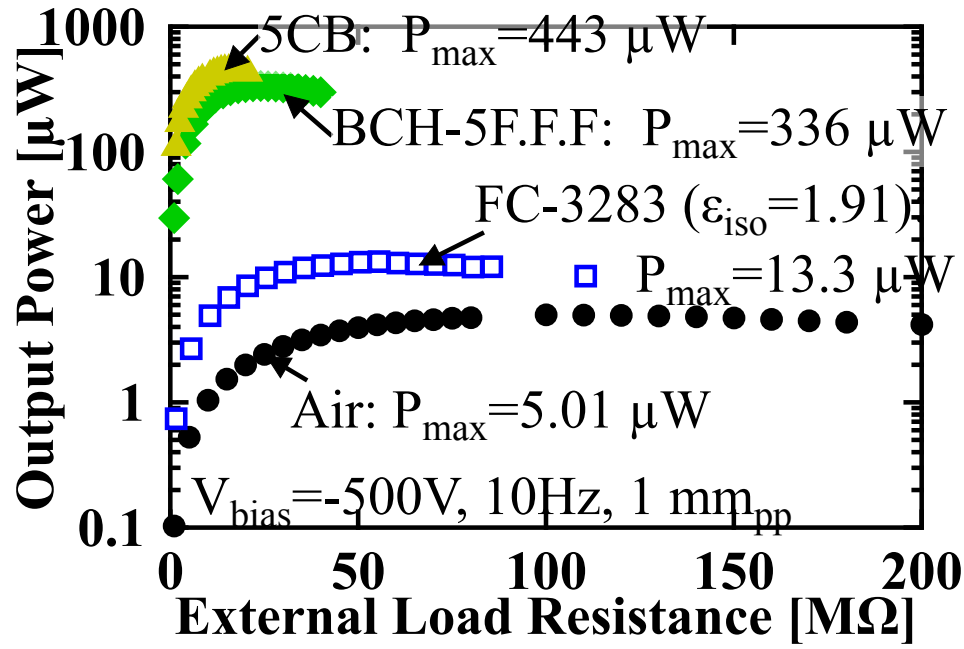


Figure 2.17 Output power versus external load resistance of electrostatic vibration energy harvester with air, FC-3283, 5CB and, BCH-5F.F.F as dielectric medium.

Table 2.4 Enhancement and anisotropic permittivity.

LC	Anisotropic permittivity $\Delta\epsilon$	$P_{max,LC}/P_{max,air}$
5CB	12	87
BCH-5F.F.F	9	67

Table 2.5 Comparison between measured and simulated C_p of different permittivity fluids.

Permittivity fluid	$C_{p,mea.}$ [pF]	$C_{p,sim.}$ [pF]
Air	60	57
FC-3283	70	66
5CB	150	224 ($\epsilon_{ }=18$) 145 ($\epsilon_{iso}=10$) 106 ($\epsilon_{\perp}=6$)
BCH-5F.F.F	107	185 ($\epsilon_{ }=12$) 106 ($\epsilon_{iso}=6$) 87 ($\epsilon_{\perp}=4$)

Furthermore, C_p of the generator has been measured using impedance analyzer. It is founded that measured C_p is slightly larger than that of correlation model [64] with ϵ_{\perp} in LC as shown in Table 2.5. By using correlation equation, it is discovered that horizontal permittivity at interdigital gap is similar to the isotropic permittivity of LC; $\epsilon_{iso}=(\epsilon_{||}+2\epsilon_{\perp})/3$.

Despite the enormous enhancement, the leakage currents from 5CB and BCH-5F.F.F are founded to be quite large due to its low resistivity ($>1\text{mA}$ for 5CB and $>1\mu\text{A}$ for BCH-5F.F.F). This could lead to the discharge of electret in the actual electret generator. In the preliminary test with electret generator, it is confirmed that discharge happens rapidly; resulted in insignificant output power. In the next part, the resistivity characteristic of LC is discussed.

2.8 Surface Charge Decay of Electret and Trade-off from Liquid Crystal

It is widely known that electret materials will discharge upon the contact of liquid. Wang et al. [83] confirmed that CYTOP has poor charge stability in high humidity environment while Wu et al. [84] demonstrated its stability with low permittivity fluid, such as, hexadecane ($10^6 \Omega\cdot\text{cm}$) as shown in Figure 2.18. This could be one of the reasons for lower-than-expected output power in [65] [68] [66] [67] due to the use of high-permittivity-but-low-resistivity fluid with electret vibration generator .

On the other hand, large anisotropic permittivity is desirable to achieve high output power enhancement as shown in Figure 1.23 (in chapter 1) and Table 2.4. However, there is a trade-off characteristic between LC resistivity and its anisotropic permittivity as shown in Figure 2.19. In other words, high output power enhancement from large anisotropic permittivity may not be sustainable due to its correspondingly low resistivity. Thus, the LC used for electret vibration energy harvester should have a balance between high resistivity and moderately high anisotropic permittivity. Based on Figure 2.19, the suitable anisotropic permittivity should be lower than 5.

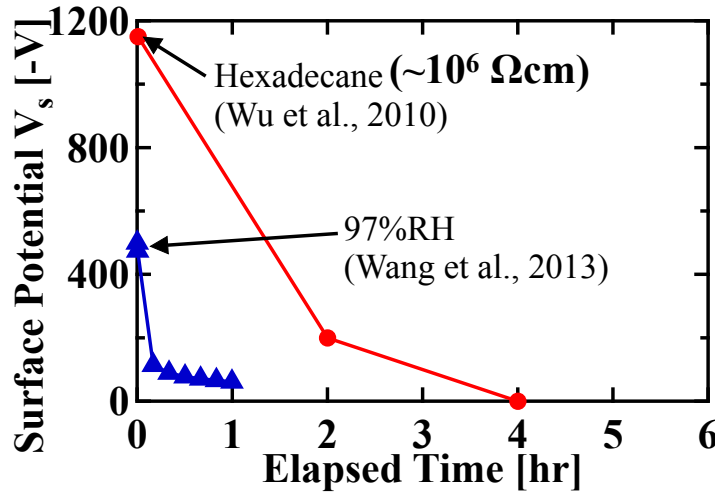


Figure 2.18 Surface potential decay under the contact of low resistivity fluids.

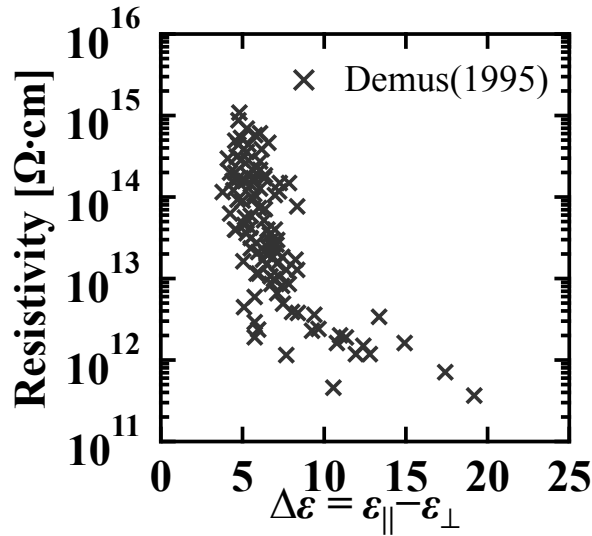


Figure 2.19 Inverse proportional relation between resistivity and anisotropic permittivity characteristics of LC. [85]

2.9 High-Resistivity Nematic Liquid Crystal

According to discussion in 2.8, we choose high-resistivity nematic liquid crystal called MLCL-7030 (MERCK) for investigation. Its bulk resistivity is higher than $10^{16} \Omega\cdot\text{cm}$ while it has anisotropic permittivity of about 3. Figure 2.20a shows the comparison of axial and transverse permittivity between BCH-5F.F.F. and MLC-7030. MLC-7030 has axial and transverse permittivity of 6.02 and 2.8, respectively. Although its axial permittivity is lower than that of BCH-5F.F.F., its transverse permittivity is also lower which leads to smaller ϵ_{iso} , consequently smaller C_p . Furthermore, it has wider nematic range making it to be more applicable for large operational temperature range. Its threshold electric field strength is found to be $3 \text{ V}/\mu\text{m}$ as shown in Figure 2.20b. Additionally, relative permittivities of MLC-7030 has shown to be frequency independent as shown in Figure 2.20c.

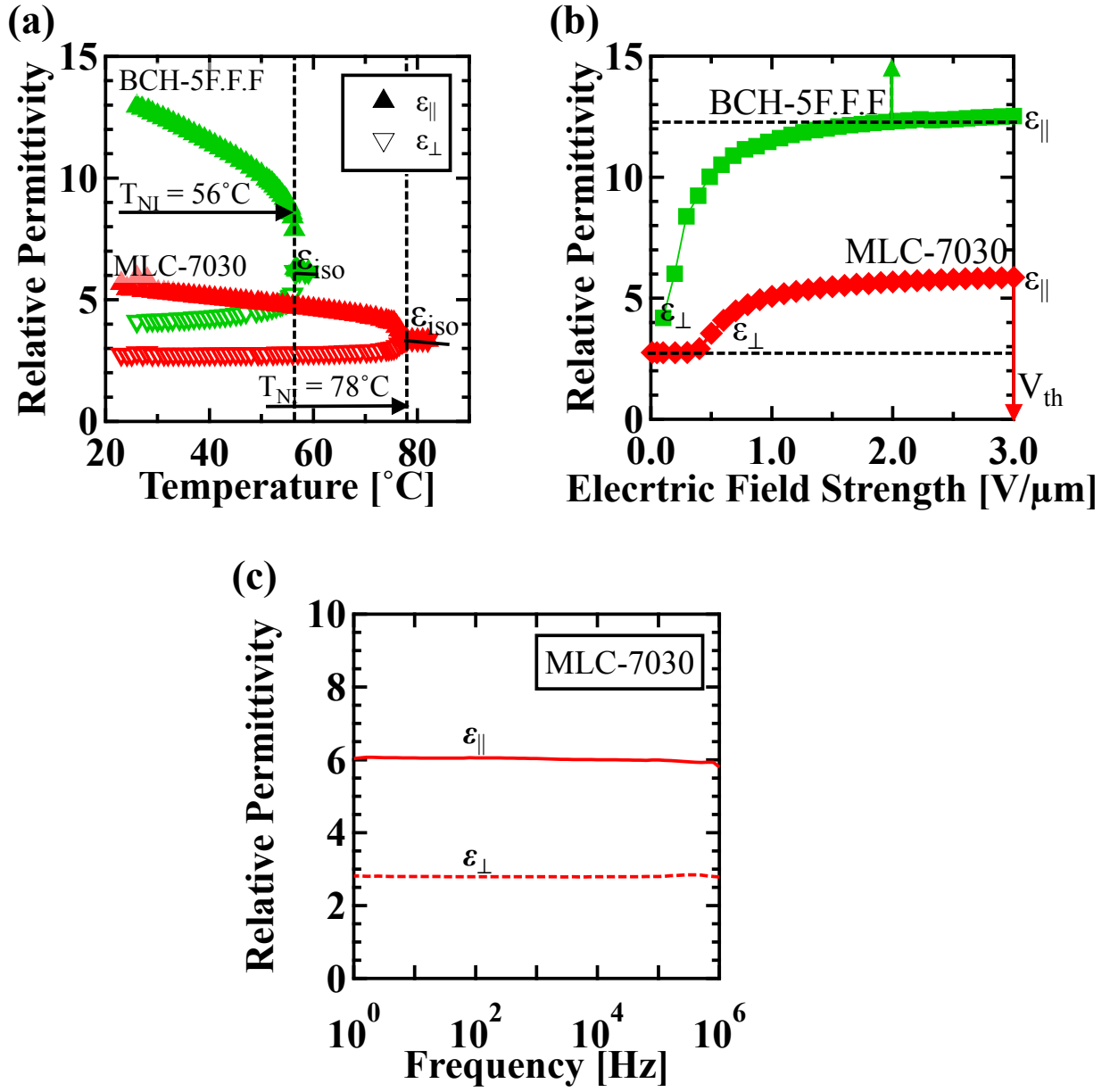


Figure 2.20 (a) Relative permittivity of MLC-7030 compared to BCH-5F.F.F. and (b) frequency dependency of MLC-7030's relative permittivities.

2.10 Effects of Impurity and Humidity on Liquid Crystal

2.10.1 Effect of Impurity and Humidity on Resistivity of LC

From Figure 2.19, we know that the resistivity of LC as a function of its anisotropic permittivity. It is noted that measured resistivity of MLC-7030 is much lower than that of in datasheet. According to Gauza et al. [86] and Hung et al. [87], the humidity absorption and ionic contamination are the common reasons for low resistivity of the LC. To verify this, commercial LC cell is cleaned with isopropanol (IPA) in ultrasonic bath for 5 minutes. Then, it is dried in vacuum oven (VOS-201SD, EYELS). After LC is filled into LC cell, the inlet holes are sealed with low impurity UV-curing epoxy (3026E, Threebond) to isolate LC from outside atmosphere.

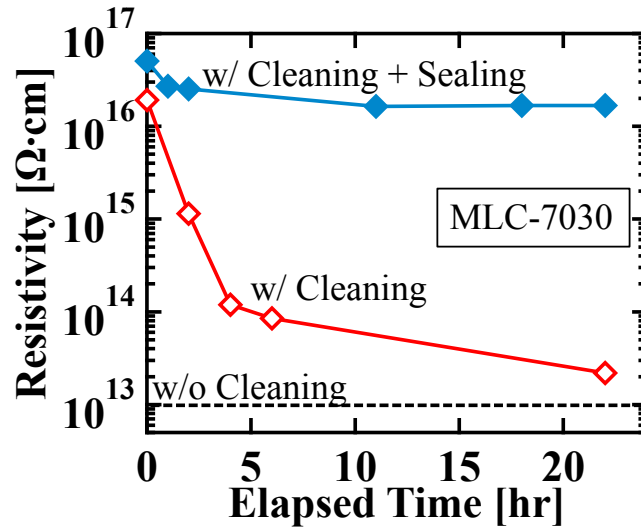


Figure 2.21 Resistivity over elapsed time of MLC-7030 with different conditions of impurity/humidity control.

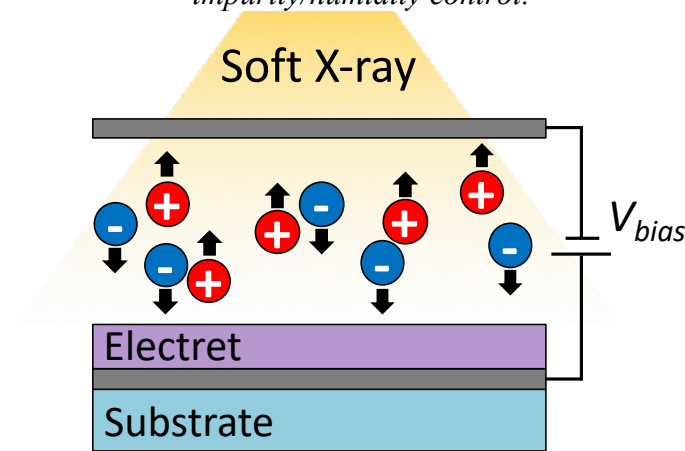


Figure 2.22 Schematic of Soft-X-ray charging technique.

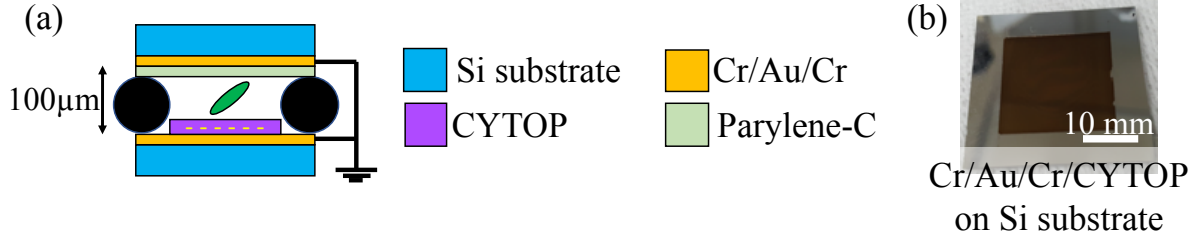


Figure 2.23 (a) Schematic of surface charge decay experiment and (b) photo of electrode for the experiment with 15μm-thick electret. Green ellipsoid represents LC in the gap.

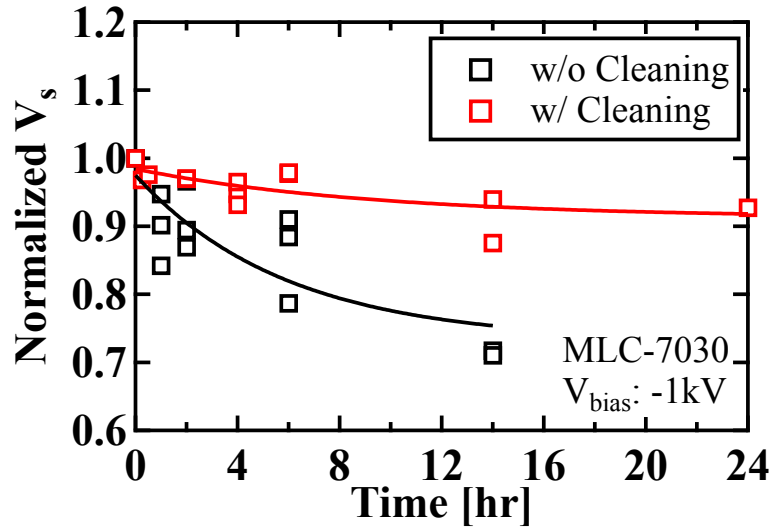


Figure 2.24 Normalized surface potential overtime of charged electret under direct contact with MLC-7030 in uncleaned and cleaned states. Initial surface potential is about -1kV.

Figure 2.21 shows the resistivity versus the elapsed time of LC cell with 3 different conditions; 1) uncleaned, 2) cleaned but not sealed and, 3) cleaned and sealed. With adequate impurity/humidity control, such as condition (3) cleaning and sealing the LC cell, high resistivity of MLC-7030 of $10^{16} \Omega \cdot \text{cm}$ can be realized. On the other hand, with only cleaning, high resistivity of MLC-7030 is initially realized but deteriorate over time. Lastly, the uncleaned LC cell cannot realize high resistivity of LC.

2.10.2 Effect of Impurity/Humidity Control on Surface Charge Decay of Electret with LC

Initial test on surface charge decay with LC is conducted. 15μm-thick CYTOP-EGG is spin-coated on Cu plate and charged to $-1kV_{bias}$ with soft x-ray charging technique [88] as shown in Figure 2.22. Air is ionized by soft x-ray; then, it is induced to electret surface with applied electric field from V_{bias} . MLC-7030 is sandwiched between charged electret and bare Cu-plate with 100μm gap as shown in Figure 2.23. With cleaned cell, the surface charge shows slow deterioration while the discharge happens at faster rate with uncleaned cell as shown in Figure 2.24. This proves that high resistivity of LC is necessary to keep high surface potential of electret; with the minimum resistivity of $10^{16} \Omega \cdot \text{cm}$.

2.10.3 Output Power Generation Experiment of Electret Vibration Energy Harvester with Impurity/Humidity Control

2.10.3.1 Experimental Setup

The setup for output power generation experiment with impurity/humidity control and its experimental conditions are similar to that of chapter 2.7.3 but, without external voltage source. Instead, the top electrode (electret electrode) is spin coated with 15 μ m-thick CYTOP-EGG. For observing the effect of impurity/humidity control, both charge-collector and electret electrodes are cleaned with IPA in ultrasonic bath like the process in chapter 2.10. Then, electret electrode is charged to -1kV with soft x-ray charging technique. To imitate the effect of low humidity, the acrylic walls and plastic lid is used to isolated the generator from external environment. N₂ is introduced into the setup keeping the relative humidity low (<10%RH). Figure 2.25 shows the modified setup and Figure 2.26 shows the relative humidity inside the setup after lid is sealed and N₂ is introduced. MLC-7030 is filled into the dielectric gap in low humidity condition, after the N₂ has been introduced for 20 hours to prevent the water reabsorption into LC.

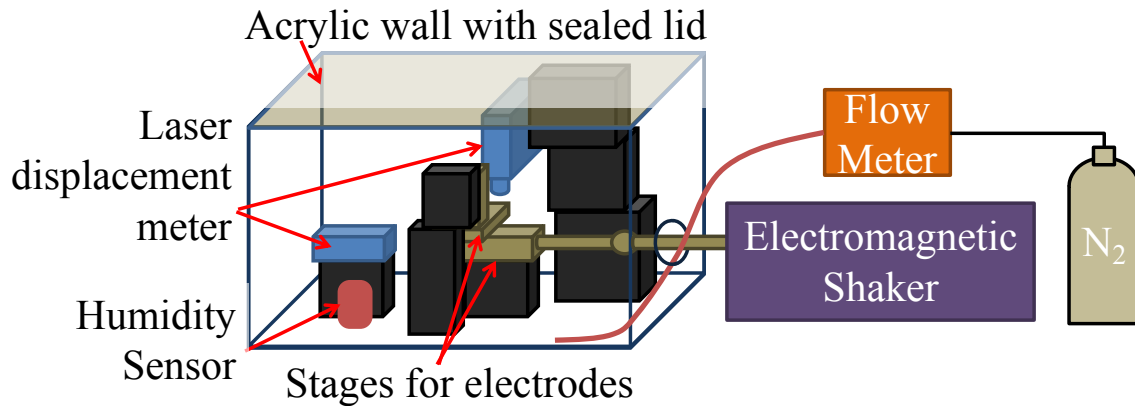


Figure 2.25 Experimental setup with impurity/humidity control for LC-enhanced electret vibration energy harvester

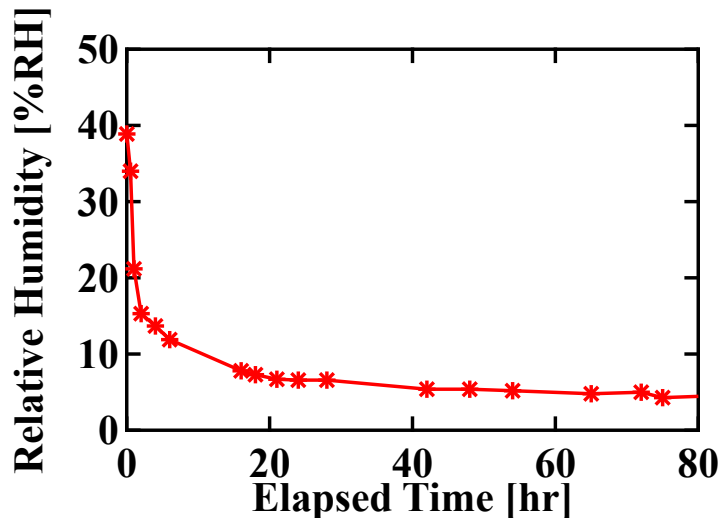


Figure 2.26 Relative humidity inside sealed experimental setup overtime after introducing N₂ gas.

2.10.3.2 Output Power Generation

Figure 2.27 shows the output voltage waveform of conventional air-in-the-gap and MLC-7030 at corresponding optimal resistance. The peak-to-peak voltage of LC-filled-gap is about 300 V while that of air gap is 140 V. Measured C_p with MLC-7030-in-the-gap is about 80pF; using correlation equation (eq. 1.12), the interdigital gap's permittivity is corresponding to $\epsilon_{iso} = 3.0$. Figure 2.28 shows the output power versus external load resistance at 0th hour. With MLC-7030, its maximum output power is 139 μ W at 68M Ω while it is about 20 μ W at 100 M Ω for conventional air-in-the-gap one. The output power enhancement is 7 times compared to air gap. Figure 2.29 shows the normalized output power versus elapsed time. With adequate impurity/humidity control, we can realize the high output power of LC-enhanced electret generator over 40 hours for the first time. This means that long-term high-output-power LC-enhanced electret vibration generator can be realized with further discharge suppression by utilizing better impurity/humidity control onto generator.

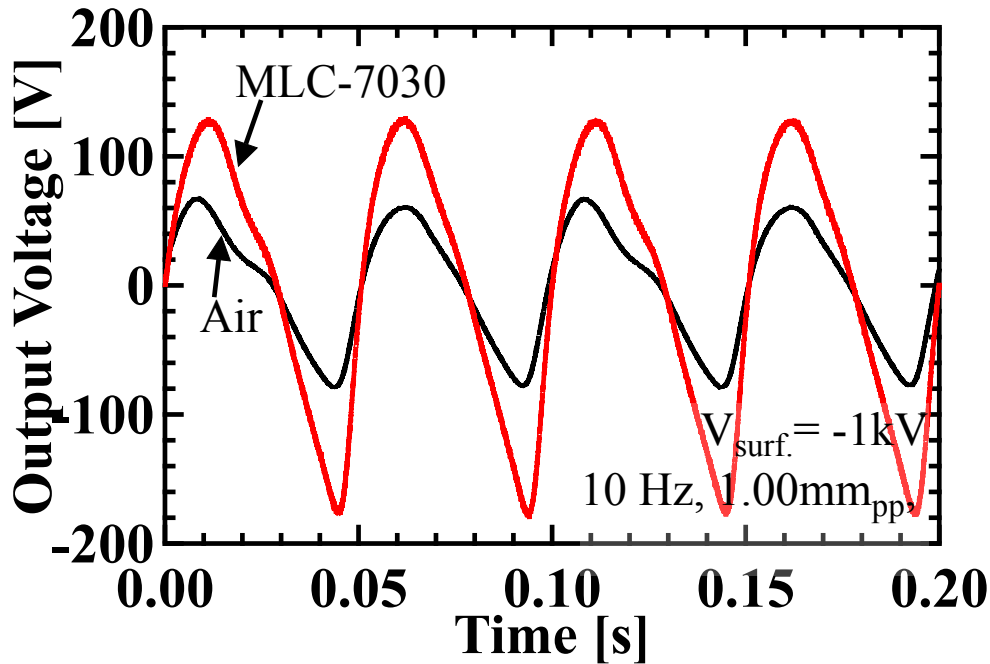


Figure 2.27 Output voltage waveform of conventional air gap electret generator and MLC-7030-filled-gap electret generator.

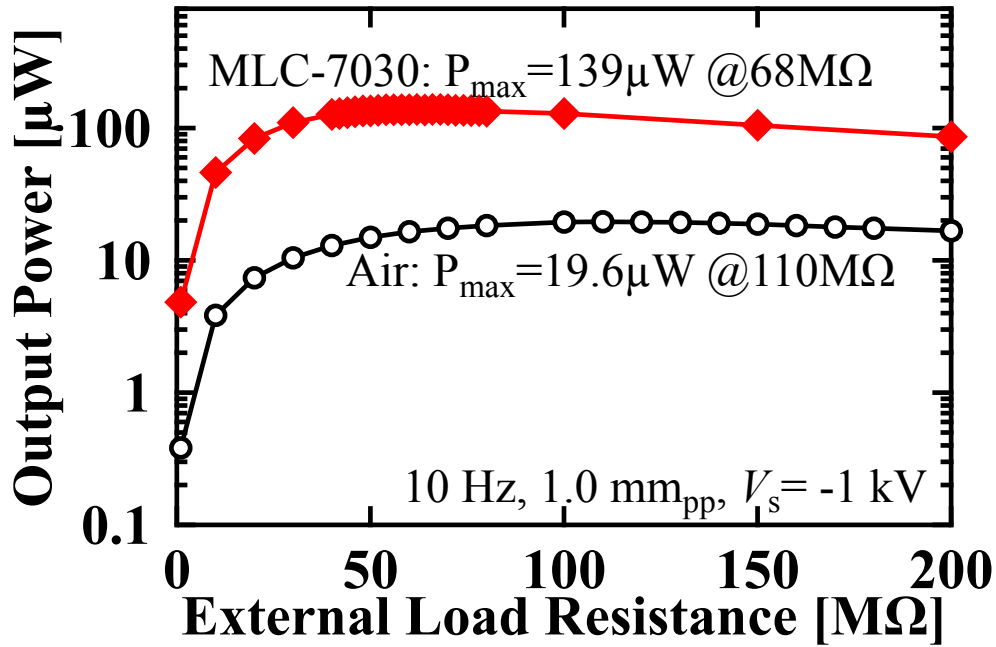


Figure 2.28 Output power versus load resistance at 0^{th} hour with conventional air gap and LC-filled gap.

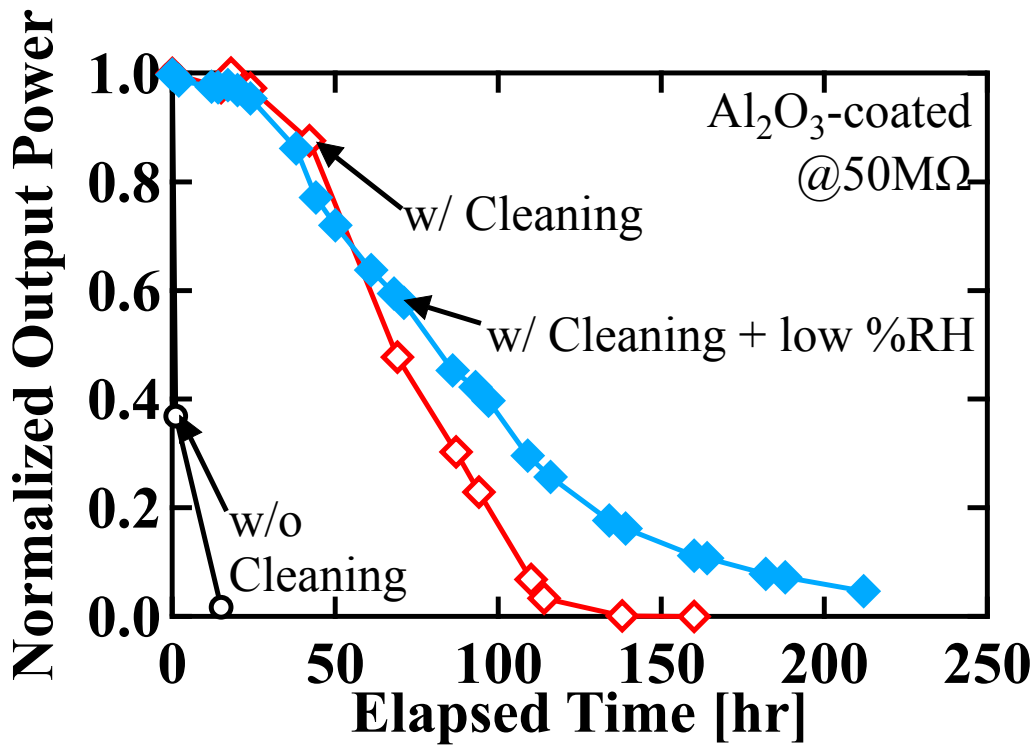


Figure 2.29 Decayed of normalized output power overtime between uncleaned, cleaned but not sealed and, cleaned and sealed LC-enhanced electret vibration energy harvester.

2.11 Chapter summary

The summary of this chapter is as the following;

- (1) Output power of electrostatic/electret vibration energy harvester is enhanced with anisotropic permittivity of nematic liquid crystal (LC). Up to 90-times output power enhancement can be achieved with common nematic LCs when compared to that of conventional energy harvester with air gap by boosting capacitance change from overlapping area change while limit the increase of parasitic capacitance.
- (2) High resistivity of the LC is found to be the necessary in realizing LC-enhanced electret vibration energy harvester. Based on preliminary experiment, resistivity of LC should be higher than $10^{16} \Omega \cdot \text{cm}$ to avoid the electret discharge
- (3) According to the trade-off characteristics between anisotropic permittivity and resistivity of nematic LC, MLC-7030 with anisotropic permittivity of 3.2 and resistivity over $10^{16} \Omega \cdot \text{cm}$ has been chosen. With MLC-7030, 7-times higher output power compared to conventional air-in-the-gap generator has been achieved.
- (4) By employing adequate impurity and humidity control, such as cleaning and keeping relative humidity below 10%RH, on the energy harvester and environment, LC-enhanced electret vibration energy harvester has been realized for the first time. Enhanced output power can be maintained for over 40 hours. Further suppressing impurity and humidity with better techniques would result in high output power for longer time.

Chapter 3

Liquid Crystal Alignment Measurement and Development of Generator Model

Chapter 3 Liquid Crystal Alignment Measurement and Development of Generator Model

3.1 Chapter Introduction

This chapter discusses about the output power modelling of LC-enhanced electret vibration energy harvester and the effect of molecule alignment in such generator. Chapter 2 shows that the realization of high-output-power LC-enhanced electret vibration energy harvester is possible. On the other hand, more accurate output power prediction model is still required for better development of LC-enhanced electret vibration generator. To create the better model, the alignment of LC molecule inside the generator should be clearly verified in both static and dynamic situations.

3.2 Output Power Modelling with Field-Dependent Permittivity

For the future development of the LC-enhanced electret vibration energy harvester, the accurate output power prediction model is necessary.

Looking back to the permittivity as a function of electric field strength in chapter 2 (Figure 2.7) and our 1-D electrostatic model (Figure 2.11), it should be noted that the electric field E_1 caused by the overlapping area A_1 has high strength due to high surface potential V_{surf} of charged electret. On the other hand, the electric field E_2 is caused by the difference between output voltage and ground; in which from the experimental output voltage, we can clearly see that it is not as high as electric field E_1 . From this, we proposed the modified version of 1-D electrostatic model derived in chapter 2 for LC-enhanced electret vibration energy harvester. Its schematic is illustrated as Figure 3.1. Top electrodes are coated with electret layer of thickness t_e and relative permittivity of ϵ_e . It is connected to the ground. Furthermore, it has patterned implanted charge of surface potential V_{surf} . The dielectric gap with thickness g is filled with liquid crystal with its relative permittivity ϵ_i as a function of electric field E_i under each corresponding overlapping area; where $i = 1$ and 2. The bottom charge-collector electrodes are coated with insulation layer of thickness t_p and relative permittivity of ϵ_p . It is connected to external load resistance R with output voltage $V(t)$. Parasitic capacitance C_p existed between 2 electrode fingers.

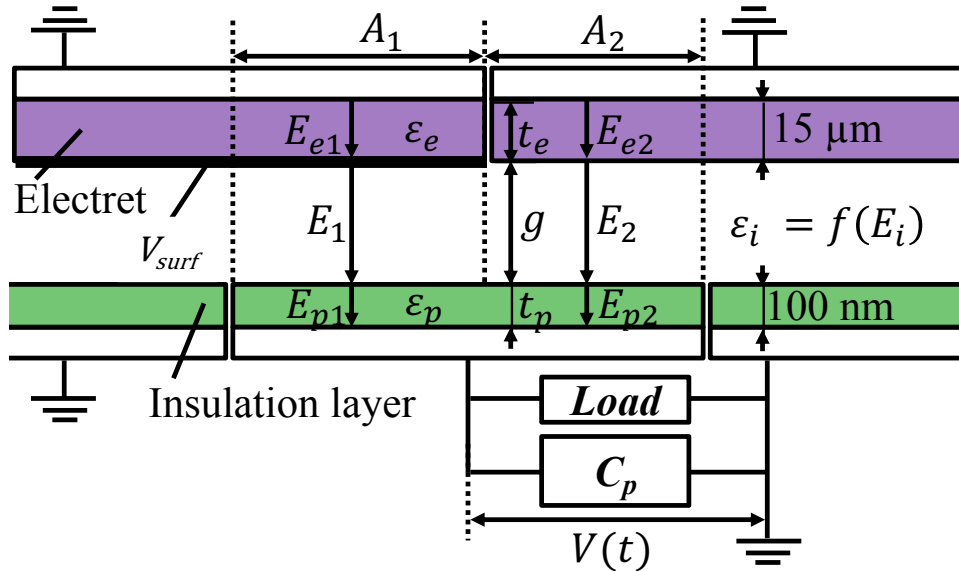


Figure 3.1 Schematic of 1-D electrostatic model with field-dependent permittivity.

Chapter 3 Liquid Crystal Alignment Measurement and Development of Generator Model

By using the same method for deriving previous 1-D electrostatic model, the modified 1-D electrostatic model with field-dependent permittivity is proposed as the following;

$$\frac{dV(t)}{dt} = - \frac{\frac{V(t)}{R} + \{B_1(V(t) - V_{surf}) + B_2V(t)\} \frac{dA_1(t)}{dt}}{C_p + B_1A_1(t) + B_2\{A_{max} - A_1(t)\}} \quad (3.1)$$

where $B_i = (\varepsilon_e \varepsilon_p \varepsilon_i(E_i)) / (\varepsilon_p \varepsilon_i(E_i)t_e + \varepsilon_e \varepsilon_p g + \varepsilon_e \varepsilon_i(E_i)t_p)$ and $i = 1$ and 2 .

In the same manner as previously proposed model, we could solve the equation (3.1) numerically to achieve output voltage and power using Runge-Kutta of the 4th order.

On the other hand, ε_i may not be consistent inside their overlapping regions due to the influence of V_{surf} and $V(t)$; in which, what would LC molecules will be most affected from. Additionally, C_p is founded to be closer to ε_{iso} than ε_{\perp} in chapter 2. It shows that LC molecule alignment at interdigital gap must be influenced by something. Thus, more detailed information of the LC molecule alignment inside the generator should be investigated. Furthermore, by understanding those influencing parameters, enhancement could be maximized. The methods for observing its alignment will be explained in later part.

3.3 Relationship between Relative Permittivity and Alignment Angle of LC

It is a challenge to observe the out-of-plane (y-axis) LC molecule alignment θ directly, even in standard LC cell. Figure 3.2a shows schematic of LC molecule alignment in parallel plate capacitor. On the other hand, θ could be derived from the common knowledge of permittivity tensor $\bar{\bar{\varepsilon}}$ for LC [89] as the followings;

$$\bar{\bar{\varepsilon}} = \begin{bmatrix} \varepsilon_{\perp} + \Delta\varepsilon n_x^2 & \Delta\varepsilon n_x n_y & \Delta\varepsilon n_x n_z \\ \Delta\varepsilon n_x n_y & \varepsilon_{\perp} + \Delta\varepsilon n_y^2 & \Delta\varepsilon n_y n_z \\ \Delta\varepsilon n_x n_z & \Delta\varepsilon n_y n_z & \varepsilon_{\perp} + \Delta\varepsilon n_z^2 \end{bmatrix} \quad (3.2)$$

where n_i represents the director of LC molecule in each direction with i corresponds to x , y , and z direction.

With the assumption of periodic condition in z -direction (the direction of electrode length), we can obtain;

$$\begin{aligned} n_x &= \cos \theta \\ n_y &= \sin \theta \end{aligned} \quad (3.3)$$

By substituting equation (3.3) into (3.2), we will have

$$\varepsilon_x = \varepsilon_{\perp} + \Delta\varepsilon \cos^2 \theta \quad (3.4)$$

$$\varepsilon_y = \varepsilon_{\perp} + \Delta\varepsilon \sin^2 \theta \quad (3.5)$$

Figure 3.2b shows the relationship between ε_x , ε_y and, θ from eq.(3.4) and (3.5). With some manipulation, we can rewrite ε_x and θ as;

Chapter 3 Liquid Crystal Alignment Measurement and Development of Generator Model

$$\varepsilon_x = 2\varepsilon_{\perp} + \Delta\varepsilon - \varepsilon_y \quad (3.6)$$

$$\theta = \arcsin\left(\sqrt{\frac{\varepsilon_y - \varepsilon_{\perp}}{\Delta\varepsilon}}\right) \quad (3.7)$$

Hence, based on eq. (3.6) and (3.7), if we could observe ε_y inside the generator, ε_x and θ could be clarified. On the other hand, sensing local ε_y is not feasible with direct measurement of impedance analyzing due to large electrode area; consequently, optical observation and its relationship with ε_y are chosen as the main technique for local molecule alignment measurement.

3.4 Liquid Crystal Alignment Measurement

In this part, LC alignment measurement will be investigated by 2 methods; 1) Fourier-Transform Infrared Spectrometry (FT-IR) and 2) Polarized Optical Microscopy (POM). FT-IR technique relies on the detection of specific infrared (IR) absorbance on chemical bonds to identify its species and amount of the bonds presented in the sample. On the other hand, POM measures the transmittance of the light through the sample under cross-polarizer. With both absorbance and transmittance data, relative permittivity and LC molecule alignment could be interpreted. This part organizes as the followings; working principle, sample fabrication, experimental setup, and results' discussion for each measurement methods.

3.4.1 Fourier Transform Infrared Spectroscopy

As stated above, FT-IR spectroscopy is a technique utilizing the infrared absorbance characteristics, unique to different type of bonding and bonded species. It also depends on the angle of the bonding to the electromagnetic axis of IR beam. The absorbance peaks correspond to certain bond vibration; either stretching or bending. The schematic of IR absorbance mechanism is shown as Figure 3.3. For liquid crystal, especially nematic liquid crystal with polar bonds align along its longitudinal axis (Figure 2.2 and Figure 2.3), the IR absorbance becomes high when the axis of the polar bond parallel to axis of IR field and vice versa. In other word, FT-IR spectroscopy is capable of detecting the change of the alignment of liquid crystal. It should be noted that, even with liquid crystal configuration that create lowest absorbance, the absorbance will not become zero due to the fact that it is obtained by the comparison between measured single beam data of liquid-crystal-filled cell and reference single beam data of empty cell.

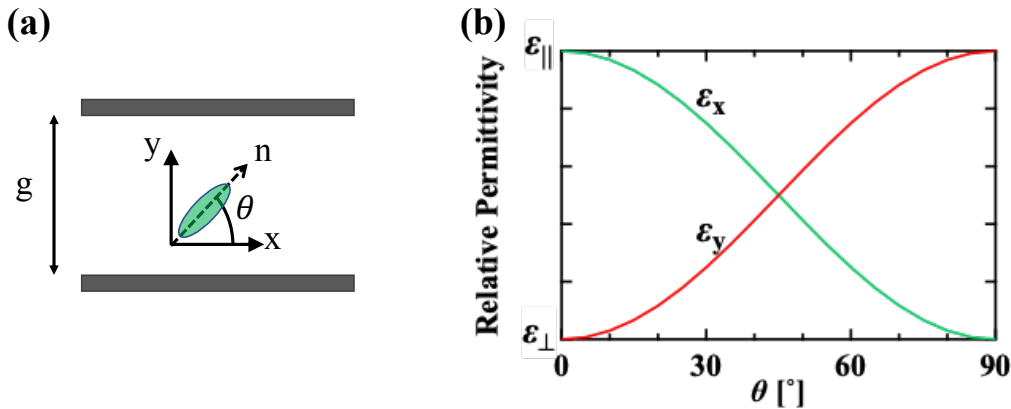


Figure 3.2 (a) Schematic of LC molecule alignment inside the parallel plate capacitor with dielectric gap g and (b) Relation of LC permittivity inside the gap and its alignment angle θ according to eq. (3.4) and (3.5).

Chapter 3 Liquid Crystal Alignment Measurement and Development of Generator Model

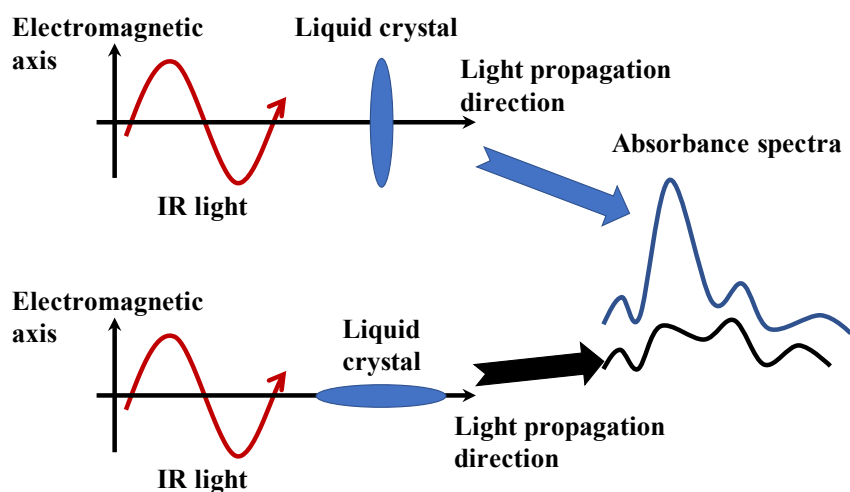


Figure 3.3 Schematic of FTIR spectroscopy with positive anisotropic liquid crystal shown as blue ellipsoid. When the electromagnetic axis of IR beam parallel to the liquid crystal molecule, the absorbance will be high, vice versa.

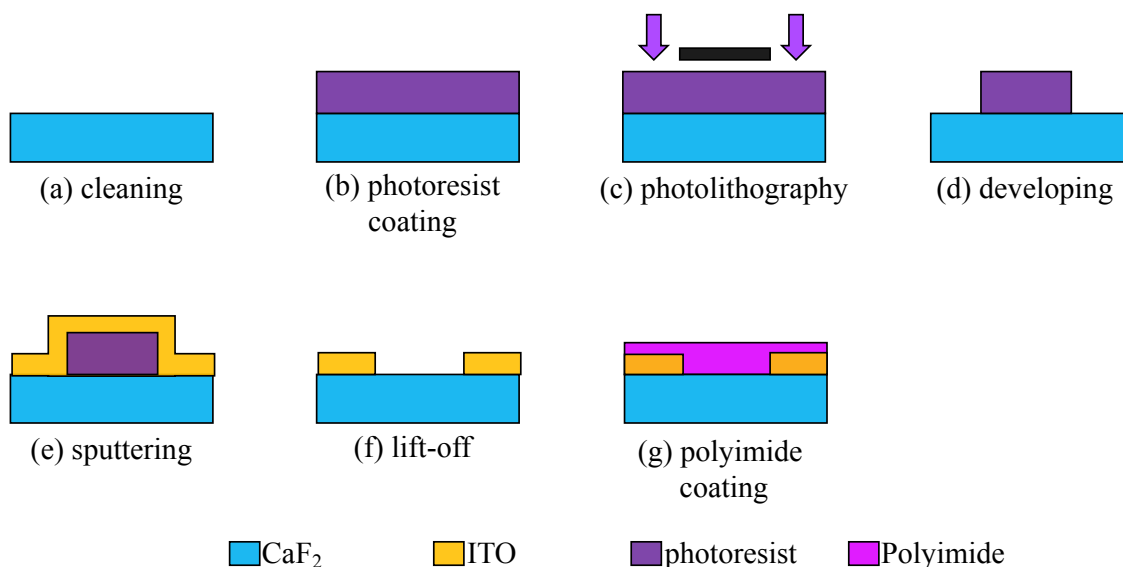


Figure 3.4 Schematic of fabrication process flow for FT-IR test cell.

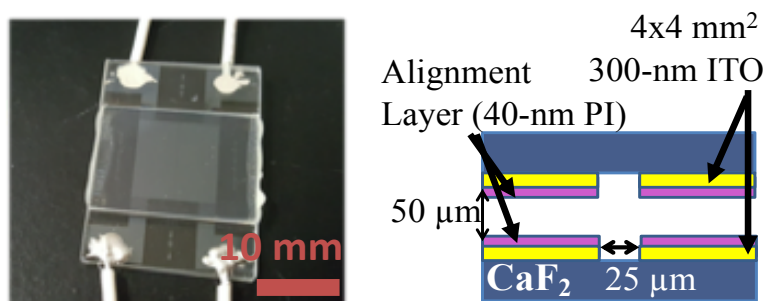


Figure 3.5 Photo of finished FT-IR test cell and the schematic of its cross-section

Chapter 3 Liquid Crystal Alignment Measurement and Development of Generator Model

3.4.1.1 Sample Fabrication for FT-IR Absorbance Measurement

For FT-IR absorbance measurement, the IR transmittance of the substrate is very important. In our study, we choose CaF_2 substrate which has good transmittance in IR range and quite transparent in visible wavelength. 300nm-thick ITO electrode is sputtered onto the substrate and patterned with lift-off process to avoid any use of etchant. The horizontal electrode gap is 25 μm . Then, 40nm-thick polyimide alignment layer (on the courtesy of Prof. Kato, Department of Chemistry and Biotechnology, The University of Tokyo) is spin-coated onto the sample and is rubbed in one direction. This ensures the initial alignment of the LC to be horizontal alignment. Next, 50 μm -thick gap spacer is used for gap control. The LC cell is then be assembling on the alignment machine (MA30tu, Nanometric Co. Ltd.). Figure 3.4 shows the schematic of the process flow. The photo of fabricated LC cell is shown in Figure 3.5. The dimension of the fabricated LC cell is half of the generator. Lastly, LC is filled into the LC cell.

3.4.1.2 Experimental Setup for FT-IR Spectroscopy

Figure 3.6 shows the schematic and photo of the setup for microscopic FT-IR spectroscopy. The FT-IR spectrometer (FT/IR-6600 and its microscopic extension, IRT-5200, JASCO) equipped with microscopic narrow band detector (MCT-N) is used in the measurement. The microscopic objective lens has the magnification of 32 times with numerical aperture of 0.7. With MCT-N, absorbance at wavenumber near IR region could be observed. FT-IR spectrometer is capable of measuring the small aperture size of 5 $\mu\text{m} \times 5 \mu\text{m}$ which is more than enough if we want to measure the detailed alignment of the liquid crystal in across the interdigitated gap in LC test cell. Next, the silicone cord heater is attached to the stage for temperature regulation; it is connected to temperature controller unit (TRC201, Multi Controller, Taketsuna Manufactory Co., Ltd.). The thermocouple is attached to the stage of microscopic FT-IR spectrometer for monitoring the temperature. To maintain liquid crystal state, the stage is kept constant at 30°C during the measurement.

The liquid crystal cell is put onto the microscopic FT-IR stage. The setting parameters are set. The impedance analyzer is connected to the liquid crystal cell to provide the alternating electric field from bottom electrode; similar to output voltage. Top electrode is connected to Source Measure Unit (2410 SourceMeter® SMU, Keithley™). LC used in this experiment is BCH-5F.F.F and its characteristic IR wavenumber are 1248 and 1366 cm^{-1} which corresponds to its C-F bonds. For this experiment, we choose IR wavenumber of 1366 cm^{-1} as the primary signal for the LC molecule alignment in this study.

On the preliminary test, it is founded that the optimal spatial resolution is 9 $\mu\text{m} \times 9 \mu\text{m}$ for our test LC cell. The detail about aperture sizes can be find in appendix B. Although the aperture size is larger than what we desire, it is still adequate for observing the local alignment change along interdigital gap; albeit, with smaller detail. Furthermore, the relationship between relative permittivity in y-direction ε_y and IR absorbance Abs of BCH-5F.F.F when the applied electric field is increasing as shown in Figure 3.7. From this, we could establish the relation equation between IR absorbance and permittivity as in the following equation:

$$\varepsilon_y(Abs) = 2.93 + 10.22 \exp\left(-\frac{Abs - 1.10}{0.0532}\right) \quad (3.8)$$

Chapter 3 Liquid Crystal Alignment Measurement and Development of Generator Model

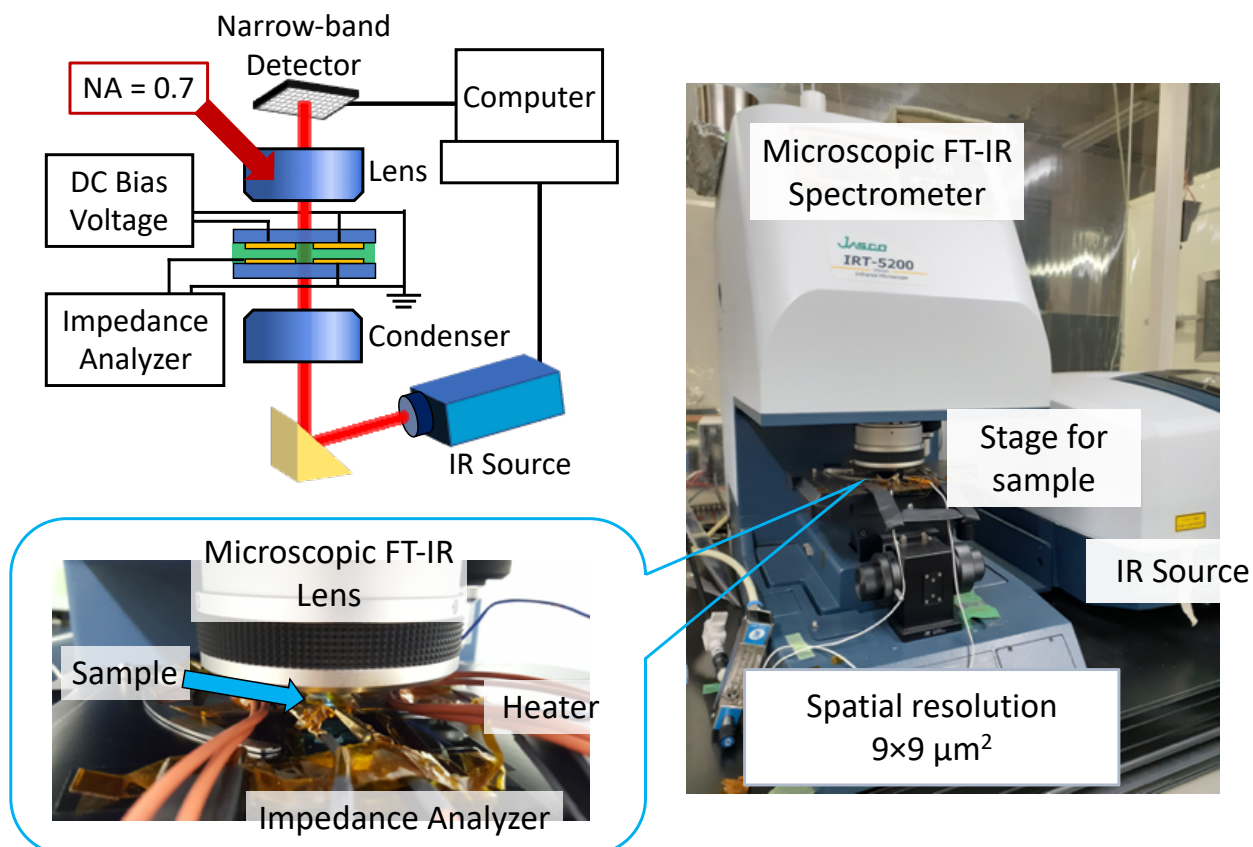


Figure 3.6 Schematic of the setup for microscopic FTIR spectroscopy, photo of microscopic FT-IR spectrometer and, its zoom-in photo of the setup.

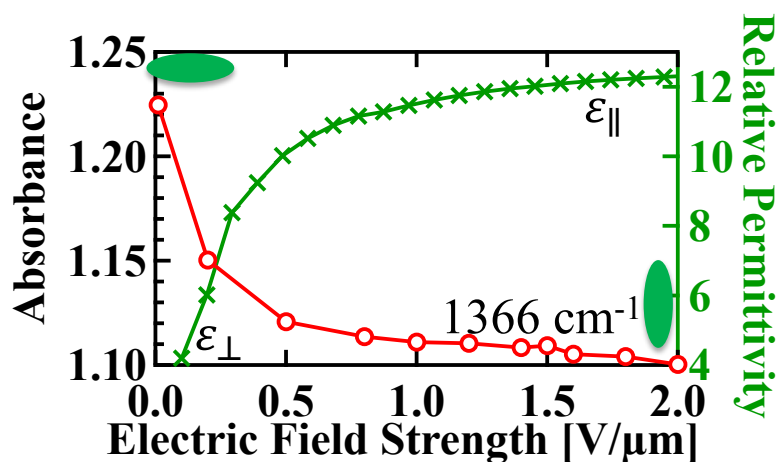


Figure 3.7 Relationship between IR absorbance, relative permittivity and, electric field strength.

Chapter 3 Liquid Crystal Alignment Measurement and Development of Generator Model

It should be noted that the change of the absorbance of LC between vertical and horizontal alignment is quite small (1.25 to 1.10) due to the thickness of LC layer (50 μ m) causing quite low transmittance. With sufficient detection time, the signal-to-noise ratio is maximized; leading to increase in accuracy and precision of the measurement.

3.4.1.3 *Liquid Crystal Measurement with FT-IR Spectroscopy*

In this measurement, 2 electrical conditions are employed; 1) grounded and 2) imitation of generator. Firstly, all electrodes of LC cell are grounded. The IR absorbance measurement shows high IR absorbance, corresponding to transverse permittivity of BCH-5F.F.F, across the LC cell. This indicates that, in the absence of electric field, LC aligns horizontally due to the alignment layer as shown in Figure 3.8a. When the voltage is applied onto top electrode, imitating high surface-charged electret, the absorbance shows the gradual change from low to high across the interdigital gap. This corresponds to axial permittivity of BCH-5F.F.F under high electric field region and transverse permittivity under grounded region and vice versa as shown in Figure 3.8b. In other words, LC aligns vertically in the presence of high electric field from applied voltage; while it is gradually changed to horizontal alignment in the grounded region across the interdigital gap as shown in Figure 3.8c.

From the measurement, we found that the LC alignment around interdigital gap is affected by fringe electric field up to 100 μ m-lateral-distance from the edge of electrode; i.e., LC alignment near the electrode edge is not consistent to that of center of electrode. From the average permittivity in the dielectric gap, this does not affect overall relative permittivity used for output power model. For further development of more accurate output power model, the dynamic alignment of the LC inside the generator will be elucidated.

Regrettably, we later found that dynamic mode of FT-IR spectrometer is not suitable for our LC cell with dimension of half-size generator. This is due to the fact that LC layer is quite thick (50 μ m) causing low signal-to-noise ratio when the shutter speed is high. On the other hand, further scaling down the LC cell is undesirable since dimension of interdigital gap will be comparable to spatial resolution of FT-IR; resulting in unrefined measurement of LC molecule alignment at interdigital gap. Henceforth, we choose to employ POM technique for measuring dynamic LC alignment.

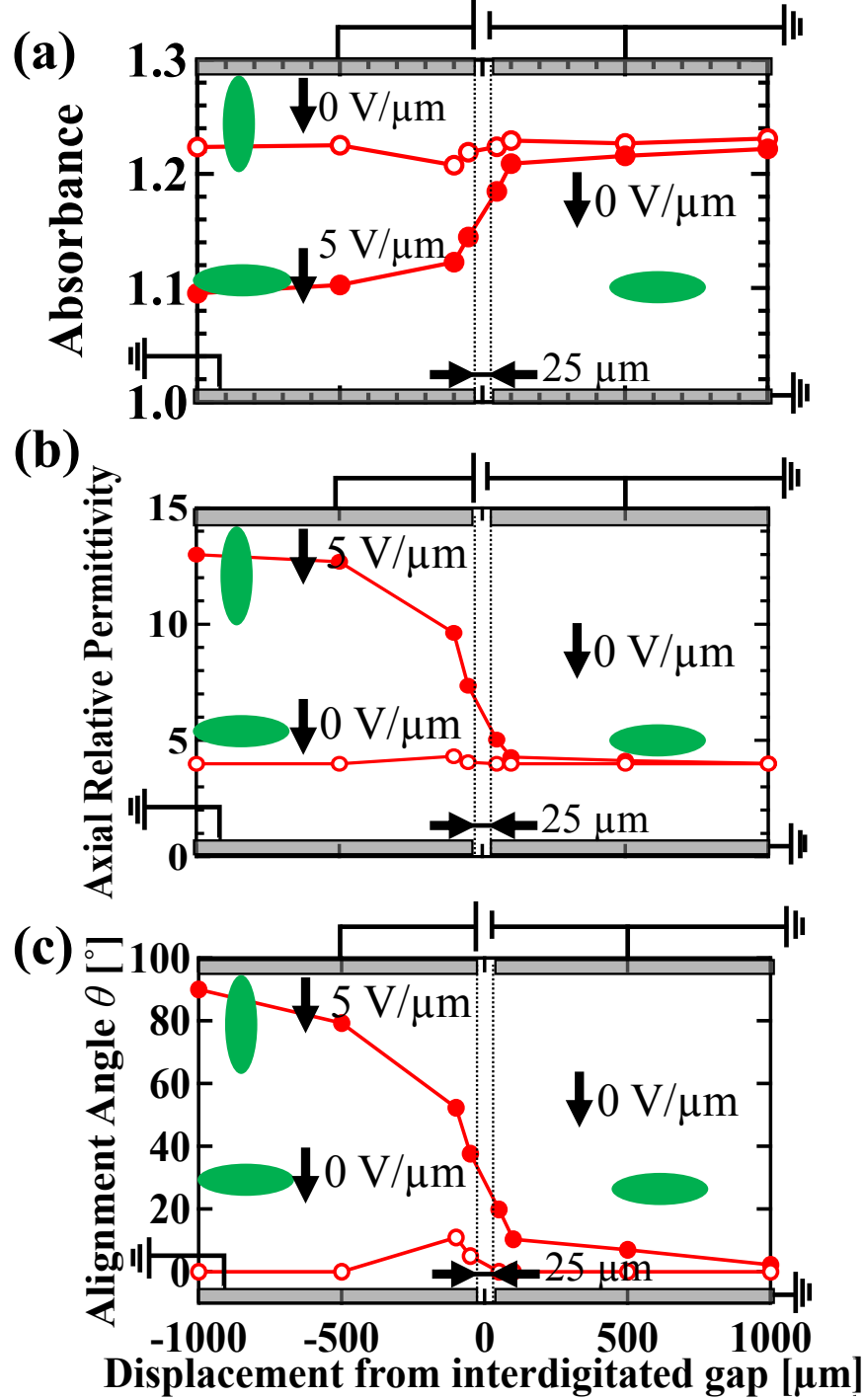


Figure 3.8 (a) IR absorbance of BCH-5F.F.F in FT-IR test cell with and without electric field and its corresponding (b) axial permittivity and (c) alignment angle. Green ellipsoids represent the interpreted alignment of LC at each region.

Chapter 3 Liquid Crystal Alignment Measurement and Development of Generator Model

3.4.2 Polarized Optical Microscopy

Polarized optical microscopy or ‘POM’ utilizes the light-bending ability of properly aligned LC molecules. For the example, the light can pass through the LC cell when LC aligns horizontally under cross-polarizer. Depends on the planar LC alignment according to the cross polarizer, the transmittance of the light over the LC cell is calculated. Transmittance is the highest when planar LC alignment is 45° to both polarizer and analyzer. On the other hand, vertically aligned LC cannot bend the light; thus, the transmittance is 0. Figure 3.9 shows the schematic of the working principle of POM technique.

3.4.2.1 Sample Fabrication for POM Measurement

Unlike the LC cell fabricated for IR absorbance measurement, substrate with good IR transmittance is not required; thus, instead of CaF_2 substrate, TEMPAX substrate is used. Additionally, the thickness of LC layer can be the same as that of actual generator. The fabrication process is similar to that of electret energy harvester in output power generation experiment in chapter 2. Briefly, 100nm-thick ITO electrode is sputtered onto the substrate. Standard photolithography process is performed to patterned ITO electrode. 100nm-thick Al_2O_3 insulation layer is deposited onto charge-collector electrode with the use of ALD technique. On electret electrode, 15 μm -thick CYTOP-EGG is spin-coated as electret material. Both electret electrode and charge-collector electrode are cleaned with IPA in ultrasonic bath for 5 minutes. Electret electrode is then charged to -1kV using soft x-ray charging technique. Figure 3.10 shows the fabricated electrodes. The dimension of the electrode is that same as those fabricated in chapter 2 (Table 2.2).

3.4.2.2 Experimental Setup for POM

Inverted polarized optical microscope (IX71, OLYMPUS) equipped with high-speed camera (FASTCAM NOVA, Photron) is used for measuring the dynamic LC molecule alignment in LC-enhanced electret vibration generator. The environmental chamber with an optical window is employed to avoid the unwanted effect of moisture/oxygen in the atmosphere. The top vacuum state is connected to 5-axis stage through the flexible arm while the bottom vacuum stage on a 1-D guide rail inside the chamber is connected to an AC servo electric motor (NMX620, Oriental Motor) through a crank mechanism. The environmental chamber is situated between a cross-polarizer. The electret electrode is mounted onto top vacuum stage. The charge-collector electrode is set on bottom vacuum stage and connected to external load resistance. The output current is connected to a programmable current-to-voltage amplifier/converter (CA5350, NF) with the gain of 1V/ μA . The dielectric gap between charge-collector and electret electrode is kept at 100 μm with confocal laser microscope (LT-9500, KEYENCETM) and filled with MLC-7030. The vibration frequency and amplitude are set up to be 10 Hz and 1mm_{peak-peak}, respectively. Figure 3.11 shows the schematic of the setup, Figure 3.12 shows the photo of the inside of environmental chamber and, Figure 3.13 shows the photo of assembled environmental chamber with the view of crank mechanism..

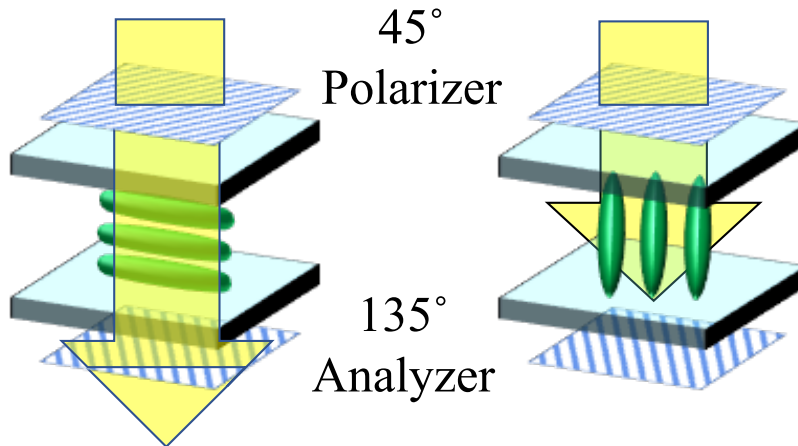


Figure 3.9 Light bending principle of LC under POM. When LC's planar alignment is in-between cross-polarizer, the light is bend. Vertical alignment poses no light bending capability

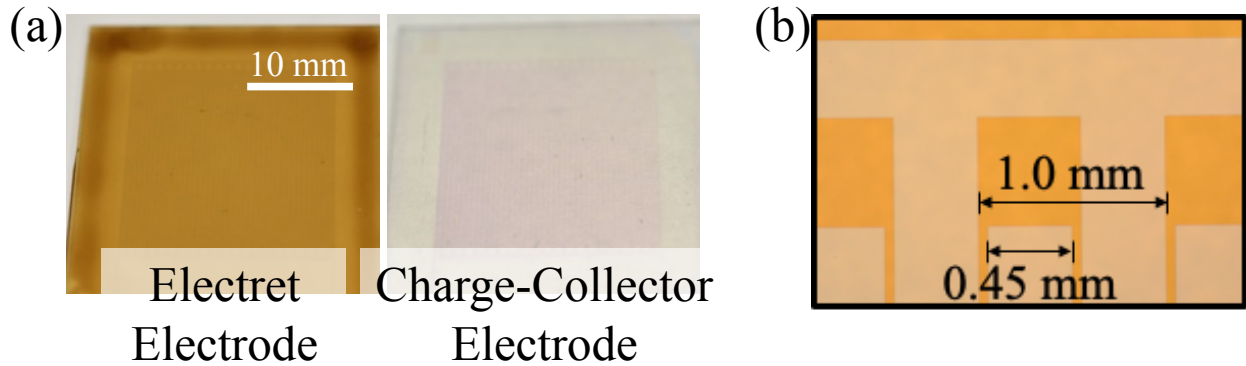


Figure 3.10 Photos of a) finished electrodes for POM experiment and zoom-in image.

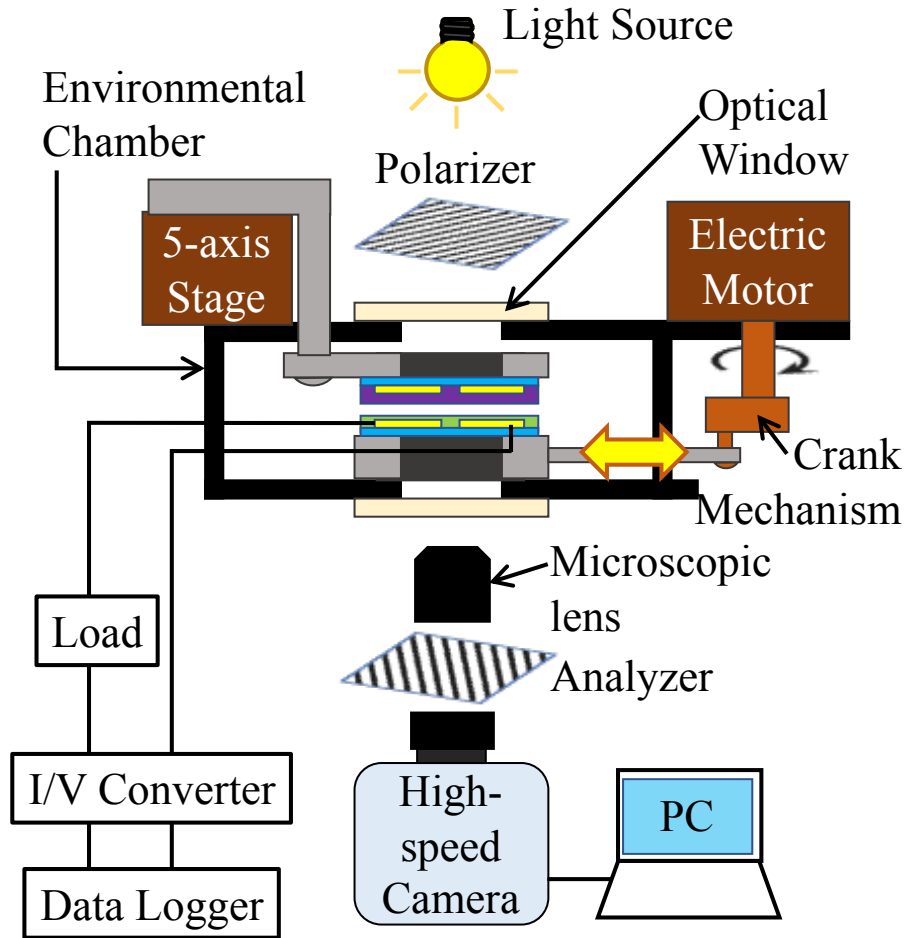


Figure 3.11 Schematic of POM experimental setup.

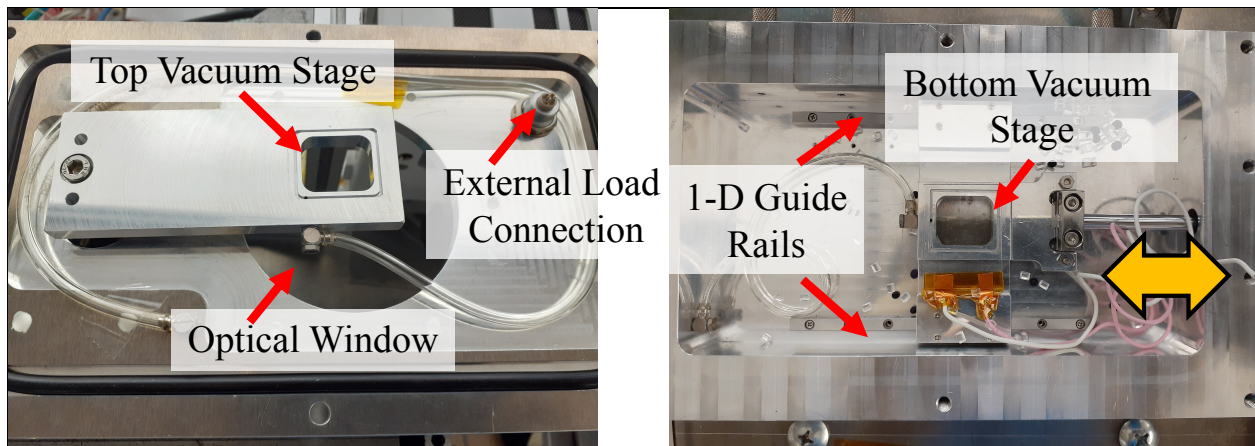


Figure 3.12 Photos of the inside of environmental chamber.

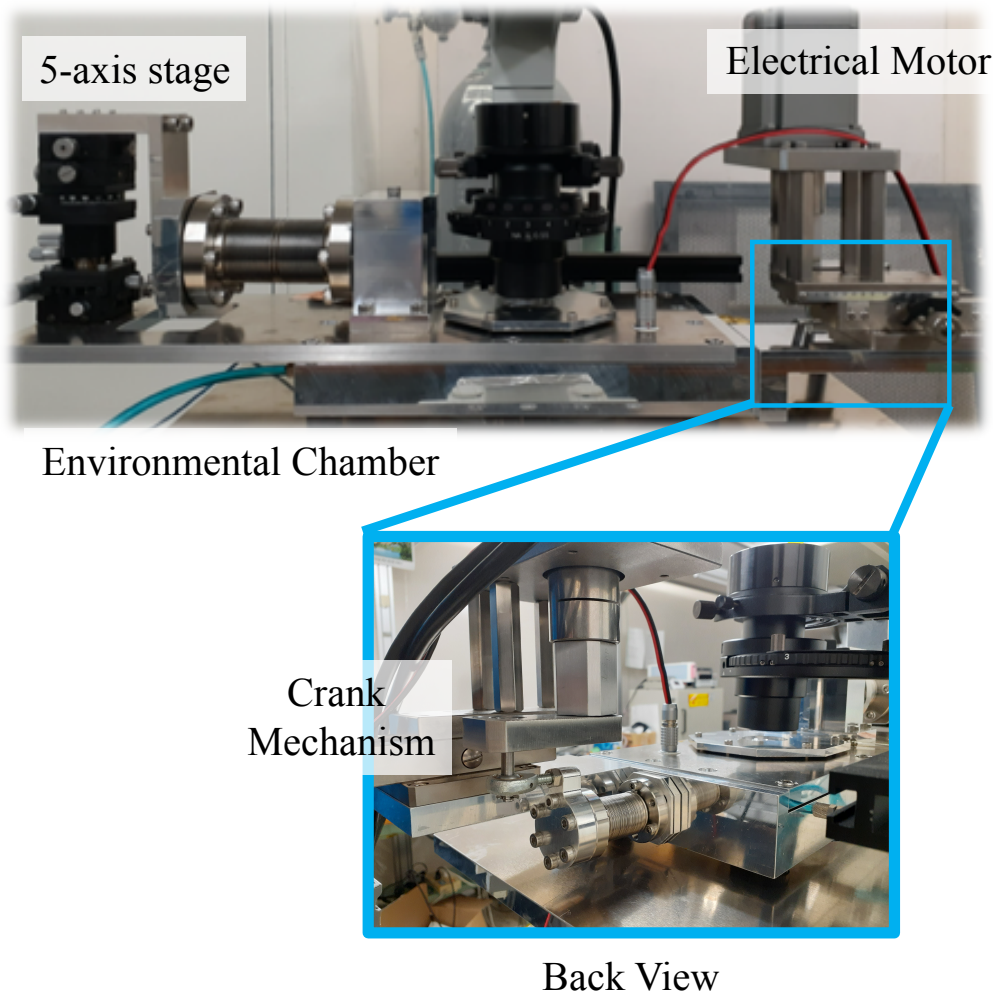


Figure 3.13 Photo of the environmental chamber and the zoom-in photo of crank mechanism.

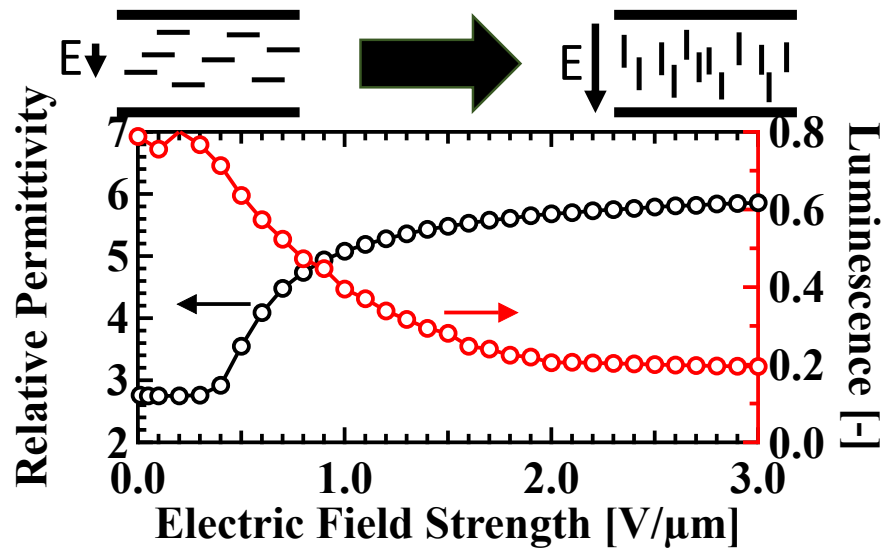


Figure 3.14 Relationship between permittivity, luminescence and, electric field strength.

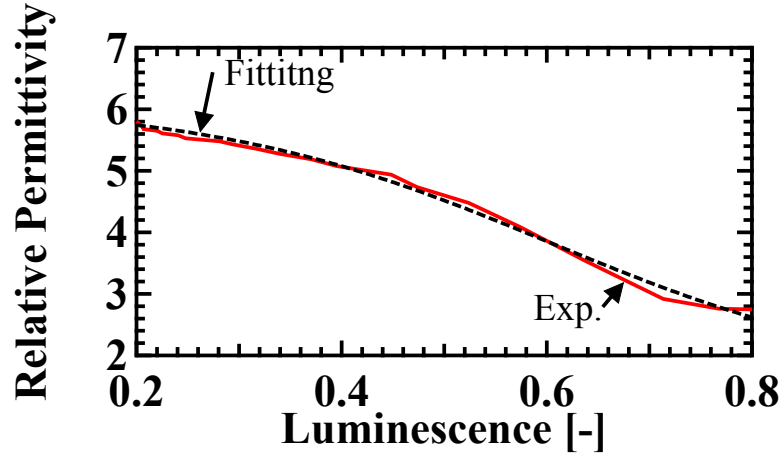


Figure 3.15 Relative permittivity as a function of luminescence.

In our preliminary experiment for POM, similar to IR absorbance measurement, the relative permittivity in y-direction ϵ_y as shown in Figure 3.14 is curve fitted with the luminescence L as in the following;

$$\epsilon_y(L) = 6.117 - \left\{ \frac{4.5703}{1 + \exp \frac{0.6035 - L}{0.1664}} \right\} \quad (3.9)$$

With this relation, the luminescence data of the POM images can be converted into ϵ_y as shown in Figure 3.15.

3.4.2.3 Dynamic Molecule Alignment Measurement of LC with POM

The output power generation experiment is performed and dynamic molecular alignment of LC is captured at optimal resistance. Figure 3.16 shows the output power versus external load resistance. With the current setup and MLC-7030, the maximum output power is 111 μW at 60M Ω which is about 5.5 times higher compared to conventional air gap (21 μW @100M Ω). With the shutter speed of 2 ms, the captured POM images at each selected time step are shown in figure 3.16. Since the movement of the electrodes and resultant alignment change is periodic, the images of only half a period (50ms) are shown. The dark area at 0ms indicates the vertical alignment of LC under high surface potential of electret while the bright area is resulted from the horizontal alignment of LC. From equations (3.9), (3.6) and, (3.7), luminescence data is converted into ϵ_y , ϵ_x and θ , respectively, as shown in Figure 3.17 and Figure 3.18.

From the results, it is clearly confirmed that the LC under electret with high surface potential will mostly align with high electric field from electret with almost no effect from unsteady electric field produced by output voltage $V(t)$; i.e., LC molecules are in vertical alignment $\theta=90^\circ$. On the other hand, LC under electrode region without charged electret has been slightly affected resulting in non-uniform and tilted alignment whenever charge-collector electrode is passing through. Figure 3.19 shows the POM images, ϵ_y , ϵ_x and θ of

Chapter 3 Liquid Crystal Alignment Measurement and Development of Generator Model

open circuit condition which resulted in higher $V(t)$ compared to that of with closed circuit. As shown in blue dash circle, the induced alignment from $V(t)$ is more noticeable in open circuit condition. It is also founded that the molecule alignment does not show any lateral shifting during the operation. This indicates the negligible or nil effect of oscillating flow on LC alignment.

Furthermore, the effect of fringe electric field between charge-collector and ground electrodes on the alignment of LC is observed as shown in 3.16-18 as ϵ_x at interdigital gap. Based on similarity between 3 different conditions of ϵ_x at interdigital gap overtime as shown in Figure 3.20, closed circuit with optimal resistance, short circuit to ground and, open circuit condition, it can be concluded that fringe electric field from $V(t)$ has only small effect on LC molecule alignment at interdigital gap. On the other hand, it shows that high electric field strength from $V_{surf.}$ has the dominant effect over realignment of LC molecule at interdigital gap.

Figure 3.20 also reveals that LC molecule alignment is dynamically changing over time. In other words, C_p is not the constant value as we previously believed for electret vibration energy harvester with permittivity-fluid-in-the-gap. By using Fast-Fourier-Transform (FFT) on the ϵ_x waveform data over 2-second time period, the dominant frequencies are founded to be 10, 20, 30 and, 40 Hz. With this information, we present the fitting function of ϵ_x at interdigital gap as in the following;

$$\begin{aligned} \epsilon_x(t) &= 4.1 + 0.41\sin(2\pi f_1 t + 1.13) + 0.44\sin(2\pi f_2 + 1.44) + 0.57\sin(2\pi f_3 + 4.9) \\ &\quad + 0.29\sin(2\pi f_4 + 2.1) \end{aligned} \quad (3.10)$$

where f_i is the frequency obtained from FFT with $i = 1, 2, 3$, and 4; corresponding to 10, 20, 30, and 40 Hz, respectively. The coefficients and phase differences are the results from fitting.

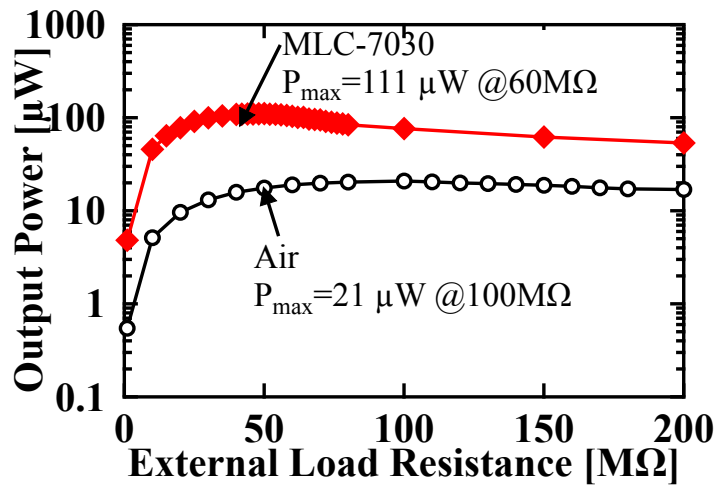


Figure 3.16 Output power versus load resistance of generator with POM setup..

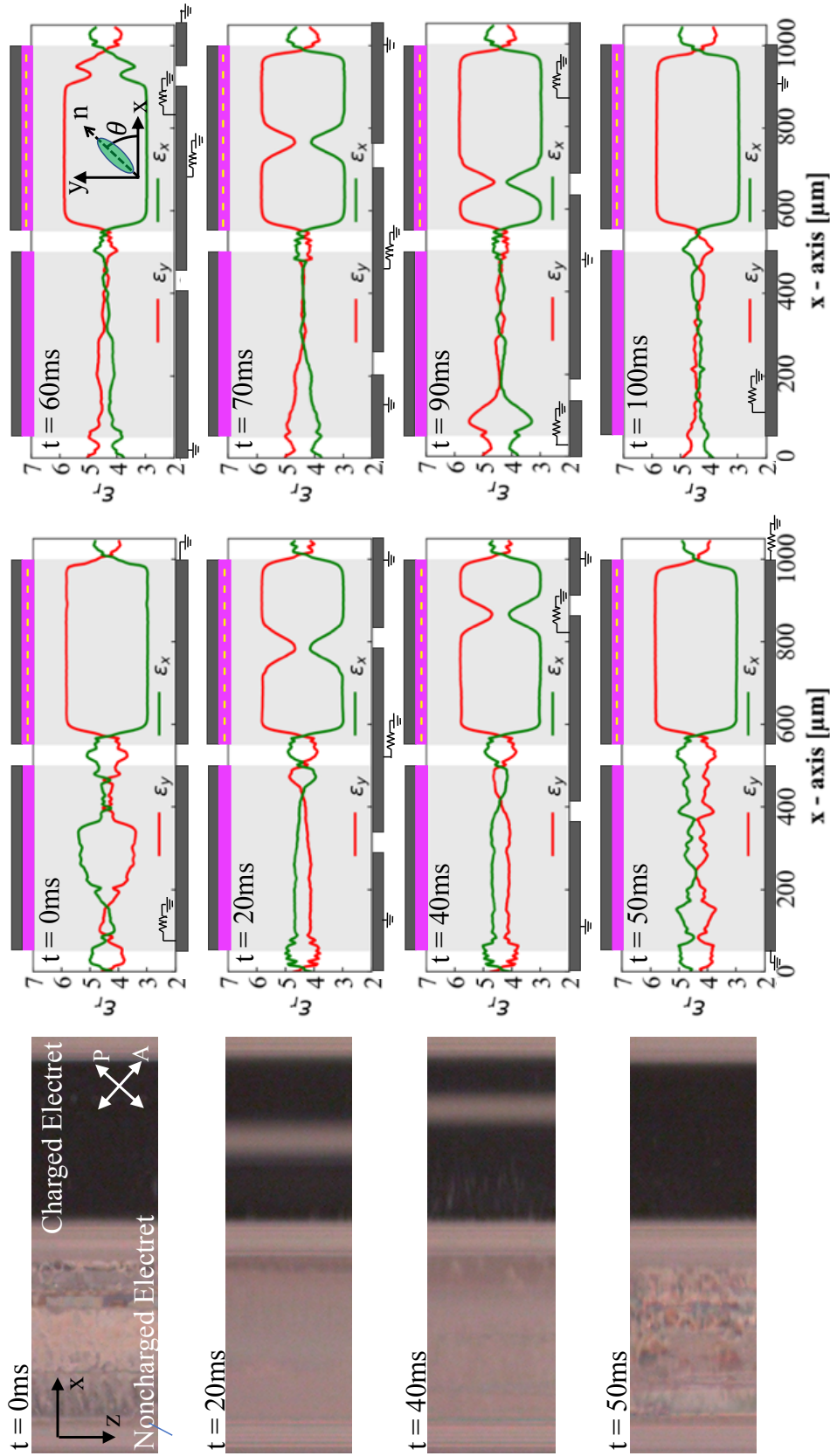


Figure 3.17 POM images of LC-enhanced electret vibration energy harvester during operation at optimal resistance and its interpretation of relative permittivity in 1 period.

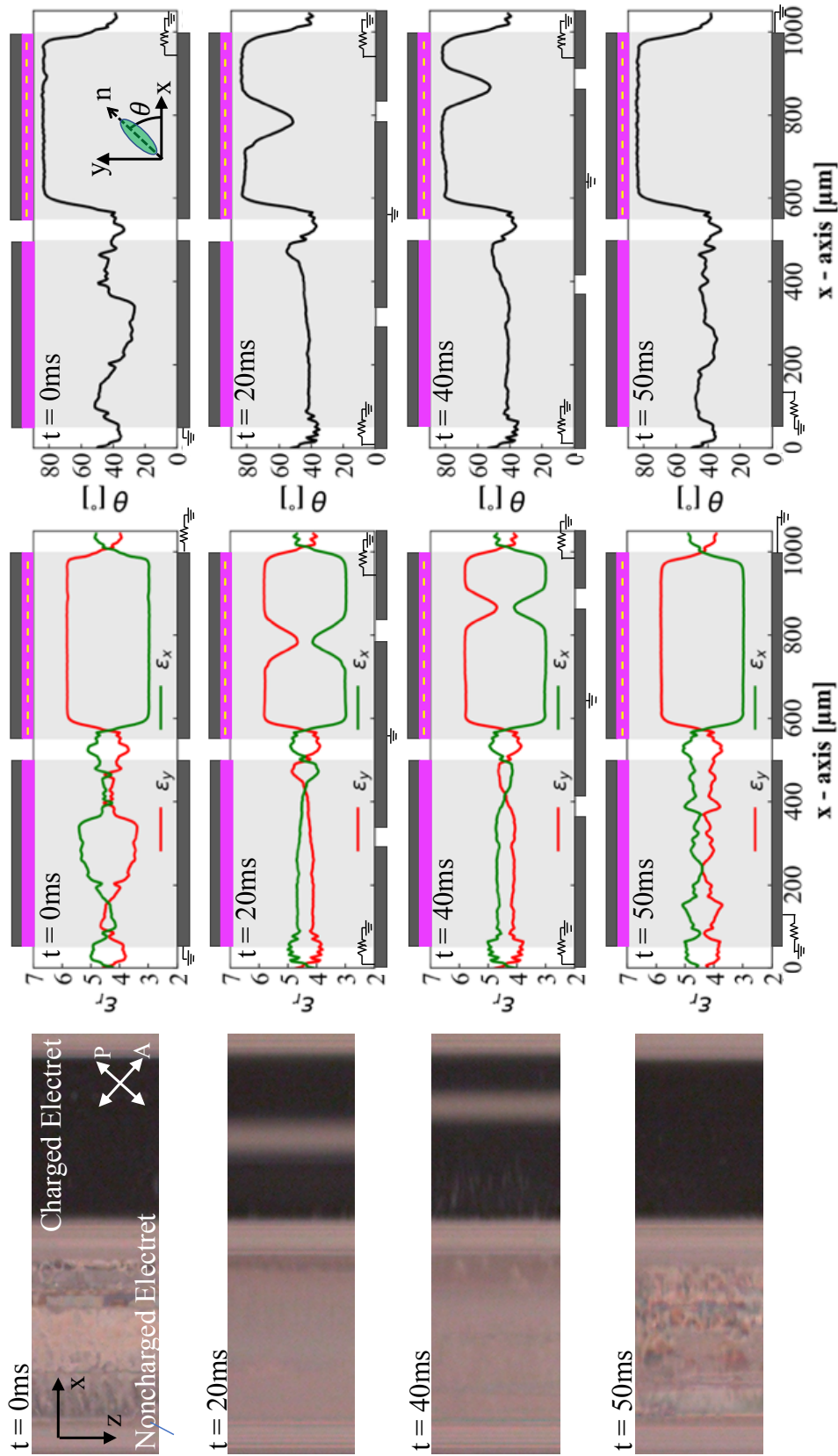


Figure 3.18 POM images of LC-enhanced electret vibration energy harvester during operation at optimal resistance and its interpretation of relative permittivity and alignment angle inside the generator within 1/2 period.

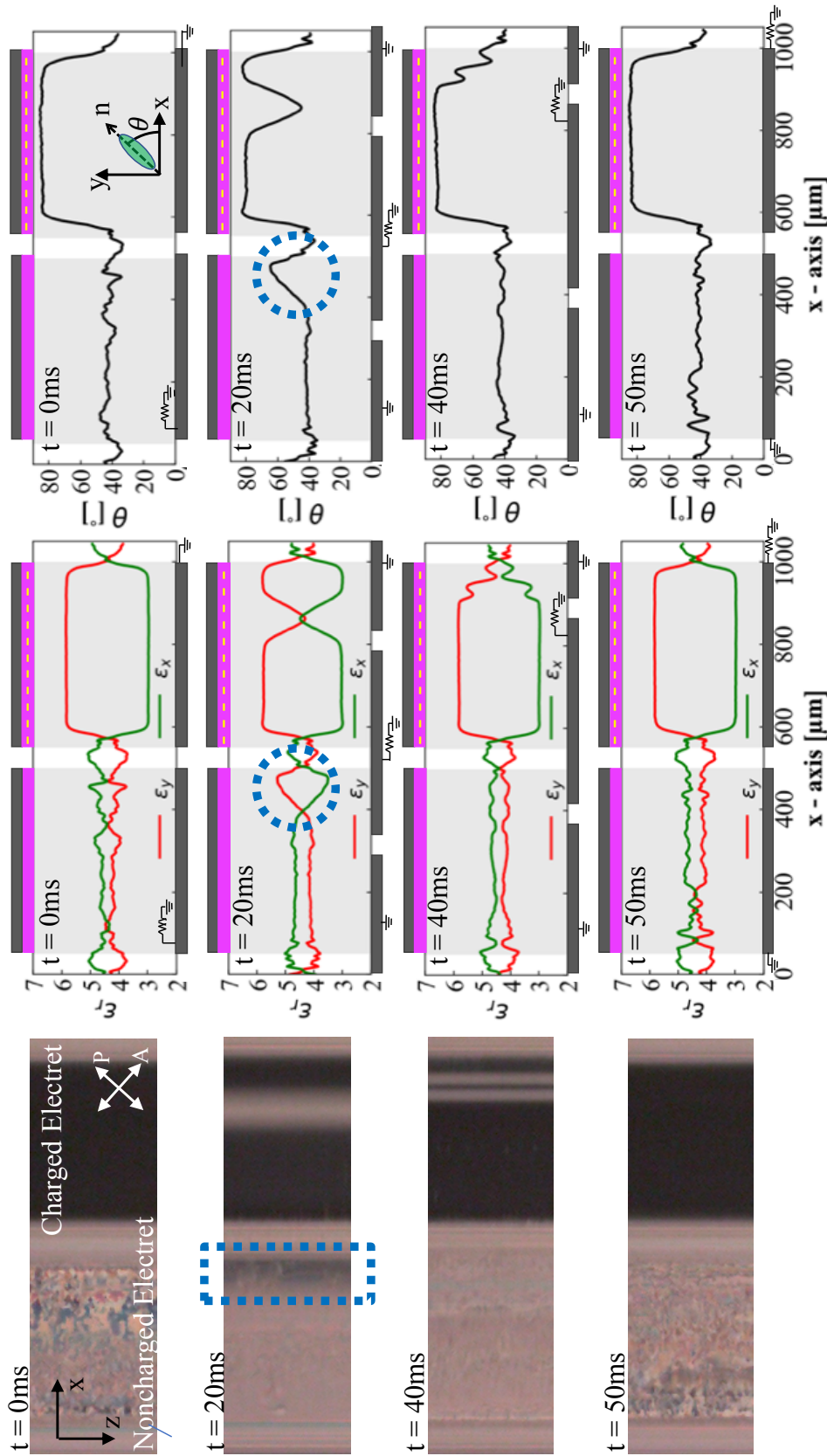


Figure 3.19 POM images of LC-enhanced electret vibration energy harvester during operation in open circuit condition and its interpretation of relative permittivity and alignment angle inside the generator within 1/2 period.

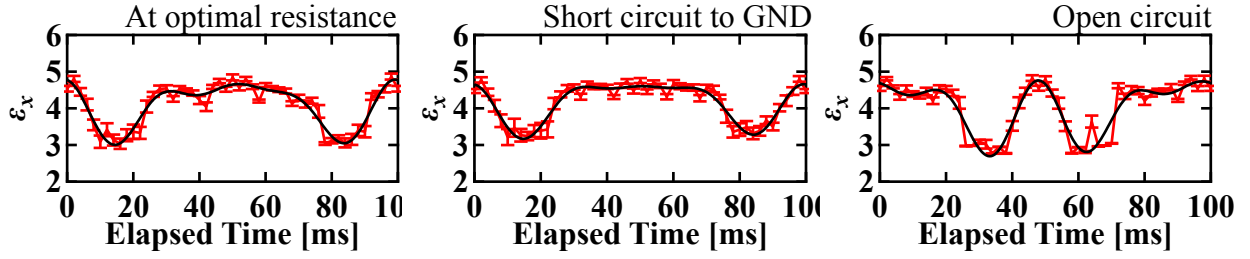


Figure 3.20 Horizontal permittivity at interdigital gap of charge-collector electrode overtime in different conditions; at optimal resistance, short circuit to ground and, open circuit condition. Each plot is the average of $N=20$ data set. Black line is the fit line from eq. (3.10).

Under charged electret Under grounded electret



Figure 3.21 Estimation of LC molecule alignment at interdigital gap under charged and grounded electret when assuming no intermediate alignment.

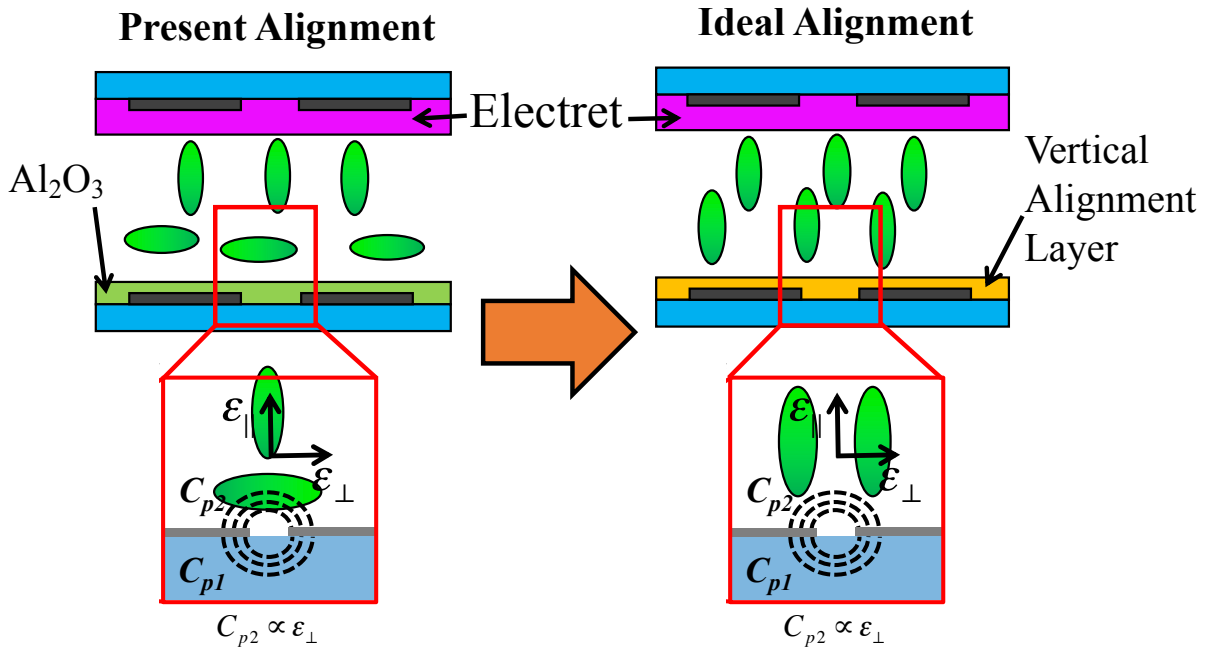


Figure 3.22 Schematic of LC molecule alignment in present and ideal alignment .

Chapter 3 Liquid Crystal Alignment Measurement and Development of Generator Model

These information, hence, indicates that the LC molecule alignment is not completely aligned vertically at the interdigital gap; resulting in slightly larger C_{p2} than first expected. By assuming no intermediate alignment between vertical and horizontal alignment at interdigital gap region and let α be the portion of LC in vertical alignment along the thickness of LC layer, we could estimate the percentage of LC molecule alignment using the observed vertical permittivity at the interdigital gap as in the followings:

$$\varepsilon_{y,@IDG} = \varepsilon_{\parallel}\alpha + \varepsilon_{\perp}(1 - \alpha) \quad (3.11)$$

Based on equation (3.11), under charged electret region, it is estimated that 69% of LC layer at interdigital gap aligned vertically; i.e. 31 μ m-thick of LC near charge-collector electrodes should be in horizontal alignment since LC molecules near charged electret electrodes must be affected by high electric field from electret and aligned vertically.

On the other hand, about 38% of LC layer is approximated to be in vertical alignment under grounded-electret region. Since LC with positive anisotropic permittivity tends to align vertically on hydrophobic surface and electret, CYTOP-EKG, is hydrophobic, 38 μ m-thick of vertically aligned LC molecules should be situated closed to grounded electret surface. Figure 3.21 shows the estimated percentage of vertically and horizontally aligned LC molecules at interdigital gap.

Looking closely, it could be seen that LC molecules at interdigital gap aligned horizontally near charge-collector electrodes. The cause of such alignment is from Al_2O_3 insulation layer which acts as horizontal alignment layer. Based on these estimations, it can be concluded that near-wall alignment affects LC molecules alignment in bulk layer up to about 30- μ m thick. This also shows that the C_{p2} can be further minimized if vertical alignment layer is employed to realize ideal alignment as shown in Figure 3.22 and Figure 3.23.

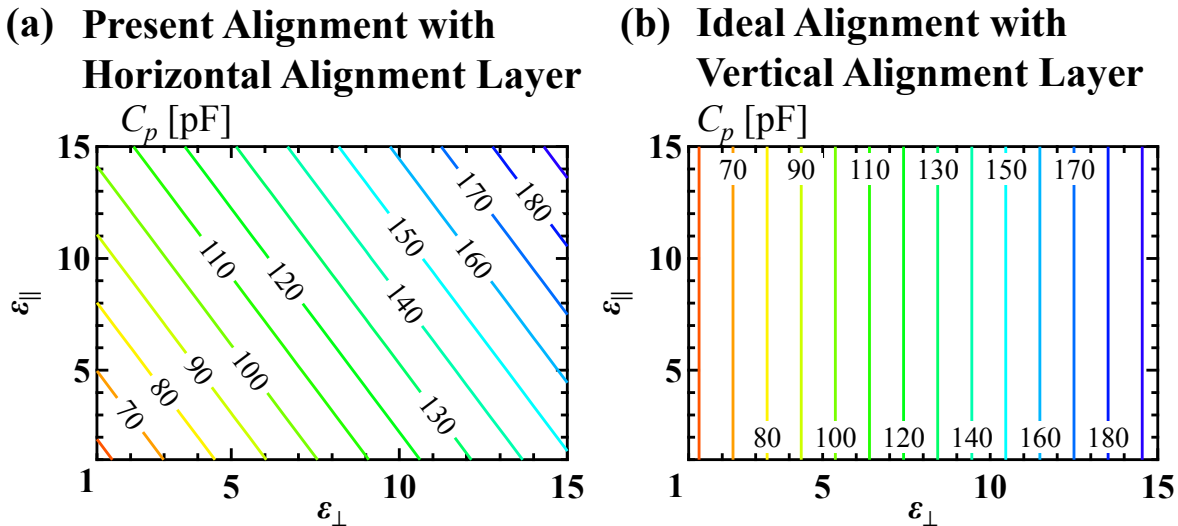


Figure 3.23 Simulated parasitic capacitance between a) present alignment and b) ideal alignment.

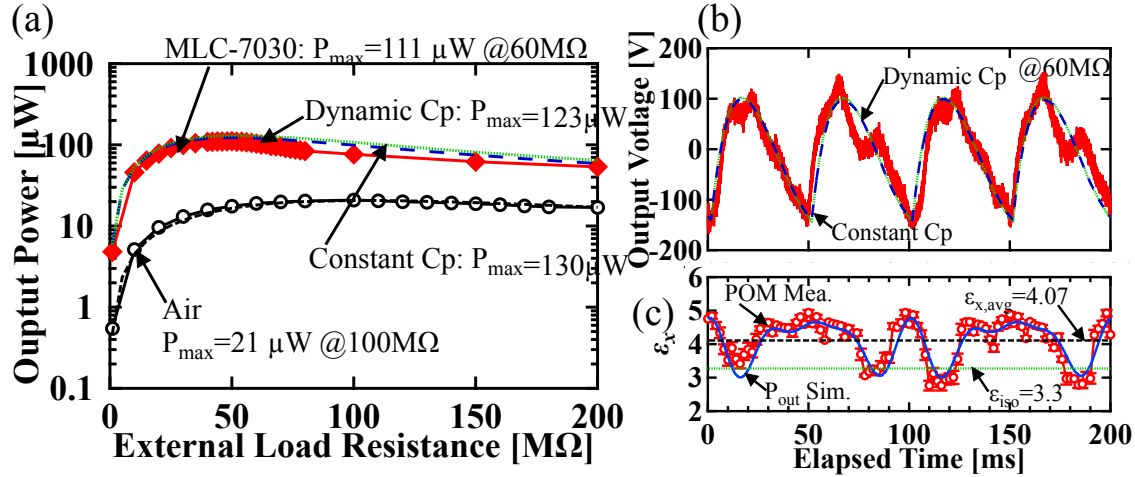


Figure 3.24 Comparison between experimental data, 1-D electrostatic model from eq.(3.1), constant C_p , and (3.11), dynamic C_p .

3.5 Output Power Modeling with dynamic permittivity and C_p

Utilizing the new knowledge obtained from the molecule alignment measurement of LC, we proposed the modified output power modeling with dynamic permittivity and C_p . Similar to that of in chapter 3.2, the differential equation of $V(t)$ can be rewritten as the following;

$$\frac{dV(t)}{dt} = - \frac{\frac{V(t)}{R} + \{B_1(V(t) - V_{surf}) + B_2V(t)\} \frac{dA_1(t)}{dt}}{C_p(t) + B_1A_1(t) + B_2\{A_{max} - A_1(t)\}} \quad (3.12)$$

where $B_i = (\epsilon_e \epsilon_p \epsilon_i(E_i)) / (\epsilon_p \epsilon_i(E_i) t_e + \epsilon_e \epsilon_p g + \epsilon_e \epsilon_i(E_i) t_p)$ and $i = 1$ and 2 .

With dynamic permittivity and C_p , the simulation results show better agreement compared to that of field-dependent permittivity and constant C_p as shown in Figure 3.24. The small difference in output power between 2 models may be caused by the small anisotropic permittivity of MLC-7030. Based on dynamic C_p , larger anisotropic permittivity LC is going to show lower than expected output power due to its higher time-average permittivity.

3.6 Performance Prediction for LC-enhanced Electret Vibration Energy Harvester

3.6.1 Output Power Enhancement

Based on the proposed 1-D electrostatic model with dynamic permittivity and C_p (eq.(3.12)), output power prediction has been performed. The simulation conditions are listed in Table 3.1. Figure 3.25a shows the output power enhancement simulation results as a function of anisotropic permittivity. It clearly shows that LC with large $\epsilon_{||}$ is more beneficial to output power enhancement compared to that of with high ϵ_{\perp} . On the other hand, LC with high resistivity should be used to prevent electret discharge. Therefore, $\Delta\epsilon$ of LC should be less than 5 according to trade-off characteristics of LC (Figure 2.19). This leads to the constriction of enhancement due to similarly large ϵ_{\perp} compared to $\epsilon_{||}$; the upper limit of the enhancement is found to be 12.

Chapter 3 Liquid Crystal Alignment Measurement and Development of Generator Model

Table 3.1 Simulation parameters for output power of LC-enhanced electret vibration harvester.

Parameters		
Dielectric gap	100	μm
Vibration amplitude	1.0	$\text{mm}_{\text{peak-leak}}$
Vibration frequency	10	Hz
Surface potential	-1000	V
Electrode area	20×20	mm^2
Pitch	1.00	mm
Electrode width	0.45	mm

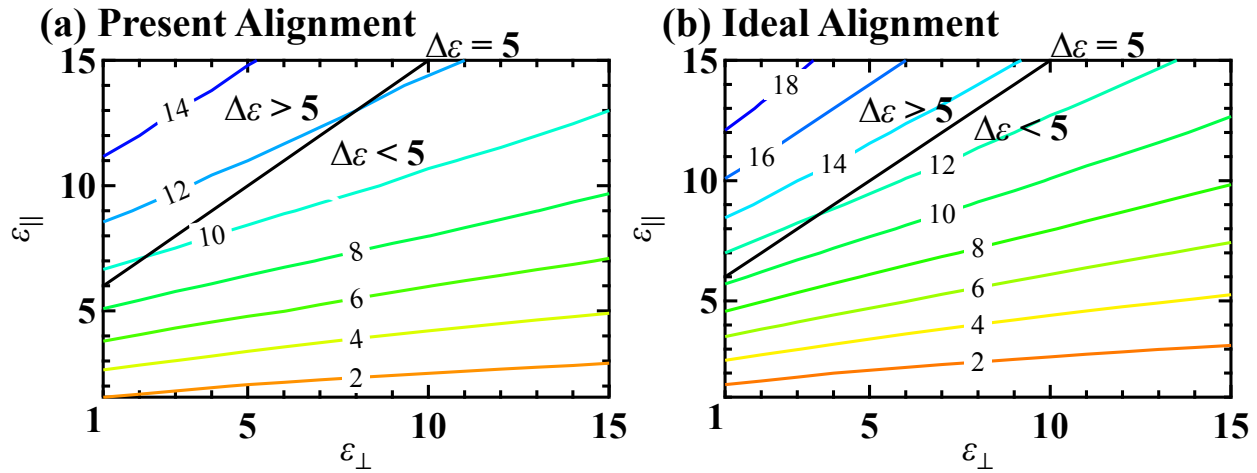


Figure 3.25 Simulated output power enhancement of LC-enhanced electret vibration energy harvester compared to conventional air gap as a function of anisotropic permittivity in a) present alignment and b) ideal alignment. Black solid line indicates fluid with $\Delta\epsilon=5$.

When LC molecules at interdigital gap aligned vertically, i.e. ideal alignment, C_{p2} is minimized and upper limit of enhancement reaches about 14 with $\Delta\epsilon$ of 5 as shown in Figure 3.25b. The small increase of enhancement limit between present and ideal alignment is due to the small reduction of C_p when $\Delta\epsilon$ is less than 5 as shown in Figure 3.23. On the other hand, the increase in enhancement with ideal alignment with large- $\Delta\epsilon$ LC ($\Delta\epsilon > 5$) is much higher than that of low- $\Delta\epsilon$ LC. alignment. This emphasizes the need for better impurity/humidity control method to support large- $\Delta\epsilon$ LC for high output power enhancement.

3.6.2 Viscous Energy Loss.

The introduction of any permittivity fluids, other than air, into the dielectric gap would lead to the increase of shear viscous force F_μ ; i.e., the increase in energy dissipation due to viscous damping from LC. According to the investigation done by Belyaev [90], as shown in Figure 3.26, average viscosity $\bar{\mu}$ of LC can be approximated by its anisotropic permittivity $\Delta\epsilon$ as in the following;

$$\bar{\mu}(\Delta\epsilon) = 16.07 + 1.67\Delta\epsilon \quad (3.13)$$

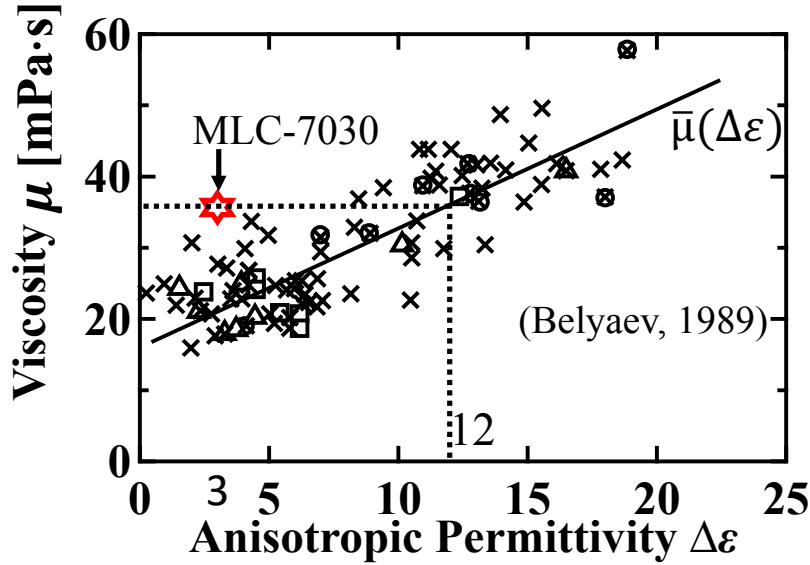


Figure 3.26 Measured viscosity of nematic liquid crystals as a function of anisotropic permittivity. [90] Black solid line is the fit of average viscosity to anisotropic permittivity. Black dash line projected the viscosity of MLC-7030 to the equivalent anisotropic permittivity according to fit line.

Then, the equation of shear viscous force will be;

$$F_{\mu} = \frac{\mu A}{g} \dot{x} = \frac{(16.07 + 1.67\Delta\epsilon)A_t}{g} \dot{x} \quad (3.14)$$

where μ , A_t , and, \dot{x} are fluid's viscosity, total area of electrodes and, velocity of rotor.

To estimate the effect of energy loss from viscosity, the ratio between electrostatic damping force F_e and shear viscous force F_{μ} , which is equivalent to the ratio of output power and viscous energy loss, is made under the assumption of negligible damping effect on mechanical motion of harvester due to sufficiently strong input; i.e. constant rotational velocity on each conditions. For the ease of calculation, root-mean-square of output voltage V_{rms} is utilized for calculation of F_e as shown in the following;

$$F_e = \alpha_e V_{rms} \quad (3.15)$$

where $\alpha_e = (\epsilon_0 \epsilon_1 \epsilon_e \epsilon_p n l V_{surf}) / (t_p \epsilon_1 \epsilon_e + t_e \epsilon_1 \epsilon_p + g \epsilon_e \epsilon_p)$. n is number of electrode pairs and l is length of the electrode.

Dividing eq.(3.15) with eq.(3.14), we will get;

$$\frac{F_e}{F_{\mu}} = \frac{\epsilon_0 \epsilon_1 \epsilon_e \epsilon_p n l V_{surf} V_{rms}}{t_p \epsilon_1 \epsilon_e + t_e \epsilon_1 \epsilon_p + g \epsilon_e \epsilon_p} \times \frac{g}{(16.07 + 1.67\Delta\epsilon)A_t \dot{x}} \quad (3.16)$$

Chapter 3 Liquid Crystal Alignment Measurement and Development of Generator Model

Since each interdigitated electrode fingers in rotational electret vibration energy harvester is in trapezoid shape, A_t equals to $0.5nl\theta_s(r + R)$; where θ_s , r and, R are width angle of each finger, inner radius and, outer radius of the generator. Thus, eq.(3.16) will become;

$$\frac{F_e}{F_v} = \frac{nl}{g} \left(\frac{\epsilon_0 \epsilon_1 \epsilon_e \epsilon_p V_{surf} V_{rms}}{\frac{t_p}{g} \epsilon_1 \epsilon_e + \frac{t_e}{g} \epsilon_1 \epsilon_p + \epsilon_e \epsilon_p} \right) \times \frac{g}{nl} \left(\frac{1}{(16.07 + 1.67\Delta\epsilon)(r + R)\theta_s \dot{x}} \right)$$

Additionally, $t_p \ll g$; so, $\epsilon_1 \epsilon_e$ can be neglect. We will have

$$\frac{F_e}{F_v} = \left(\frac{\epsilon_0 \epsilon_1 \epsilon_e V_{surf} V_{rms}}{\frac{t_e}{g} \epsilon_1 + \epsilon_e} \right) \times \left(\frac{1}{(16.07 + 1.67\Delta\epsilon)(r + R)\theta_s \dot{x}} \right) \quad (3.17)$$

Parameters used in the estimation of eq. (3.17) are listed in Table 3.2. Figure 3.27 shows the comparison of eq.(3.17) with different V_{surf} and \dot{x} . It is found that the F_e/F_v ratio is decreased with the increasing rotational speed since F_e is independent of \dot{x} . On the other hand, F_e/F_v ratio is increased with the increasing of V_{surf} due to its dependency on both V_{surf} and V_{rms} . Based on the simulations, viscous loss is found to be minimal at the operating condition of low rotational velocity and high surface potential. It should also be noted that the increase of $\Delta\epsilon$ leads to larger F_e/F_v ratio, despite the increase of μ from $\Delta\epsilon$, due to stronger dependency of F_e to ϵ_1 and V_{rms} compared to that of F_v .

Based on properties of MLC-7030, at normal operating speed of rotational electret energy harvester at about 1.0 rps with V_{surf} of -1kV, F_e/F_v is 8.7. In other words, the estimated viscous loss from the application of MLC-7030 in rotational electret energy harvester is as small as 1/9 or 11% of the output power.

Table 3.2 Simulation parameters for estimation of viscous loss compared to output power.

Parameters	Value	Unit
Dielectric gap, g	100	μm
Thickness of electret, t_e	15	μm
Inner radius, r	9	mm
Output radius, R	19	mm
Width angle of electrode, θ_s	0.024	rad
Relative permittivity of electret, ϵ_e	2.1	-
Relative transverse permittivity, ϵ_\perp	3	-

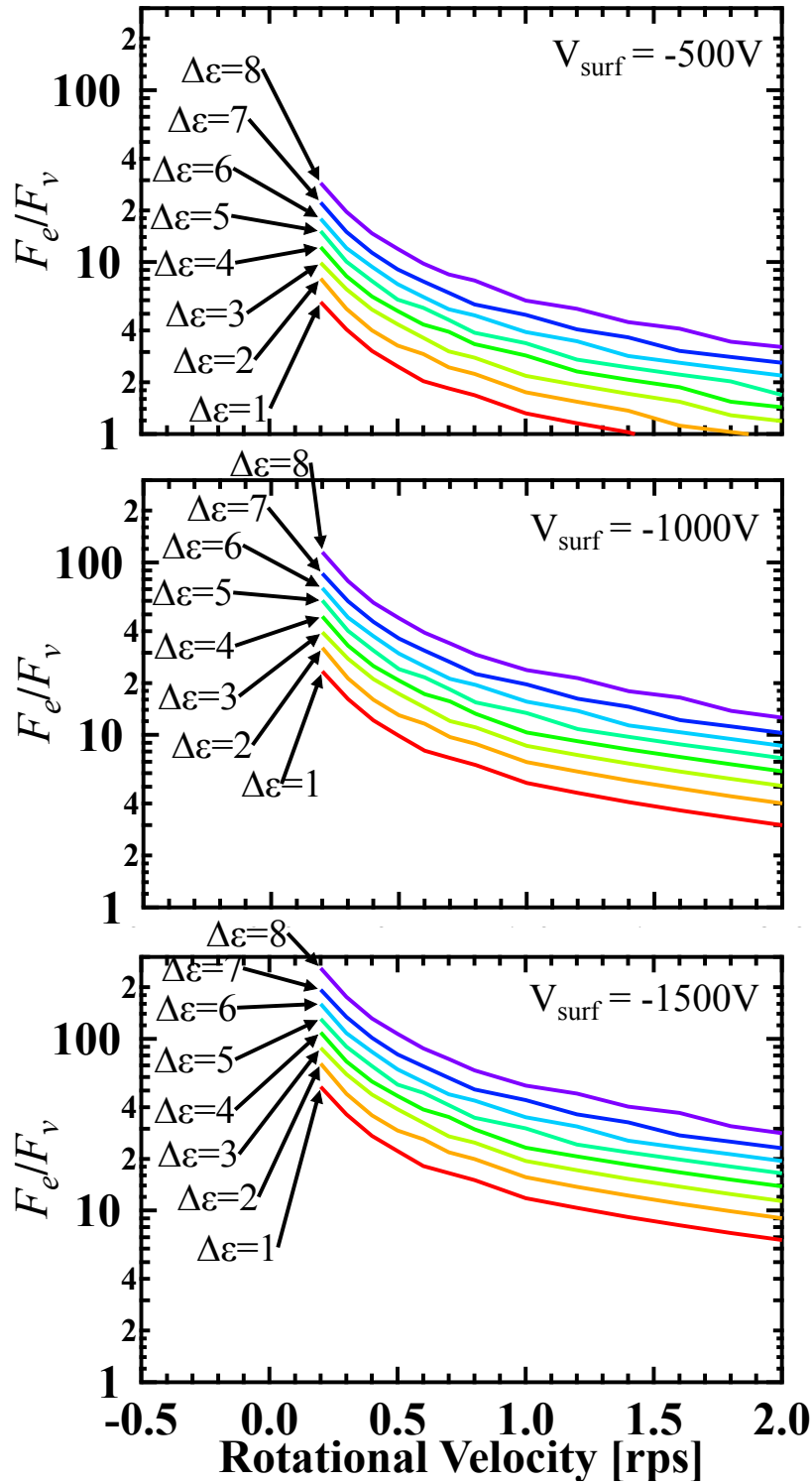


Figure 3.27 Ratio between electrostatic damping force and viscous damping force from different anisotropic permittivity fluids as a function of rotational velocity at varied surface potential.

Chapter 3 Liquid Crystal Alignment Measurement and Development of Generator Model

3.6.3 Figure of Merit for Permittivity Fluids.

For better comparison of the output power enhancement effects $P_{max}/P_{max,air}$ among different permittivity fluids, figure of merit (FoM) is defined as the normalization of net energy produced over the viscous loss from the fluids to that of air gap. It can be written as;

$$FoM = \frac{(F_e - F_v)_{fluid}}{(F_e - F_v)_{air}} \quad (3.18)$$

Using the same parameters as in Table 3.2 with surface potential of $-1kV_{surf.}$ and constant rotational velocity of 1.0 rps, FoM and output power enhancement ratio for different fluids are compared and shown in Figure 3.28. The estimation for isotropic liquids (black solid line) is made under the assumption of no viscous energy loss while the estimation for other named fluids is calculated with its viscosity from data sheet. For MLC-7030, its viscosity is $37 \text{ mPa} \cdot \text{s}$.

The upper limit of power enhancement and FoM of isotropic liquids are 16.5 and 10.5. For isotropic liquids, it is also found that power enhancement and FoM is decreased after increasing permittivity pass the optimal point of $\epsilon_r=20$. For MLC-7030 with present horizontal alignment layer, the power enhancement ratio and FoM reach about 17 and 14.4, respectively, which are higher than isotropic liquids. When ideal alignment of LC molecules at interdigital gap is realized, i.e. C_{p2} is minimized, the power enhancement ratio and FoM of MLC-7030 could reach as high as 45 and 31, respectively, which are significantly higher than any other isotropic liquids and itself in present horizontal alignment condition.

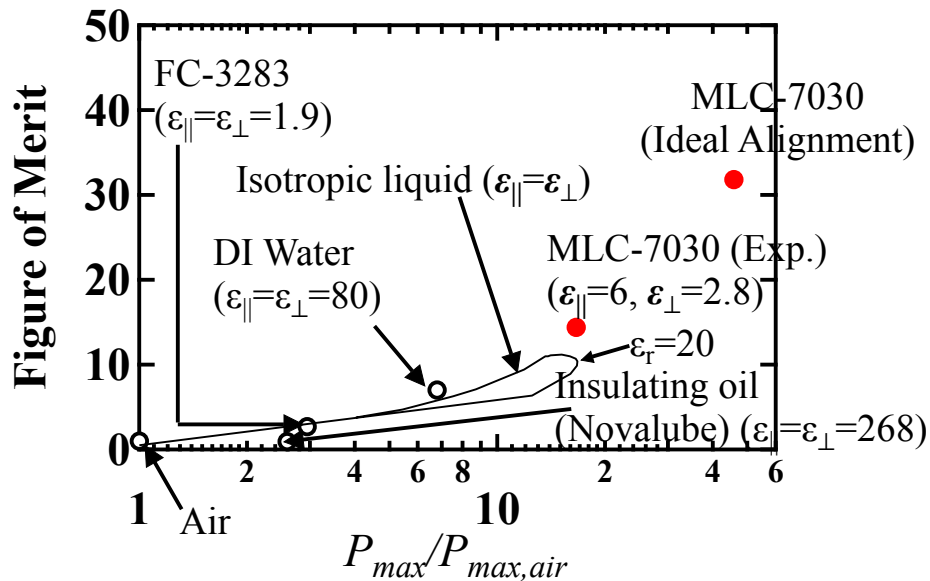


Figure 3.28 Comparison of FoM and power enhancement between different fluids.

Chapter 3 Liquid Crystal Alignment Measurement and Development of Generator Model

3.7 Chapter Summary

The summary of this chapter is as the following;

- (1) LC molecule alignment is observed with microscopic Fourier-Transform Infrared spectroscopy (FT-IR). It is founded that LC molecules aligned vertically under an area with strong electric field of $5.0 \text{ V}/\mu\text{m}$, and is gradually changing from vertical to horizontal alignment across interdigital gap to the grounded area. LC alignment change is estimated to start at about $100 \mu\text{m}$ from the edge, inside high electric field area. This indicates the strong effect from the fringe electric field between interdigitated electrodes.
- (2) Dynamic alignment measurement system for electret vibration energy harvester has been developed utilizing polarized optical microscopy (POM) equipped with high-speed camera. LC molecules are founded to be vertically aligned under the charged electret due to its strong electric field of over $10 \text{ V}/\mu\text{m}$. On the other hand, LC aligns horizontally in area with low electric field. During the operation, LC molecule alignment is found to be periodically changing. Additionally, strong electric field from charged electret has a dominant effect over the realignment of LC molecule at interdigital gap while it is unaffected by the unsteady electric field from output voltage.
- (3) Based on the experimental data of LC molecule alignment at the interdigital gap, parasitic capacitance from dielectric gap (C_{p1}) is founded to be periodically changed over time. Time-average value shows the larger-than-expected C_{p1} compared to the estimation using correlation model. Though larger, it will not affect the total C_p , since parasitic capacitance from substrate (C_{p2}) is dominant.
- (4) From the experimental data of time-dependent LC molecule alignment, 1-D electrostatic model of LC-enhanced electret vibration energy harvester with field-dependent permittivity and dynamic parasitic capacitance is developed. The model is in good agreement with experimental data.
- (5) Based on the present 1-D electrostatic model, performance prediction of LC-enhanced electret vibration energy harvester is made. The upper limit of output power enhancement is found to be 12 due to the maximum anisotropic permittivity for high resistivity over $10^{16} \Omega \cdot \text{cm}$ is 5.
- (6) Viscous damping and energy loss by LC is estimated using rotational electret energy harvester. The ratio between electrostatic damping force F_e and viscous damping force F_v , i.e. ratio of output power and viscous loss, is found to be decreasing with the increase of rotational speed. This is because F_e is independent on the speed while F_v is proportional to it. During normal operation with speed of 1 rps, F_e/F_v is 8.7 for $\Delta\epsilon$ of 3.2.
- (7) Figure of merit (FoM) is developed for comparing the enhancement effects of different permittivity fluids. For MLC-7030 with $\Delta\epsilon=3.2$, the power enhancement ratio and FoM are 17 and 14.4, respectively, which are much higher than isotropic liquids.

Chapter 4
Absorbance of Ion Impurity with
Ferroelectric Materials for Liquid-Crystal-
Enhanced Electret Vibration Energy
Harvester

Chapter 4 Absorbance of Ion Impurity with Ferroelectric Materials for Liquid-Crystal-Enhanced Electret Vibration Energy Harvester

4.1 Chapter introduction

This chapter aims to investigate the impurity control scheme for LC-enhanced electret vibration energy harvester. In this chapter, the impurity control for LC is discussed. Mainly, the impurity control through the use of ferroelectric material with LC. Long-term resistivity retention for LC with ferroelectric materials will be tested compared with metal oxide ones. Then, generator with ferroelectric material will be fabricated and the output power generation experiment will be performed with liquid crystal.

4.2 Impurity Control for Resistivity Retentions in Liquid Crystal

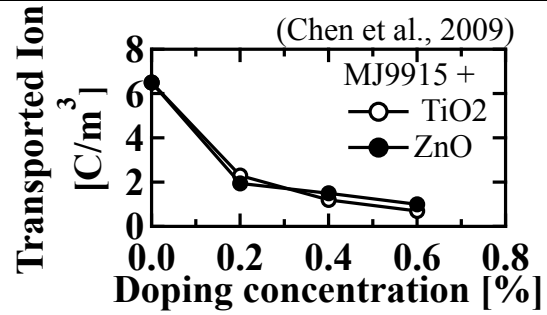
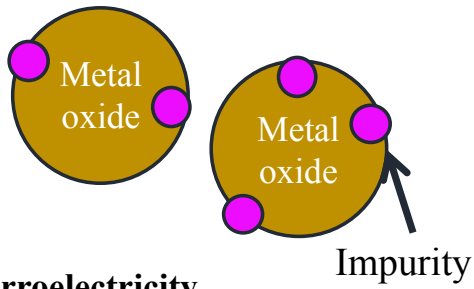
As demonstrated in chapter 2, high resistivity of LC is crucial for the realization of LC-enhanced electret vibration energy harvester. During the synthesizing process, LC has been purified many times with common purification techniques – recrystallization [91], distillation, selective solidification [92], and etc. – resulting in low impurity concentration. On the other hand, Huang et al. [87] has shown that ionic impurity concentration in LC is much higher after its contact with fabricated cells/containers/devices. Though this can be reduced with careful and cleaned fabrication process, slight contamination from the cleaned devices is inevitable which may lead to the change in electrical properties of LC overtime. There are many attempts to tackle such challenge. One method is to doped LC with micro/nano-sized particles [93] [94] [95] [96] [97]; but, the results is generally diverse depending on type of materials and concentration of dopant. With metal particles [94], instead of removing impurity, it becomes additional impurity in LC. While metal oxide particles show varied effects; increasing [95] [96] [98] and reducing [97] LC's resistivity. For metal oxide particles, the theory behind its impurity control is the utilization of chemisorption effect (surface effect), i.e. ion impurities are chemically/physically absorbed onto the surface of the particles. Chen et al. [98] demonstrated the reduction of transported ions, which equals to the increase of resistivity, in LC using of TiO_2 and ZnO , metal oxide nanoparticles as shown in Figure 4.1a.

On the other hands, ferroelectric materials, such as BaTiO_3 , display trapping capabilities for ionic impurities. Garbovskiy and Gluschenko [99] give reason that strong local electric field from remnant polarization of ferroelectric particles plays an important role in trapping the ion impurity as shown in Figure 4.1b. This leads to realization of high resistivity of LC. Despite the promising results, long-term resistivity retention of such dopants is uncertain and has never been reported, the same as that of metal oxide particles. This aspect of ferroelectric material as impurity control for LC will be tested and discussed later in the chapter 4.3.

Apart from doping LC with various materials, another impurity control method is the use of impurity trapping film. Hirai et al. [100] had proposed the use of porous polyimide resin film for trapping ionic impurity from LC in unit cell of liquid crystal display. However, the surface area of such unit cell is too small for any efficient impurity removal. Additionally, the absorption of polymer film is not that selective, such that, additives for LC and even LC molecule itself also got adsorbed; causing the overall degradation of LC. On the other hand, the immobile film is attractive due to simple and stable construct unlike complex doping process/interactions. The combination of ferroelectric material and thin film could benefit from both characteristics. This idea will be assessed in chapter 4.4.

Chapter 4 Absorbance of Ion Impurity with Ferroelectric Materials for Liquid-Crystal-Enhanced Electret Vibration Energy Harvester

(a) Chemisorption



(b) Ferroelectricity

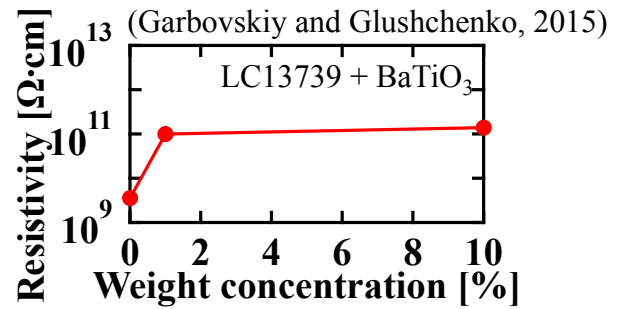
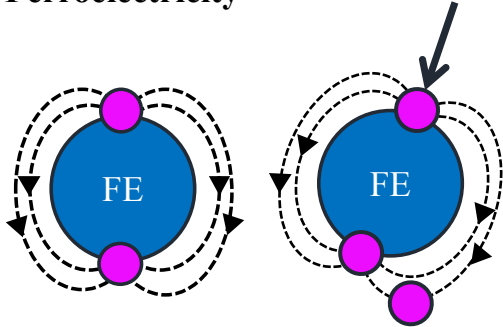


Figure 4.1 Schematic and examples of ion trapping mechanisms; (a) chemisorption and (b) ferroelectricity.

This part is withheld due to the conference publication schedule within 2021/12. Additionally, the findings are likely planned to be filed as a patent.

Chapter 5

Conclusions

Conclusions

This thesis presents the output power enhancement method for overlapping area change electret vibration energy harvester using nematic liquid crystal (LC) for the first time. By introducing anisotropic permittivity of LC into the gap between the electrets and counter electrodes, the capacitance change in response to the overlapping area change is boosted while limiting the increase of parasitic capacitance. The enhancement mechanisms have been investigated through LC alignment angle measurements. Use of ferroelectric materials is also proposed to absorb ion impurities and to keep high impedance of LC. The conclusions are summarized as follows:

- (1) The output power of electrostatic/electret vibration energy harvester is increased with the anisotropic permittivity of LC, and up to 90 times output power enhancement can be achieved if compared with a conventional energy harvester with the air gap. However, for the application to electret energy harvesters, the resistivity of LC should be higher than $10^{16} \Omega \cdot \text{cm}$ to avoid the electret discharge.
- (2) Due to the trade-off between anisotropic permittivity and resistivity of nematic LC, a commercial LC MLC-7030 with the anisotropic permittivity of 3.2 and the resistivity over $10^{16} \Omega \cdot \text{cm}$ has been chosen as the anisotropic permittivity liquid. It is found that the output power is increased by 7 times in the LC-enhanced electret vibration energy harvester compared to conventional air-in-the-gap energy harvester. By cleaning the device before use and by controlling humidity lower than 10 %RH, the enhanced output power can be kept for over 40 hours.
- (3) Molecule alignment of LC at the interdigitated electrodes is examined with microscopic FT-IR spectroscopy (FT-IR). It is found that LC molecules are vertically aligned under a strong electric field over $5.0 \text{ V}/\mu\text{m}$ and gradually changed from vertical to horizontal alignment across the interdigital gap into the grounded electrode area. The alignment change is estimated to start at about $100 \mu\text{m}$ from the edge of electrode inside the area with high electric field, indicating the strong effect from fringe electric field between interdigitated electrodes.
- (4) Time-resolved in-situ alignment angle measurement system for electret vibration energy harvester has been developed using a polarized optical microscope (POM) equipped with a high speed camera. It is found that, even with the LC motion induced by the in-plane vibration of the electrodes, the LC molecules are vertically aligned under the charged electret due to the high electric field strength over $10.0 \text{ V}/\mu\text{m}$. On the other hand, the LC molecules are horizontally aligned in the area with low electric field. During the operation, alignment at the interdigital gap is dynamically alternating and strongly affected by the strong electric field from charged electret while unaffected by the unsteady electric field from output voltage.
- (5) Based on the transient experimental data of LC molecule alignment, the parasitic capacitance of interdigital electrodes on the LC side is found to be periodically changed. Although its time-average value is larger than the estimate using a static model, it will not affect the total parasitic capacitance, since the parasitic capacitance on the substrate side is dominant.
- (6) Based on the experimental data of time-dependent LC molecule alignment, 1-D electrostatic model of LC-enhanced electret vibration energy harvester with field-dependent permittivity and dynamic parasitic capacitance is developed. It is found that the prediction with the present model is in good agreement with the experimental data.
- (7) Performance prediction of LC-enhanced electret vibration energy harvester is made by using the present 1-D electrostatic model. It is found that the upper limit of output power enhancement is 12, since the upper limit of $\Delta\epsilon$ for high resistivity over $10^{16} \Omega \cdot \text{cm}$ is 5.

(8) The viscous damping and energy loss by LC is estimated for a rotational electret energy harvester. The ratio between the electrostatic damping force F_e and the viscous damping force F_v , which is also the ratio of the output power and the viscous loss, is decreased with increasing rotational speed, since the electrostatic damping force is independent on the speed. At the normal operation speed of rotational electret energy harvester at around 1 rps, F_e/F_v is 8.7 for $\Delta\epsilon=3.2$. A figure of merit (FoM) is also defined for comparing the power enhancement effects of different liquids. For MLC-7030, the power enhancement ratio and FoM reach 17 and 14.4, respectively, which are much higher than any other isotropic liquids.

This conclusions from chapter 4 is withheld due to planned publication.

Chapter 6

References

References

- [1] S. Sutardja, "Slowing of Moore's law signals the beginning of smart everything," in *Solid State Device Research Conference (ESSDERC), 2014 44th European*, Venice, Italy, 2014.
- [2] "Internet of Things," Wikimedia Foundation, Inc., 25 January 2018. [Online]. Available: https://en.wikipedia.org/wiki/Internet_of_things. [Accessed 25 January 2018].
- [3] "MarketsandMarkets," MarketsandMarkets Research Private Ltd., 06 12 2019. [Online]. Available: <https://www.marketsandmarkets.com/Market-Reports/wireless-sensor-networks-market-445.html>. [Accessed 25 02 2021].
- [4] "Internet of Things," 14 November 2015. [Online]. Available: <https://www.electronicshub.org/internet-of-things/>. [Accessed 25 January 2018].
- [5] I. Buchmann, "Types of Lithium-ion," Cadex Electronics Inc., 15 November 2017. [Online]. Available: http://batteryuniversity.com/learn/article/types_of_lithium_ion. [Accessed 25 January 2018].
- [6] J. M. Tarascon and M. Armand, "Issues and challenges facing rechargeable lithium batteries," *Nature*, vol. 414, pp. 359-367, 15 November 2001.
- [7] Fujitsu Laboratories Ltd., "Fujitsu Develops Hybrid Energy Harvesting Device for Generating Electricity from Heat and Light," Fujitsu Laboratories Ltd., 9 December 2010. [Online]. Available: <http://www.fujitsu.com/global/about/resources/news/press-releases/2010/1209-01.html>. [Accessed 25 January 2018].
- [8] J. A. Paradiso and T. Starner, "Energy Scavenging for Mobile and Wireless Electronics," *IEEE Pervasive Computing*, vol. 4, no. 1, pp. 18-27, January 2005.
- [9] N. S. Haduk and G. G. Amatucci, "Small-scale energy harvesting through thermoelectric, vibration, and radiofrequency power conversion," *Journal of Applied Physics*, vol. 103, no. 10, pp. 1-24, 2008.
- [10] "Thermic," Seiko Holdings Corporation, [Online]. Available: https://museum.seiko.co.jp/en/collections/clock_watch/category3/collect041.html. [Accessed 25 January 2018].
- [11] S. Roundy, P. K. Wright and J. Rabaey, "A study of low level vibrations as a power source for wireless sensor nodes," *Computer Communications*, vol. 26, no. 11, pp. 1131-1144, 1 July 2003.
- [12] C. B. Williams and R. B. Yates, "Analysis of a micro-electric generator for microsystems," *Sensors and Actuators A: Physical*, vol. 52, no. 1-3, pp. 8-11, March 1996.
- [13] R. Amirtharajah and A. P. Chandrakasan, "Self-powered signal processing using vibration-based power generation," *Journal of Solid-State Circuits*, vol. 33, no. 5, pp. 687-695, May 1998.
- [14] C. B. Williams, C. Shearwood, M. A. Harradine, P. H. Mellor, T. S. Birch and R. B. Yates, "Development of an electromagnetic micro-generator," *IEE Proceedings - Circuits, Devices and Systems*, vol. 148, no. 6, pp. 337-342, December 2001.
- [15] L. Wang and F. G. Yuan, "Energy harvesting by magnetostrictive material (MsM) for powering wireless sensors in SHM," in *SPIE Smart Structures and Materials & NDE and Health Monitoring, 14th International Symposium (SSN07)*, 2007.

-
- [16] C. T. Pan and T. T. Wu, "Development of a rotary electromagnetic microgenerator," *Journal of Micromechanics and Microengineering*, vol. 17, no. 1, pp. 120-128, December 2006.
- [17] D. P. Arnold, "Review of microscale magnetic power generation," *IEEE Transactions on Magnetics*, vol. 43, no. 11, pp. 3940-3951, 2007.
- [18] S. Das, D. P. Arnold, I. Zana, J.-W. Park, M. G. Allen and J. Lang, "Microfabricated high-speed axial-flux multiwatt permanent-magnet generators-part I: modeling," *Journal of Microelectromechanical Systems*, vol. 15, no. 5, pp. 1330-1350, 2006.
- [19] P. S. Dineva, D. Gross, R. Muller and T. Rangelov, "Chapter 2 Piezoelectric Materials," in *Dynamic fracture of piezoelectric materials*, Springer International Publishing, 2014, pp. 7-32.
- [20] S. Roundy and P. K. Wright, "A piezoelectric vibration based generator for wireless electronics," *Smart Materials and Structures*, vol. 13, no. 5, pp. 1131-1142, 2004.
- [21] Y. B. Jeon, R. Sood, J.-H. Jeong and S.-G. Kim, "MEMS power generator with transverse mode thin film PZT," *Sensors and Actuators A: Physical*, vol. 122, no. 19, pp. 16-22, July 2005.
- [22] N. S. Shenck and J. A. Paradiso, "Energy scavenging with shoe-mounted piezoelectrics," *IEEE Micro*, vol. 21, no. 3, pp. 30-42, 2001.
- [23] Y. H. Liu, Y. Huang, R. Tang and B. Wang, "Application of interdigital capacitive sensors for detecting power cable insulation damage," in *2015 IEEE International Conference on Mechatronics and Automation*, Beijing, China, 2015.
- [24] K. Chetpattanaonondh, T. Tapoanoi, P. Phukpattaranont and N. Jindapetch, "A self-calibration water level measurement using an interdigital capacitive sensor," *Sensors and Actuators A: Physical*, vol. 209, no. 1, pp. 175-182, March 2014.
- [25] V. Tsouti, C. Boutopoulos, I. Zergioti and S. Chauzandroulis, "Capacitive microsystems for biological sensing," *Biosensors and Bioelectronics*, vol. 27, no. 1, pp. 1-11, 2011.
- [26] H. Philipp, "Capacitive sensor and array". USA Patent US6452514 B1, 17 September 2002.
- [27] J. Boland, Y. H. Chao, Y. Suzuki and Y. C. Tai, "Micro electret power generator," in *IEEE The 16th Annual International Conference on Micro Electro Mechanical Systems (MEMS'03)*, Kyoto, Japan, 2003.
- [28] H. W. Lo and Y. C. Tai, "Parylene-based electret power generators," *Journal of Micromechanics and Microengineering*, vol. 18, no. 10, pp. 1-8, 2008.
- [29] P. Basset, D. Galayko, A. M. Paracha, F. Marty, A. Dudka and T. Bourouina, "A batch-fabricated and electret-free silicon electrostatic vibration energy harvester," *Journal of Micromechanics and Microengineering*, vol. 19, no. 11, pp. 1-12, 2009.
- [30] D. Hoffmann, B. Folkmer and Y. Manoli, "Fabrication, characterization and modelling of electrostatic micro-generators," *Journal of Micromechanics and Microengineering*, vol. 19, no. 9, pp. 1-11, 2009.
- [31] U. Bartsch, J. Gaspar and O. Paul, "Low-frequency two-dimensional resonators for vibrational micro energy harvesting," *Journal of Micromechanics and Microengineering*, vol. 20, no. 3, pp. 1-12, 2010.

-
- [32] Y. Suzuki, "Recent progress in MEMS electret generator for energy harvesting," *Special Issue on Smart Technologies in Sensors and MEMS*, vol. 6, no. 2, pp. 101-111, 2-11.
 - [33] S. Gray, *Philosophical Transactions of the Royal Society of London*, vol. 37, no. 285, 1732.
 - [34] G. Sesler, *Electrets* 3rd edition, Morgan Hill (CA): Laplacian Press, 1998.
 - [35] M. Suzuki, T. Takahashi and S. Aoyagi, "Development of a high-performance fluoropolymer electret mixed with nano-particles and its application to vibration energy harvesting," *Journal of Physics: Conference Series*, vol. 557, pp. 1-5, 2014.
 - [36] O. Heaviside, *Electrical papers*, London: Macmillan and Co., 1892.
 - [37] M. Eguchi, "XX. On the permanent electret," *The London, Edinburgh, and Dublin Philosophical Magazine and Journal of Science*, vol. 49, no. 289, pp. 178-192, 1925.
 - [38] A. Sprengels, W. Olthuis and P. Brveld, "The application of silicon dioxide as an electret material," in *6th International Symposium on Electrets (ISE 6)*, Oxford, UK, 1988.
 - [39] K. Yamashita, N. Oikawa and T. Umegaki, "Acceleration and Deceleration of Bone-Like Crystal Growth on Ceramic Hydroxyapatite by Electric Poling," *Chemistry of Materials*, vol. 8, no. 12, p. 2697-2700, 1996.
 - [40] Y. Sakane, Y. Suzuki and N. Kasagi, "The development of a high-performance perfluorinated polymer electret and its application to micro power generation," *JOURNAL OF MICROMECHANICS AND MICROENGINEERING*, vol. 18, no. 10, pp. 1-6, 2008.
 - [41] H. Kawai, "The Piezoelectricity of Poly (vinylidene Fluoride)," *Japanese Journal of Applied Physics*, vol. 8, pp. 975-976, 1969.
 - [42] S. Kim, K. Suzuki, A. Sugie, H. Yoshida, M. Yoshida and Y. Suzuki, "Effect of end group of amorphous perfluoro-polymer electrets on electron trapping," *Science and Technology of Advanced Materials*, vol. 19, pp. 486-494, 2018.
 - [43] S. Kim, K. Suzuki and Y. Suzuki, "Development of A High-performance Amorphous Fluorinated Polymer Electret Based on Quantum Chemical Analysis," in *18th International Conference on Micro and Nanotechnology for Power Generation and Energy Conversion Applications (PowerMEMS18)*, Florida, USA, 2018.
 - [44] S. Kim, A. Melnyk, D. Andrienko and Y. Suzuki, "Solid-State Electron Affinity Analysis of Amorphous Fluorinated Polymer Electret," *The Journal of Physical Chemistry B*, vol. 124, no. 46, p. 10507-10513, 2020.
 - [45] Y. Zhang, J. Zhang, K. Suzuki, M. Sumita, K. Terayama, J. Li, Z. Mao, K. Tsuda and Y. Suzuki, "Discovery of polymer electret material via de novo molecule generation and functional group enrichment analysis," *Applied Physics Letters*, vol. 118, no. 22, pp. 1-4, 2021.
 - [46] O. D. Jefimenko and D. K. Walker, "Electrostatic Current Generator Having a Disk Electret as an Active Element," *IEEE Transactions on Industry Applications*, Vols. IA-14, no. 6, pp. 537-539, 1978.
 - [47] Y. Tada, "Experimental Characteristics of Electret Generator, Using Polymer Film Electrets," *Japanese Journal of Applied Physics*, vol. 1, no. 3, pp. 846-851, 1992.
 - [48] K. Matsumoto, K. Saruwatari and Y. Suzuki, "Vibration-powered Battery-less Sensor Node Using MEMS Electret Generator," in *11th Int. Workshop on Micro and*

- [49] T. Miyoshi, M. Adachi, K. Suzuki, Y. Liu and Y. Suzuki, "Low-profile rotational electret generator using print circuit board for energy harvesting from arm swing," in *IEEE international conference on micro electro mechanical systems (MEMS)*, Belfast, UK, 2018.
- [50] A. M. Paracha, P. Basset, F. Marty, A. V. Chasin, P. Poulichet and T. Bourouina, "A high power density electrostatic vibration-to-electric energy converted based on an in-plane overlapping plate (IPOP) mechanism," in *Dans Symposium on Design, Test, Integration and Packaging of MEMS/MOEMS - DTIP 2007*, Stresa, Iago Maggiore, Italy, 2007.
- [51] F. Wang and O. Hansen, "Electrostatic energy harvesting device with out-of-the-plane gap closing scheme," in *Solid-State Sensors, Actuators and Microsystems (TRANSDUCERS & EUROSENSORS XXVII), 2013 Transducers & Eurosensors XXVII: The 17th International Conference on*, Barcelona, Spain, 2013.
- [52] Y. Feng, Z. J. Yu and Y. H. H, "High-performance gap-closing vibrational energy harvesting using electret-polarized dielectric oscillators," *Applied Physics Letters*, vol. 112, pp. 1-4, 2018.
- [53] Q. Fu and Y. Suzuki, "Large-dynamic-range MEMS electret energy harvester with combined gap-closing/overlapping-area-change electrodes," *Journal of Physics: Conference Series*, vol. 476, pp. 1-5, 2013.
- [54] L. Bu, H. Y. Xu, B. J. Xu and L. Song, "Micro-fabricated liquid encapsulated energy harvester with polymer barrier layer as liquid electret interface," *Journal of Physics: Conference Series*, vol. 557, 2014.
- [55] D. H. Huynh, T. C. Nguyen, P. D. Nguyen, C. D. Abeyrathne, M. S. Hossain, R. Evans and E. Skafidas, "Environmentally friendly power generator based on moving liquid dielectric and double layer effect," *Scientific Reports*, vol. 6, 2016.
- [56] T. Takahashi, M. Suzuki, T. Hirata, N. Matsushita, R. Yoneya, J. Onishi, T. Nishida, Y. Yoshikawa and S. Aoyagi, "Electret energy harvesting based on fringe electrical field change inside trenched ferroelectric," in *The 24th International Conference on Micro Electro Mechanical Systems MEMS 2011*, Cancun, Mexico, 2011.
- [57] M. Adachi, K. Suzuki and Y. Suzuki, "Development of rotational electret energy harvester using print circuit board," in *The 17th International Conference on Micro and Nanotechnology for Power Generation and Energy Conversion Applications*, Kanazawa, Japan, 2017.
- [58] U. Bartsch, C. Sander, M. Blattmann, J. Gaspar and O. Paul, "Influence on parasitic capacitances on the power output of electret-based energy harvesting generators," in *The 9th International Workshop on Micro and Nanotechnology for Power Generation and Energy Conversion Applications (PowerMEMS 2009)*, Washington DC, USA, 2009.
- [59] C. T. A. Johnk, *Engineering electromagnetics field and waves*, New York: John Wileys and Sons, 1975.
- [60] C. S. Walker, *Capacitance, inductance, and crosstalk analysis*, London: Artech House Publishing, 1990.

-
- [61] R. Igreja and C. J. Dias, "Analytical evaluation of the interdigital electrodes capacitance for a multi-layered structure," *Sensors and Actuators A*, vol. 112, pp. 291-301, 2004.
 - [62] R. Igreja and C. J. Dias, "Extension to the analytical model of the interdigital electrodes capacitance for a multi-layered structure," *Sensors and Actuators A: Physical*, vol. 172, pp. 392-399, 2011.
 - [63] T. Masaki, N. Yoshitake, S. Kamiyama, M. Nabeto, T. Seki, M. Oba and D. Uchida, "Multi-frequency vibration-driven electret generator for wireless sensor applications," *Journal of Physics: Conference Series*, vol. 557, 2014.
 - [64] R. Chen and Y. Suzuki, "Suspended electrodes for reducing parasitic capacitance in electret energy harvesters," *Journal of Micromechanics and Microengineering*, vol. 23, 2013.
 - [65] J. Boland, J. Messenger, K. Lo and Y. Tai, "Arrayed liquid rotor electret power generator systems," in *18th IEEE International Conference on Micro Electro Mechanical Systems, 2005 (MEMS 2005)*, Miami Beach, FL, USA, 2005.
 - [66] S. Inoue, T. Takahashi, M. Kumemura, H. Fujita and H. Toshiyoshi, "An implantable fluidic vibrational energy harvester," *Journal of Physics: Conference Series*, vol. 773, pp. 1-2, 2016.
 - [67] Y.-F. Chen, S. Inoue and H. Toshiyoshi, "An Electret-based Implantable Energy Harvester with Liquid Cells (MEMS vs. 3D Printing Fabrication)," *IEEJ Transactions on Sensors and Micromachines*, vol. 9, pp. 401-405, 2018.
 - [68] L. Bu, X. Wu, X. Wang and L. Liu, "Liquid encapsulated electrostatic energy harvester for low-frequency vibrations," *Journal of Intelligent Material Systems and Structures*, vol. 24, no. 1, pp. 61-69, 2012.
 - [69] W. J. Merz, "The Electrical and Optical Behavior of BaTiO₃ Single-Domain Crystals," *Physical Reviews*, vol. 76, no. 8, pp. 1221-1225, 1949.
 - [70] L. Jorat, A. Sibli, M. F. Blanc-Migon and G. Noyel, "Dielectric Anisotropy of the Magnetic Fluid Cobalt Ferrite in Dibutylphthalate," *IEEE Transactions on Dielectrics and Electrical Insulation*, vol. 1, no. 3, pp. 365-370, 1994.
 - [71] T. Kato, Y. Hirai, S. Nakaso and M. Moriyama, "Liquid-crystalline physical gels," *Chemical Society Reviews*, vol. 36, no. 12, pp. 1845-2128, 2007.
 - [72] P. Kumar, S. W. Kang and S. H. Lee, "Advanced bistable cholesteric light shutter with dual frequency nematic liquid crystal," *Optical Materials Express*, vol. 2, no. 8, pp. 1121-1134, 2012.
 - [73] B. Senyuk, "Anisotropy in liquid crystals," [Online]. [Accessed 25 January 2018].
 - [74] G. W. Gray, "Reminiscences from a life with liquid crystals," *Liquid Crystals*, vol. 24, no. 1, pp. 5-13, 1998.
 - [75] B. R. Ratna and R. Shashidhar, "Dielectric properties of 4'-n-alkyl-4-cyanobiphenyls in their nematic phases," *Pramana*, vol. 6, no. 5, pp. 278-283, 1976.
 - [76] M. Hard, "Fluorinated liquid crystal - properties and applications," *Chemical Societies Reviews*, vol. 36, pp. 2070-2095, 2007.
 - [77] R. Kirsch, "Fluorine in liquid crystal design for display applications," *Journal of Fluorine Chemistry*, vol. 177, pp. 29-36, 2015.

-
- [78] F. Benabed, T. Seghier, S. Boudraa and A. Seghiour, "Dielectric proprieties and relaxation behavior of Polyimide films (PI)," in *Electrical Sciences and Technologies in Maghreb (CISTEM), 2014 International Conference on*, Tunis, Tunisia, 2014.
 - [79] S. Murakami and H. Naito, "Charge injection and generation in nematic liquid crystal cells," *Japanese Journal of Applied Physics*, vol. 36, no. 2, pp. 773-776, 1997.
 - [80] H. Mada and M. Ryuzaki, "Ion influence on nematic liquid crystal cell impedance at low frequency," *Japanese Journal of Applied Physics*, vol. 34, pp. 1134-1136, 1995.
 - [81] Y. Tada, "Theoretical characteristics of generalized electret generator, using polymer films electret," *IEEE Transactions on Electrical Insulation*, Vols. EI-21, no. 3, pp. 457-464, 1986.
 - [82] T. Tsutsumino, Y. Suzuki, N. Kasagi and Y. Sakane, "Seismic power generator using high-performance polymer electret," in *Micro Electro Mechanical Systems (MEMS2006), 19th IEEE International Conference on*, Istanbul, Turkey, 2006.
 - [83] F. Wang and O. Hansen, "Inorganic electret with enhanced charge stability for energy harvesting," in *The 8th Annual IEEE International Conference on Nano/Micro Engineered and Molecular Systems*, Suzhou, China, 2013.
 - [84] T. Wu, Y. Suzuki, N. Kasagi and K. Kashiwaki, "Oil droplet manipulation using liquid dielectrophoresis on electret with superlyophobic surfaces," in *2010 IEEE 23rd International Conference on Micro Electro Mechanical Systems (MEMS)*, Hong Kong, China, 2010.
 - [85] D. Demus, Y. Goto, S. Sawada, E. Nakagawa, H. Saito and R. Tarao, "Trifluorinated Liquid Crystals for TFT Displays," *Molecular Crystals and Liquid Crystals Science and Technology. Section A. Molecular Crystals and Liquid Crystals*, vol. 260, no. 1, pp. 1-21, 1995.
 - [86] S. Gauza, J. Li, S.-T. Wu, A. Spaldo, R. Da browski, Y.-N. Tzeng and K.-L. Cheng, "High birefringence and high resistivity isothiocyanate-based nematic liquid crystal mixtures," *Liquid Crystals*, vol. 32, no. 8, pp. 1077-1085, 2005.
 - [87] H.-Y. Hung, C.-W. Lu, C.-Y. Lee, C.-S. Hsu and Y.-Z. Hsieh, "Analysis of metal ion impurities in liquid crystals using high resolution inductively coupled plasma mass spectrometry," *Analytical Methods*, vol. 4, pp. 3631-3637, 2012.
 - [88] K. Hagiwara, M. Honzumi, T. Tajima, Y. Yasuno, H. Kodama, K. Kidokoro, K. Kashiwagi and Y. Suzuki, "NOVEL THROUGH-SUBSTRATE CHARGING METHOD FOR ELECTRET GENERATOR USING SOFT X-RAY IRRADIATION," in *9th Int. Workshop on Micro and Nanotechnology for Power Generation and Energy Conversion Applications (PowerMEMS 2009)*, Washington DC, USA, 2009.
 - [89] Q. Wang, S. He, F. Yu and N. Huang, "Iterative finite-difference method for calculating the distribution of a liquid-crystal director," *Optical Engineering*, vol. 40, no. 11, pp. 2552-2557, 2001.
 - [90] V. V. Belyaev, "The viscosity of nematic liquid crystals," *Russian Chemical Reviews*, vol. 58, no. 10, pp. 917-947, 1989.
 - [91] 赵. 袁. 张. 詹. 王玉琴, "Purification method of liquid crystal intermediate 3,4,5-trifluoro phenol". China Patent CN102108044B, 25 09 2013.

-
- [92] 梁. 张. 张. 唐洪, "Liquid crystal purifying method". China Patent CN1775908A, 24 05 2006.
 - [93] Y. Garbovskiy and I. Glushchenko, "Nano-Objects and Ions in Liquid Crystals: Ion Trapping Effect and Related Phenomena," *Crystals*, vol. 5, pp. 501-533, 2015.
 - [94] S. Sridevi, S. Prasad, G. Nair, V. D'Britto and B. Prasad, "Enhancement of anisotropic conductivity, elastic, and dielectric constants in a liquid crystal-gold nanorod system," *Applied Physics Letter*, vol. 97, 2010.
 - [95] T. Joshi, J. Prakash, A. Kumar, J. Gangwar, A. Srivastava, S. Singh and A. Biradar, "Alumina nanoparticles find an application to reduce the ionic effects of ferroelectric liquid crystal," *Journal of Physical D: Applied Physics*, vol. 44, 2011.
 - [96] S. Gupta, D. Singh and R. Manohar, "Electrical and polarization behaviour of titania nanoparticles doped ferroelectric liquid crystal.," *Advanced Material Letter*, vol. 6, pp. 68-72, 2015.
 - [97] S. Supreet, K. Kumar and R. P. Raina, "Enhanced stability of the columnar matrix in a discotic liquid crystal by insertion of ZnO nanoparticles," *Liquid Crystals*, vol. 40, pp. 228-236, 2013.
 - [98] W.-T. Chen, P.-S. Chen and C.-Y. Chao, "Effect of Insulating Nanoparticles Doping on Electro-Optical Characteristics in Nematic Liquid Crystal Cells," *Molecular Crystals and Liquid Crystals*, vol. 507, no. 1, pp. 253-263, 2009.
 - [99] Y. Garbovskiy and I. Gluschenko, "Ion trapping by means of ferroelectric nanoparticles, and the quantification of this process in liquid crystals," *Appl. Phys. Lett.*, vol. 107, pp. 1-5, 2015.
 - [100] O. Hirai, N. Tashiro, O. Watanabe, H. Nishizawa and K. Suzuki, "Purification of liquid crystals and liquid crystal composition". United States Patent US5422034A, 6 6 1995.

List of Publications/Conferences

- 1) “Liquid-Crystal-Enhanced Electrostatic Vibration Generator, ”
K. Kittipaisalsilpa, T. Kato and, Y. Suzuki,
29th IEEE International Conference on Micro Electro Mechanical Systems (MEMS’16),
Shanghai, pp. 37-40, (2016).
- 2) “Modelling of Liquid-Crystal-Enhanced Electrostatic Vibration Generator, ”
K. Kittipaisalsilpa, T. Kato and, Y. Suzuki,
International Symposium on Micro-Nano Science and Technology (MNST2016), Tokyo,
pp.19, (2016).
- 3) “Characterization of Fluorinated Nematic Liquid Crystal for High-Power Electrostatic
Energy Harvester, ”
K. Kittipaisalsilpa, T. Kato and, Y. Suzuki,
17th International Conference on Micro and Nanotechnology for Power Generation and
Energy Conversion Applications (PowerMEMS’17), Kanazawa, pp.202-205, (2017).
- 4) “Effect of Impurity/Humidity on Liquid-Crystal-Enhanced Electret Vibration Energy
Harvester, ”
K. Kittipaisalsilpa, T. Kato and, Y. Suzuki,
19th International Workshop on Micro and Nanotechnology for Power Generation and
Energy Conversion Applications (PowerMEMS 2019), Krakow, T4-B2 (2019).
- 5) “Measurement of Molecule Alignment in Liquid-Crystal-Enhanced Electret Vibration
Energy Harvester, ”
K. Kittipaisalsilpa, T. Miyoshi, T. Kato and, Y. Suzuki,
日本機械学会熱工学コンファレンス 2020, オンライン, C134 (2020).
- 6) “ALD-Deposited Film for Impurity Control in Liquid-Crystal-Enhanced Electret Vibration
Energy Harvester, ”
K. Kittipaisalsilpa, T. Kato and, Y. Suzuki,
日本機械学会熱工学コンファレンス 2021, オンライン, (2021). (TBA)

Appendix

Appendix A

This part explains the fabrication steps of interdigitated electrodes for output power generation experiments and interdigitated electrodes for IR absorbance measurement in details.

Recipe for Fabrication Interdigital Electrodes on TEMPAX Glass Wafer(TPX-525μm)

Order	Process	Equipment	Chemical	Recipe
(a)	HF Cleaning			
a-1	HF Cleaning	Plastic Tray(HF)	0.5%HF	~30sec.
a-2	Water Cleaning	Plastic Tray(Water acid1)		
a-3	Water Cleaning	Plastic Tray(Water acid2)		
(b)	Dehydration			
b-1	Spin Drying	Spin Dryer		~1-2 min.
b-2	Oven Drying	Upper Oven		180°C, 15-20 min.
(c)	Sputtering 1			
c-1	Vacuuming	Sputter Machine		to less than 10 ⁻³
c-2	Pre-sputtering	Sputter Machine		Target 1 (Cr), 50W for 5min.
c-3	Sputtering	Sputter Machine		Target 1 (Cr), 300W for 2 min; 50nm
(d)	Sputtering 2			
d-1	Vacuuming	Sputter Machine		to less than 10 ⁻³
d-2	Pre-sputtering	Sputter Machine		Target 2 (Au), 50W for 5min.
d-3	Sputtering	Sputter Machine		Target 2 (Au), 300W for 2 min 10-20 sec; 200nm
(e)	Adhesion Enhancement			
e-1	Inserting	HDMS Metal Box		Put the wafer into HDMS Metal Box
e-2	Enhancing		HDMS	Pour HDMS(1 Plastic pipet [~1ml]), Close the lid
e-3	Enhancing (2)			Wait for 2 min.
(f)	PR Coating			
f-1	Spin Coating	Spin Coater	AZP4400	Recipe 0; result in 3.8nm-thick PR
(g)	Soft Bake			
g-1	Soft Bake	Oven		100°C, 20 min.
(h)	Photolithography			
h-1	Mask Set Up	Mask Aligner		Set up the Mask on the stage(1)
h-2	Parameter Set Up	Mask Aligner		Contact: Hard, Exposure Time: 3.8sec
h-3	Wafer Set Up	Mask Aligner		Set the Wafer on the stage(2)
h-4	UV Exposure	Mask Aligner		Expose the UV light
(i)	Developing			
i-1	PR Developing		Developer AZ 400K	~90-110 sec.
i-2	Water Cleaning			
i-3	Water Cleaning			
(j)	Drying			
j-1	Spin Drying	Spin Dryer		~1-2 min.
(k)	Residual Removing			
k-1	Vacuuming	RIE		Put the Wafer into the RIE chamber
k-2	Descuuming	RIE		Recipe 1; RF 50W for 1 min. with 30sccmO ₂

(l)	Metal Etching(1)			
l-1	Gold Etching	Glass Tray (Au Etchant)	Au Etchant	~9-10 min.
l-2	Water Cleaning	Glass Tray(1)		
l-3	Water Cleaning	Glass Tray(2)		
(m)	Drying			
m-1	Spin Drying	Spin Dryer		~1-2 min.
(n)	Metal Etching(2)			
n-1	Chromium Etching	Plastic Tray (Cr Etchant)	Cr Etchant	~20-25 sec.
n-2	Water Cleaning	Plastic Tray(1)		
n-3	Water Cleaning	Plastic Tray(2)		
(o)	PR Removing			
o-1	PR Removing	Glass Tray(Remover)	Remover 700	>5 min.
o-2	IPA Cleaning	Glass Tray(IPA)	IPA	
o-3	Water Cleaning	Glass Tray(Water)		
(p)	Drying			
p-1	Spin Drying	Spin Dryer		~1-2 min.
(q)	Residual Removing			
q-1	Vacuuming	RIE		Put the Wafer into the RIE chamber
q-2	Ashing	RIE		Recipe 2; RF 100W for 5 min. with 30sccmO ₂
(r)	Dehydration			
r-1	Dehydration	Upper Oven		120°C, 10 min.
(s)	Resistance Checking			
s-1	Resistance Checking	Multimeter/Agilent 6.5Digit Multimeter		>100MΩ, okay; >1GΩ, Good
(t)	PR Coating			
t-1	Spin Coating	Spin Coater	AZP4400	Recipe 0; result in 3.8nm-thick PR
(u)	Soft Bake			
u-1	Soft Bake	Oven		100°C, 20 min.
(v)	Dicing			
v-1	Prepare Wafer			Prepare the Wafer on the heating stage (50°C)
v-2	Set the Wafer	Dicing SAW, DAD-340		Set the Wafer onto the magnetic stage
v-3	Set the Parameter	Dicing SAW, DAD-340		Blade Type: AAA; Blade Height: 0.3/0.15
v-4	Dicing	Dicing SAW, DAD-340		#dicing's cut depends on 2*(#chip+1) per direction
(w)	PR Removing			
w-1	PR Removing	Glass Tray(Remover)	Remover 700	>5 min.
w-2	IPA Cleaning	Glass Tray(IPA)	IPA	
w-3	Water Cleaning	Glass Tray(Water)		

(x)	Residual Removing			
x-1	Vacuuming	RIE		Put the Wafer into the RIE chamber
x-2	Ashing	RIE		Recipe 2; RF 100W for 5 min. with 30sccmO ₂
(y)	Dehydration			
y-1	Dehydration	Upper Oven		120°C, 10 min.
(z)	Resistance Checking			
z-1	Resistance Checking	Multimeter/Agilent 6.5Digit Multimeter		>100MΩ, okay; >1GΩ, Good

For the fabrication involving ITO electrode, sputtering and metal etching recipe have to be changed into the following;

ITO SPUTTERING RECIPE

(a)	Sputtering			
a-1	Vacuuming	Sputter Machine		to less than 10 ⁻³
a-2	Pre-sputtering	Sputter Machine		Target 3 (ITO), 50W(RF) for 5min.
a-3	Sputtering	Sputter Machine		Target 3 (ITO), 300W(RF) for 2.5 min; 100nm

ITO ETCHING RECIPE

(a)	ITO Etching			
a-1	ITO Etching	Glass Tray	HCl	Dilute HCl(35%) with DI water in 1:9 ratio. Etch rate is about 55nm/min. Etch time is about 1.9-2 min.
a-2	Water Cleaning (1)	Glass Tray		
a-3	Water Cleaning (2)	Glass Tray		

Note: In case of haze appearing on substrate, the use of RIE (Ashing) and ultrasonic bath may help in its removal in the case of almost-transparent haze.

On the other hand, haze is the partially dissolved photoresist mixed with etched ITO; thus, its removal may be impossible with opaque haze.

Recipe for Fabrication Interdigital Electrodes on IR grade substrate

Order	Process	Equipment	Chemical	Recipe
(a)	Substrate Cleaning			
a-1	Acetone Cleaning	Plastic Tray(Acetone)		~30sec.
a-2	IPA Cleaning	Plastic Tray(IPA)		~30sec.
a-3	Water Cleaning	Plastic Tray(Water)		~30sec.
(b)	Dehydration			
b-1	N2 Blowing	N2 Gun		~1-2 min.
b-2	Oven Drying	Upper Oven		120°C, 15-20 min.
(c)	Adhesion Enhancement			
c-1	Inserting	HDMS Metal Box		Put the wafer into HDMS Metal Box
c-2	Enhancing		HDMS	Pour HDMS(1 Plastic pipet [~1ml]), Close the lid
c-3	Enhancing (2)			Wait for 2 min.
(d)	PR Coating			
d-1	Spin Coating	Spin Coater	AZP4400	Recipe 0; result in 3.8nm-thick PR
(e)	Soft Bake			
e-1	Soft Bake	Oven		100°C, 20 min.
(e)	Photolithography			
e-1	Machine Start-UP	MLA		Turn on the main switch behind monitor (inside the big metal box)
e-2	Parameter Set Up	MLA		Substrate size/shape, Mask uploading, Exposure Dose, Defocus
e-3	Wafer Set Up	MLA		Open MLA window and aligned substrate. Then, vacuum the stage.
e-4	Exposure	MLA		Expose with laser beam of fixed wavelength
(f)	Developing			
f-1	PR Developing	Plastic Tray(Acetone)	Developer AZ 400K	~90-120 sec.
f-2	Water Cleaning			
f-3	Water Cleaning			
(g)	Residual Removing			
g-1	Vacuuming	RIE		Put the Wafer into the RIE chamber
g-2	Descuuming	RIE		Recipe 1; RF 50W for 1 min. with 30sccmO2
(h)	Metal Deposition			
h-1	Target Set	Sputter		Set the target metal material in target holder
h-2	Vacuuming	Sputter		Set sample on the ceiling and vacuum the
h-3	Presputtering	Sputter		AC Power. ITO target; 5min.
h-4	Sputter	Sputter		AC Power. ITO; 1 min.
(i)	PR Removing			
i-1	Lift-off	Plastic(Acetone)	Remover	5 min. in ultrasonic bath + 1min. X-times Session until clean
i-2	IPA Cleaning	Plastic(IPA)	IPA	
i-3	Water Cleaning	Plastic(Water)		
(j)	PI Coating			

j-1	Spin Coating	Spin Coater	AZP4400	Kato Lab recipe; Slope 5s, Spin 1200rpm 60s, Slope 5s, Spin 2000rpm 60s. Result in XX nm
(k)	PI Bake			
k-1	Bake	Hot plate		100°C, 30 min. Then, 200°C, 60 min.
(l)	Assembling			
l-1	Cell assembling	Alignment Machine MA30TU		Mix spacer with epoxy and applied it on the edge of the cell. Align. Press.

Appendix B

This part explains the preliminary experiment on determining the smallest spatial resolution compatible with our IR absorbance samples and preliminary experiment on determining the camera parameters for POM experiment.

1. Determining the smallest spatial resolution for IR absorbance measurement

Test cell is fabricated with same procedure in chapter 3.4.1. BCH-5F.F.F is filled into the gap. IR energy data is collected with the blank cell as shown in figure B1. For current narrow IR band detector, MCT-N, IR energy is about one-order-of-magnitude higher than that of wide band IR detector, MCT-M. Additionally, its energy per unit area shows much improvement compared to MCT-M and, its peak energy per unit area is at the range of 7×7 to $11 \times 11 \mu\text{m}^2$. Figure B2 shows the IR absorbance as a function of electric field strength of BCH-5F.F.F-filled test cell at different aperture size.

The smallest spatial resolution is determined by the standard deviation of the IR absorbance data. Each conditions is measured 10 times. T-standard is used for calculating standard deviation of the absorbance data. It is found that the smallest spatial resolution with standard deviation that does not overlap or overtake the neighboring data point is $9 \times 9 \mu\text{m}^2$.

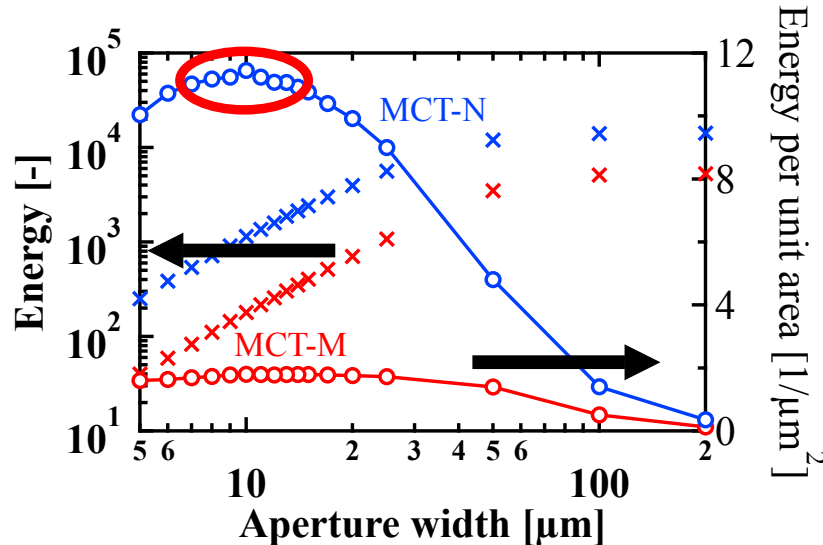


Figure B1: Comparison of IR energy as a function of aperture width between MCT-M and MCT-N

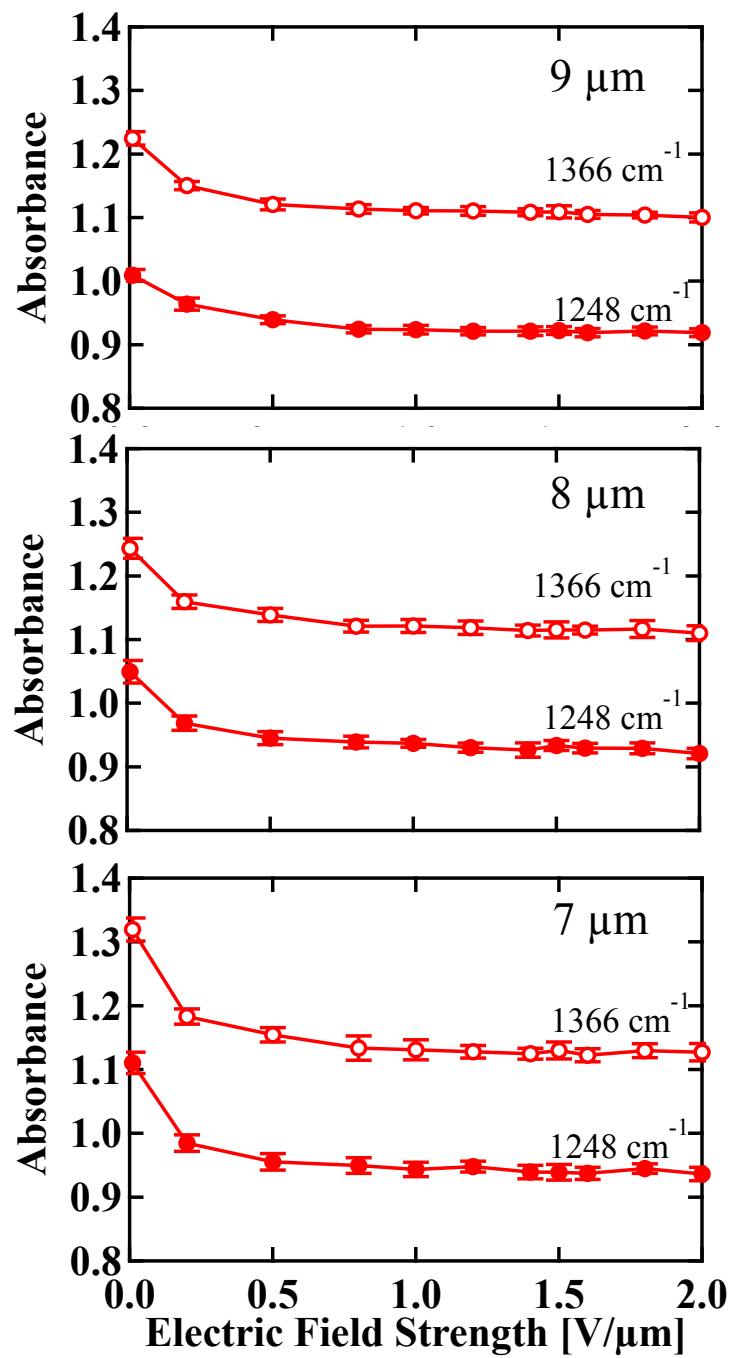


Figure B2: IR absorbance of the characteristics bonds in BCH-5F.F.F as a function of electric field strength at different aperture width..

2. Determining camera parameters for POM

Test cell with same layer composition as electret vibration energy harvester is fabricated with ITO as electrode materials; namely, TEMPAX/ITO/ Al_2O_3 /Air(fluid)/CYTOP/ITO/TEMPAX. The 100 μm -thick dielectric gap is filled with MLC-7030. Al_2O_3 act as horizontal alignment layer. The impedance measurement shows that LC between Al_2O_3 layers aligned horizontally in the absence of electric field. Test cell is, then, use in POM setup.

Shutter speed, gain and, gamma value are varied to determine the condition with acceptable highest luminescence or raw pixel value from POM images as shown in figure B3. Low raw pixel value can be interpreted as low signal-to-noise ratio. Since maximum pixel value from POM images is 256, we set the criteria for camera parameters to at least results in pixel value of 100. After many measurements, it is found that high gamma will result in smaller raw pixel value. On the other hand, raw pixel value is increased with increasing gain value but, it is decreased when it is too high. Taking the vibration frequency of the generator in to account, we set the shutter speed to be 500fps (2ms). The optimal camera parameters are gain = 2.5, and gamma = 0.6 at the shutter speed of 500fps.

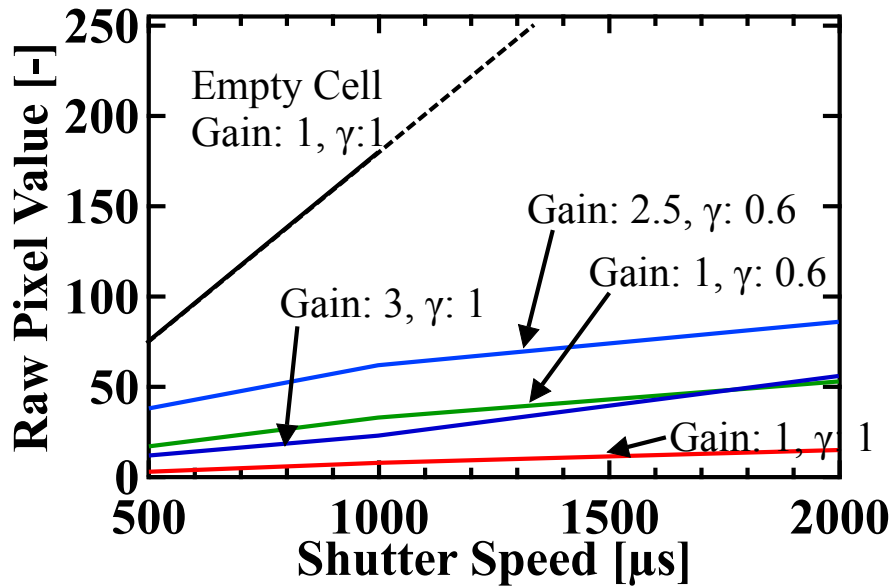


Figure B3: Raw pixel value of POM images taken at different camera parameters. Black dash line is the extrapolation of raw pixel value of empty cell.